

Aus der Klinik für Radioonkologie, Cyberknife- und Strahlentherapie
der Universität zu Köln
Direktor: Univ.-Prof. Dr. Dr. Emmanouil Fokas

Modulation of the cGAS/STING pathway in various tumor cell lines by a novel HSP90 inhibitor

Inaugural-Dissertation zur Erlangung der Doktorwürde
der Medizinischen Fakultät
der Universität zu Köln

vorgelegt von
Marie Isabelle Heßelmann
aus Hilden

promoviert am 04. April 2025

Gedruckt mit Genehmigung der Medizinischen Fakultät der Universität zu Köln
2025

Dekan: Universitätsprofessor Dr. med. G. R. Fink

1. Gutachter: Privatdozent Dr. med. J. M. G. A. Herter
2. Gutachter: Universitätsprofessor Dr. rer. nat. H. Kashkar

Erklärung

Ich erkläre hiermit, dass ich die vorliegende Dissertationsschrift ohne unzulässige Hilfe Dritter und ohne Benutzung anderer als der angegebenen Hilfsmittel angefertigt habe; die aus fremden Quellen direkt oder indirekt übernommenen Gedanken sind als solche kenntlich gemacht.

Bei der Auswahl und Auswertung des Materials sowie bei der Herstellung des Manuskriptes habe ich keine Unterstützungsleistungen erhalten.

Weitere Personen waren an der Erstellung der vorliegenden Arbeit nicht beteiligt. Insbesondere habe ich nicht die Hilfe einer Promotionsberaterin/eines Promotionsberaters in Anspruch genommen. Dritte haben von mir weder unmittelbar noch mittelbar geldwerte Leistungen für Arbeiten erhalten, die im Zusammenhang mit dem Inhalt der vorgelegten Dissertationsschrift stehen.

Die Dissertationsschrift wurde von mir bisher weder im Inland noch im Ausland in gleicher oder ähnlicher Form einer anderen Prüfungsbehörde vorgelegt.

Die Transfektion der verwendeten ACF133.3-OVA- sowie RP157.8-OVA-Zellen wurde von Frau Dr. Martha Kiljan geplant und durchgeführt.

Die übrigen in dieser Arbeit angegebenen Experimente sind nach entsprechender Anleitung durch Herrn Matthias Reinscheid und Frau Dr. Martha Kiljan von mir selbst ausgeführt worden.

Erklärung zur guten wissenschaftlichen Praxis:

Ich erkläre hiermit, dass ich die Ordnung zur Sicherung guter wissenschaftlicher Praxis und zum Umgang mit wissenschaftlichem Fehlverhalten (Amtliche Mitteilung der Universität zu Köln AM 132/2020) der Universität zu Köln gelesen habe und verpflichte mich hiermit, die dort genannten Vorgaben bei allen wissenschaftlichen Tätigkeiten zu beachten und umzusetzen.

Köln, den 03.12.2024

Unterschrift:

Danksagung

Diese Arbeit wäre nicht möglich gewesen ohne die großartige Unterstützung vieler Menschen sowohl im als auch außerhalb des Labors.

Für die engagierte Betreuung meiner Dissertation möchte ich Herrn PD Dr. Jan Herter sowie Frau PD Dr. Grit Herter-Sprie herzlich danken. Ich danke außerdem Matthias Reinscheid und Martha Kiljan für die lehrreiche und geduldige Einarbeitung im Labor, die mir ermöglichte, die Experimente für diese Dissertation eigenständig durchzuführen. Des Weiteren geht mein Dank an alle ehemaligen Mitarbeiter:Innen der Herter-Labs, insbesondere Olta Ibruli, Jiali Cai, Li-Na Niu, Elena Wagner und Yagmur Shabaz. Jeder und Jede, die ich in meiner Zeit im Labor kennenlernen durfte, hat dazu beigetragen, dass diese Zeit mir immer in wertvoller Erinnerung bleiben wird.

Für die Unterstützung außerhalb des Labors, für ihr immer offenes Ohr und für Ablenkung, wenn diese dringend nötig war, möchte ich Luisa Böhmert, Jennifer Schitz und Jason Winkenstern danken.

Diese Arbeit wäre nicht möglich gewesen ohne meine Eltern. Für eure unermüdliche und bedingungslose Unterstützung bin ich unendlich dankbar.

Zuletzt danke ich der Friedrich-Naumann-Stiftung für die Freiheit für Ihre Unterstützung während meines Studiums.

Table of Contents

| | |
|------------------------------------------------|-----------|
| LIST OF ABBREVIATIONS | 7 |
| 1. ZUSAMMENFASSUNG | 10 |
| 2. ABSTRACT | 11 |
| 3. INTRODUCTION | 12 |
| 3.1 Cancer | 12 |
| 3.1.1. Lung cancer | 13 |
| 3.1.2. Colorectal cancer | 15 |
| 3.2 The immune system | 17 |
| 3.3 Tumor immunogenicity | 18 |
| 3.4 Immunotherapy | 21 |
| 3.5 Radiation therapy | 22 |
| 3.6 The cGAS/STING pathway | 24 |
| 3.7 Heat shock protein 90 | 26 |
| 3.8 TAS-116 | 29 |
| 3.9 Rationale | 30 |
| 4. MATERIALS AND METHODS | 32 |
| 4.1 Materials | 32 |
| 4.1.1. Devices | 32 |
| 4.1.2. Laboratory and cell culture material | 32 |
| 4.1.3. Solutions | 33 |
| 4.1.4. Reagents | 33 |
| 4.1.5. Antibodies | 35 |
| (1) Antibodies for flow cytometry | 35 |
| (2) Antibodies for immunofluorescence staining | 35 |
| 4.1.6. Software | 36 |
| 4.2 Methods | 36 |

| | | |
|-----------|---------------------------------------------------------|-----------|
| 4.2.1. | Cell lines | 36 |
| (1) | Small cell lung cancer – RP157.8 | 36 |
| (2) | Non-small cell lung cancer – ACF135.10 | 36 |
| (3) | Colon carcinoma – MC38 | 37 |
| (4) | Melanoma – B16F ₁₀ | 37 |
| (5) | Lymphoma – E.G7 | 37 |
| 4.2.2. | OT-I mice | 37 |
| 4.2.3. | Isolation and activation of T cells | 38 |
| 4.2.4. | TAS-116 | 38 |
| 4.2.5. | TAS-116 cytotoxicity assay | 38 |
| 4.2.6. | Viability assay after TAS-116 treatment and irradiation | 39 |
| 4.2.7. | Analysis of cGAS/STING pathway activation | 40 |
| (1) | DNA double-strand breaks - γ H2AX | 40 |
| (2) | Cytosolic double-stranded DNA | 40 |
| (3) | STING phosphorylation | 41 |
| (4) | IFN β | 41 |
| (5) | Quantification of fluorescence signal intensity | 42 |
| 4.2.8. | CD8 ⁺ T cell-mediated killing assay | 42 |
| 4.2.9. | Analysis of TCR clonality | 43 |
| 5. | RESULTS | 46 |
| 5.1 | Cell line specific cytotoxicity of TAS-116 | 46 |
| 5.2 | Viability after TAS-116 treatment and irradiation | 48 |
| 5.3 | Induction of DNA double-strand breaks | 54 |
| 5.4 | Analysis of cGAS/STING pathway activation | 59 |
| 5.4.1. | Cytosolic double-stranded DNA | 60 |
| 5.4.2. | STING phosphorylation | 65 |
| 5.4.3. | IFN β secretion | 70 |
| 5.4.4. | Summary of cGAS/STING pathway analysis | 75 |
| 5.5 | CD8 ⁺ T cell-mediated killing | 76 |
| 5.6 | Analysis of TCR clonality | 79 |
| 6. | DISCUSSION | 81 |
| 6.1 | Effects of HSP90 inhibition and RT on MC38 cells | 81 |
| 6.2 | Effects of HSP90 inhibition and RT on RP157.8 cells | 83 |

| | | |
|------------|----------------------------------------------------------------------------------|------------|
| 6.3 | Effects of HSP90 inhibition and RT on ACF135.10 cells | 85 |
| 6.4 | Effects of HSP90 inhibition and RT on CTL-mediated killing of tumor cells | 87 |
| 6.5 | Effects of HSP90 inhibition and RT on TCR clonality | 88 |
| 6.6 | Conclusion | 90 |
| 7. | BIBLIOGRAPHY | 91 |
| 8. | APPENDIX | 105 |
| 8.1 | List of figures | 105 |
| 9. | PRELIMINARY PUBLICATIONS OF RESULTS | 106 |

List of abbreviations

| | |
|--------------------|--------------------------------------------------------|
| 17-AAG | 17-allylamino-17-demethoxy-geldanamycin |
| 17-DMAG | 17-Dimethylaminoethylamino-17-demethoxygeldanamycin |
| 7-AAD | 7-amino-actinomycin D |
| Apaf-1 | Apoptotic protease-activating factor 1 |
| APC | Antigen-presenting cell |
| APC (gene) | Adenomatous polyposis coli |
| ATM | Ataxia telangiectasia mutated kinase |
| ATP | Adenosine triphosphate |
| BER | Base excision repair |
| BSA | Bovine serum albumin |
| CD | Cluster of differentiation |
| cDMEM | Complete Eagle's minimal essential medium |
| cGAMP | Cyclic guanosine monophosphate-adenosine monophosphate |
| cGAS | Cyclic-GMP-AMP synthase |
| CMS | Consensus molecular subtypes |
| CRC | Colorectal cancer |
| CTL | Cytotoxic T lymphocyte |
| CTLA-4 | Cytotoxic T-lymphocyte-associated protein 4 |
| CYP450 | Cytochrome P450 |
| DAMP | Damage-associated molecular pattern |
| DAPI | Diamidino-2-phenylindole |
| DC | Dendritic cell |
| ddH ₂ O | Double-distilled water |
| DDR | DNA damage repair |
| DMSO | Dimethyl sulfoxide |
| DNA | Deoxyribonucleic acid |
| DNA-PK | DNA-dependent protein kinase |
| DNase | Deoxyribonuclease |
| dsDNA | Double-stranded DNA |
| EGFR | Epidermal growth factor receptor |
| EMA | European Medicines Agency |
| FAP | Familial adenomatous polyposis |
| FBS | Fetal bovine serum |
| FDA | United States Food and Drug Administration |

| | |
|----------------|--------------------------------------------------|
| GFP | Green fluorescent protein |
| GIST | Gastrointestinal stromal tumor |
| GTP | Guanosine-5'-triphosphate |
| HER-2 | Human epidermal growth factor |
| HLA | Human leukocyte antigen |
| HR | Homologous recombination |
| HSF1 | Heat shock transcription factor 1 |
| HSP90 | Heat shock protein 90 |
| HSR | Heat shock response |
| IDO | Indoleamine 2,3-dioxygenase |
| IFN | Interferon |
| IFN α | Interferon alpha |
| IFN β | Interferon beta |
| IFN γ | Interferon gamma |
| IL-2 | Interleukin-2 |
| IRF3 | Interferon regulatory factor 3 |
| KRAS | Kirsten rat sarcoma virus |
| LUAD | Lung adenocarcinoma |
| LUSC | Lung squamous cell carcinoma |
| MDSC | Myeloid-derived suppressor cell |
| MHC | Major histocompatibility complex |
| MICA/B | MHC class I polypeptide-related sequence A and B |
| MMP-2 | Matrix metalloproteinase 2 |
| MMR | Mismatch repair |
| mRNA | Messenger ribonucleic acid |
| MSI | Microsatellite instability |
| MSI-H | Microsatellite instability-high |
| MSS | Microsatellite stable |
| NF- κ B | Nuclear factor kappa B |
| NHEJ | Non-homologous end joining |
| NK | Natural killer cell |
| NKG2D | Natural killer group 2D |
| NKT | NK1.1 ⁺ / CD3 ⁺ T cells |
| NSCLC | Non-small cell lung cancer |
| PAMP | Pathogen-associated molecular pattern |
| PARP | Poly ADP ribose polymerase |

| | |
|------------------|-----------------------------------------------------------------------------------------------------------|
| PBS | Phosphate-buffered saline |
| PD-1 | Programmed cell death protein 1 |
| PD-L1/2 | Programmed death-ligand 1/2 |
| PFA | Paraformaldehyde |
| PFS | Progression-free survival |
| PI | Propidium Iodide |
| POLE | DNA polymerase epsilon catalytic subunit |
| pSTING | Phosphorylated STING |
| RAS | Rat sarcoma virus |
| RB1 | Retinoblastoma protein 1 |
| RNA | Ribonucleic acid |
| ROS | Reactive oxygen species |
| RPMI | Roswell Park Memorial Institute medium |
| RT | Radiation therapy |
| SCLC | Small cell lung cancer |
| SD | Standard deviation |
| SEM | Standard error of the mean |
| STING | Stimulator of interferon genes |
| TANK | TRAF family member-associated NF- κ B activator |
| TAS-116 | 3-ethyl-4-[4-[4-(1-methylpyrazol-4-yl)imidazol-1-yl]-3-propan-2-yl]pyrazolo[3,4-b] pyridin-1-yl]benzamide |
| TBK1 | TANK binding kinase 1 |
| TCR | T cell receptor |
| TKI | Tyrosine kinase inhibitor |
| TLR | Toll-like receptor |
| TMB | Tumor mutational burden |
| TME | Tumor microenvironment |
| TNF | Tumor necrosis factor |
| TP53 | Tumor protein p53 |
| TRAF | Tumor necrosis factor receptor-associated factor |
| TRAIL | TNF-related apoptosis-inducing ligand |
| T _{reg} | Regulatory T cell |
| TREX1 | Three prime repair exonuclease 1 |
| ULK1 | UNC-51-like kinase |
| VEGF-A | Vascular endothelial growth factor A |
| WT | Wildtype |
| γ H2AX | Phosphorylated histone H2AX |

1. Zusammenfassung

Obwohl es heute eine Vielzahl von Behandlungsmethoden für bösartige Erkrankungen gibt, ist Krebs nach wie vor eine der häufigsten Todesursachen weltweit. Neben chirurgischen Verfahren, Chemo- und Strahlentherapie haben immuntherapeutische Ansätze die Krebstherapie in den letzten Jahren revolutioniert. Allerdings profitiert nur ein Teil der Patientinnen und Patienten langfristig von einer solchen Therapie und es kommt häufig zu Resistenzentwicklung. Seit langem ist bekannt, dass Strahlentherapie neben der direkten Wirkung auf neoplastische Zellen auch die Immunogenität von Tumoren positiv beeinflusst und daher einen vielversprechenden Ansatz für kombinatorische Behandlungsschemata darstellt. Es ist bekannt, dass die immunmodulatorische Wirkung von Bestrahlung zu einem großen Teil auf Typ-I-Interferone zurückzuführen ist, welche durch Aktivierung des cGAS/STING-Signalwegs bei DNA-Schäden induziert werden. Das molekulare Chaperon HSP90 spielt eine zentrale Rolle bei der Stabilisierung von Proteinen, die an der Reparatur von DNA-Schäden beteiligt sind, sodass das Unterdrücken seiner Funktion Zellen anfälliger für Bestrahlung macht. In dieser Arbeit wurde der HSP90-Inhibitor TAS-116 mit nachfolgender Bestrahlung *in vitro* an verschiedenen murinen Tumorzelllinien getestet, um tumortyp-spezifische Unterschiede in Bezug auf synergistische Effekte auf die Immunogenität von Tumoren herauszuarbeiten. Der Wirkstoff wurde vor allem murinen SCLC-, NSCLC- und Kolonkarzinomzellen in Konzentrationen verabreicht, von denen bekannt ist, dass sie für jede Zelllinie subtoxisch sind, und die Aktivierung des cGAS/STING-Signalwegs wurde quantifiziert. TAS-116 und Strahlentherapie zeigten ein synergistisches Potential bezüglich der Aktivierung des cGAS/STING-Signalwegs, welches bei Lungenkrebszellen stärker ausgeprägt war als bei Kolonkarzinomzellen. Dieses Potential einer verbesserten Immunogenität von Tumoren wurde anschließend in einem *In-vitro*-Ansatz zur Untersuchung der spezifischen Eliminierung von Tumorzellen durch CD8⁺ T-Lymphozyten weiter untersucht. Die kombinierte Behandlung mit HSP90-Inhibition und Strahlentherapie von tumortragenden Mäusen führte zu interessanten Ergebnissen in Bezug auf Veränderungen des T-Zell-Rezeptor-Repertoires von tumorinfiltrierenden Lymphozyten, was zur weiteren vertieften Forschung in diesem Bereich anregt. Insgesamt gibt diese Arbeit Einblick in mögliche tumortypabhängige Unterschiede hinsichtlich einer Synergie von HSP90-Inhibition und Strahlentherapie. Die daraus gewonnenen Erkenntnisse sollten durch *In-vivo*-Behandlungsstudien weiter vertieft werden. Auch wenn die Studienhypothese nicht bestätigt werden konnte, bieten die in dieser Arbeit erzielten Ergebnisse ermutigende Aussichten für die weitere Forschung hinsichtlich des Einsatzes von HSP90-Inhibition in Kombination mit Bestrahlung als vielversprechenden Ansatz zur Steigerung der Wirksamkeit immuntherapeutischer Ansätze und somit für bessere Therapiemöglichkeiten für viele Krebspatientinnen und -patienten in der Zukunft.

2. Abstract

Although a variety of treatment modalities for malignant diseases are available today, cancer remains one of the leading causes of death worldwide. In addition to surgery, chemotherapy, and radiation therapy, immunotherapeutic approaches have revolutionized cancer therapy in recent years. However, durable benefits are confined to only a subset of patients and development of resistance is common. It has long been known that radiation therapy, in addition to its direct effects on neoplastic cells, also positively affects tumor immunogenicity and therefore represents a promising approach for combinatory treatment regimens. Immunomodulatory effects of radiation are known to be dependent on type-I interferon signaling resulting from activation of the cGAS/STING pathway upon DNA damage. The molecular chaperone HSP90 plays a pivotal role in stabilizing proteins involved in DNA damage repair mechanisms and its inhibition therefore renders cells more susceptible to irradiation. In this thesis, the HSP90 inhibitor TAS-116 was applied to various murine tumor cell lines with subsequent irradiation *in vitro* to elucidate tumor type-specific differences in terms of synergistic effects on tumor immunogenicity. The agent was administered primarily to murine SCLC, NSCLC, and colon carcinoma cells at concentrations known to be subtoxic to each cell line, and activation of the cGAS/STING pathway was quantified. TAS-116 and radiation therapy displayed synergistic potential to activate the cGAS/STING pathway, which was more pronounced in lung cancer cells than in colon carcinoma cells. This potential to improve tumor immunogenicity was subsequently further investigated in an *in vitro* approach examining specific killing of tumor cells by CD8⁺ T lymphocytes. Combined treatment with HSP90 inhibition and radiation therapy of tumor-bearing mice led to interesting results in terms of changes in the T cell receptor repertoire of tumor-infiltrating lymphocytes, encouraging future in-depth research in this area. Overall, this work provides insight into possible tumor type-dependent differences regarding synergy of HSP90 inhibition and radiotherapy. The knowledge acquired from these findings should be further expanded on through *in vivo* treatment studies. Even though the study hypothesis could not be confirmed hereby, the results obtained in this thesis offer encouraging prospects for further investigation of HSP90 inhibition in combination with radiation as a promising approach to enhance the efficacy of immunotherapeutic approaches and thus provide better therapeutic options for many cancer patients in the future.

3. Introduction

3.1 Cancer

Accounting for 9.7 million deaths in 2022, cancer remains one of the leading causes of death worldwide. While lung-, breast-, and colorectal cancers are the most common cancer types, lung-, colorectal, and liver cancer are the leading causes of death among cancer patients¹.

In 2000, Hanahan and Weinberg postulated six characteristics most malign cells have in common. These 'hallmarks of cancer' were later expanded to a total of eight core capabilities of cancer cells, namely "*the acquired capabilities for sustaining proliferative signaling, evading growth suppressors, resisting cell death, enabling replicative immortality, inducing / accessing vasculature, activating invasion and metastasis, reprogramming cellular metabolism, and avoiding immune destruction*"² (Fig. 1).



Figure 1: The hallmarks of cancer (D. Hanahan, 2022)³

The hallmarks of cancer are eight core capabilities common to most tumor cells that enable growth and progression of malignancies. In addition, two enabling characteristics involved in the activation of cancer hallmarks have been defined: tumor-promoting inflammation, and genome instability and mutation.

While genetic predisposition and environmental factors play a central role in the development of malignant diseases, spontaneous somatic mutations also occur in human cells during the

cell division process. Because such mutations are stochastic events, it is partly a matter of chance which genes gather which type of mutations at a given time in life⁴. Therefore, the accumulation of somatic mutations may eventually lead to activating mutations of oncogenes or inactivation of tumor suppressor genes, promoting uncontrolled proliferation of mutant cells and ultimately carcinogenesis⁵. However, cancer cells continue to undergo genetic changes even after complete malignant transformation, resulting in intratumoral genetic heterogeneity. The origin of most solid tumors can be traced back to a single cell that has been malignantly altered by a truncal mutation. Nevertheless, genetically distinct populations of subclones, starting from their common progenitor cell, evolve in parallel. This model of cancer development, termed 'branched evolution', inevitably results in high intratumoral heterogeneity and has been described for lung cancer, colon cancer, and melanoma, among others⁶. This is of high clinical relevance because patients with tumors of high genetic heterogeneity are more likely to develop resistance to cancer therapies due to expansion of certain preexisting subclonal populations under therapeutic pressure⁷.

3.1.1.Lung cancer

Accounting for 12.4% of all cancer cases and 18.7% of total cancer deaths in 2022¹, lung cancer is of immense importance to the medical system worldwide. With 90% of all cases attributable to tobacco use, smoking remains the most important modifiable risk factor for the development of lung cancer. However, as the prevalence of smoking generally declines, other factors such as air pollution, asbestos and radon exposure, as well as chronic lung disease are becoming increasingly important⁸.

Histologically, 15% of total lung cancer cases can be classified as small cell lung cancer (SCLC)⁹. SCLC tumors originate from neuroendocrine cells in the lung epithelium¹⁰ and are characterized by rapid growth and a tendency to metastasize early. They are, however, considered curable if the cancer is still confined to one hemithorax at the time of diagnosis.

The carcinogenesis of SCLC is primarily driven by bi-allelic inactivation of tumor protein p53 (*TP53*) and retinoblastoma protein 1 (*RB1*). Loss of function of both proteins has been found to be mandatory for SCLC pathogenesis¹¹.

Treatment of SCLC at a limited stage consists of chemoradiotherapy with prophylactic cranial irradiation¹². However, 2-year survival rates are low at only 14-15%¹³, as 70% of SCLC patients already have metastases at the time of diagnosis (stage IV)¹⁴. In recent years, management of extended-stage SCLC has advanced by approval of the checkpoint inhibitors atezolizumab and durvalumab, monoclonal antibodies against programmed death-ligand 1 (PD-L1). These checkpoint inhibitors, in combination with platinum-based chemotherapy as first-line treatment, resulted in an improved overall survival of 12.3 and 13.0 months, respectively, compared with

10.3 months for chemotherapy alone. This is independent of PD-L1 immunohistochemistry status^{15,16}.

Of the 85% of lung cancers classified as non-small lung cancer (NSCLC), the most common histologic subtypes are lung squamous cell carcinoma (LUSC) and lung adenocarcinoma (LUAD), the latter being the most frequently diagnosed type of lung cancer in non-smokers¹⁷. Both NSCLC subtypes are characterized by a high mutation rate and genomic complexity, but generally have a better prognosis than SCLC, with a 2-year survival rate of 42%¹³. While somatic mutations of *TP53* are found in most LUSC tumors, the most common targetable mutations in LUAD, namely epidermal growth factor receptor (*EGFR*) and Kirsten rat sarcoma virus (*KRAS*) mutations, are very rare in LUSC tumors, leading to marked differences in terms of treatment¹⁷.

The first-line therapy of NSCLC diagnosed at stage I-II is complete surgical resection of the tumor, if possible. Adjuvant cisplatin-based chemotherapy regimens have resulted in a 5.4% total survival benefit at 5 years in patients with stage II or IIIa tumors after resection¹⁸. The phase III CheckMate 816 trial showed that neoadjuvant chemotherapy in combination with nivolumab treatment prolonged event-free survival by 10.8 months and improved the pathological complete response rate by 22% in patients with resectable stage Ib to IIIa NSCLC compared with neoadjuvant chemotherapy alone. Moreover, this benefit to patients did not negatively affect the occurrence of adverse events or the feasibility of surgery¹⁹.

Complete resection generally has curative potential in the treatment of stage III NSCLC, if possible. However, at this stage the disease is often considered unresectable because large or invasive tumors cannot be removed without leaving a positive margin, or supraclavicular or contralateral lymph nodes are infested²⁰. In these cases, definite chemoradiation with concurrent administration of chemotherapy and radiation therapy (RT) has been shown to be more effective than sequential treatment²¹. Furthermore, consolidation therapy with durvalumab after chemoradiotherapy improved overall survival and progression-free survival (PFS) in the phase III, placebo-controlled PACIFIC trial, establishing this treatment regimen as standard of care for patients with unresectable, stage III NSCLC²².

On the other hand, patients with metastatic disease (stage IV) generally require systemic therapy. Before immunotherapeutic therapies became accessible, the standard treatment for these patients consisted of platinum-based chemotherapy²³. However, molecular characterization of tumor samples and discovery of targetable mutations led to new therapeutic approaches. Targeted therapy of *EGFR*-mutated tumors with tyrosine kinase inhibitors (TKI) has been shown to reduce the risk of disease progression or death by 63% compared with patients receiving chemotherapy²⁴. Nevertheless, 40-60% of patients who initially respond to treatment with *EGFR* TKIs develop resistance over time. For these patients, the TKI osimertinib

has been shown to target both EGFR and the missense mutation responsible for resistance development, leading to a disease control rate of 84%²⁵.

In recent years, immunotherapeutic approaches have contributed to immense changes in the treatment of NSCLC patients. The checkpoint inhibitor pembrolizumab, targeting programmed cell death protein 1 (PD-1), has been shown to prolong median PFS by 4.3 months in stage IV NSCLC patients with PD-L1 expression status greater than 50%, compared to patients receiving chemotherapy²⁶. Combination therapy with pembrolizumab and platinum-based chemotherapy further improved PFS by 3.9 months in comparison to chemotherapy and placebo in patients with metastatic NSCLC²⁷. Additionally, a recent study evaluating stereotactic irradiation of a single tumor site in patients with advanced NSCLC prior to treatment with pembrolizumab showed beneficial effects compared with pembrolizumab treatment alone²⁸, displaying promising prospects for potential future combinatorial treatment regimens.

3.1.2.Colorectal cancer

In 2022, colorectal cancer (CRC) accounted for 9.6% of global cancer cases and 9.3% of cancer deaths¹. Of all CRC cases, 39% develop in the proximal, 24% in the distal colon, and 30% in the rectum with remaining cases classified as “not otherwise specified”²⁹. Incidence rates double every five years up to the age of 50 and increase by approximately 30% in subsequent age groups. In both sexes, incidence rates for CRC have steadily declined since the 1980s. However, this decrease in incidence only reflects the trend in the older generation and is largely due to the rapid spread of colonoscopy screening. In contrast, incident rates in individuals younger than 50 years have increased since the 1990s, with an annual increase of 1.8% in proximal and distal colon cancer in this group³⁰. A study among cancer patients in the United States showed that about 54% of deaths from CRC were due to modifiable risk factors such as dietary habits, physical inactivity, alcohol consumption, smoking, and excess body weight³¹.

Most CRCs develop in a stepwise process from normal to dysplastic to cancerous cells, known as the adenoma-carcinoma sequence. The most common mutation known to occur early in this sequence affects the adenomatous polyposis coli (*APC*) tumor suppressor gene. Germline mutations of the *APC* gene also underlie familial adenomatous polyposis (FAP), a hereditary disease characterized by the excessive occurrence of colorectal adenomas beginning in adolescence and inevitably leading to the development of CRC. Other genetic aberrations believed to occur early in the adenoma-carcinoma sequence include a gain-of-function mutation of *KRAS*, mutation or overexpression of *TP53*, and allelic loss of chromosomal regions 5q, 17p or 18q³².

However, 15% of CRC acquire genetic alterations due to DNA mismatch repair (MMR) deficiency. MMR-deficient cancers accumulate mutations in repetitive microsatellite DNA segments and therefore exhibit a phenotype termed high-level microsatellite instability (MSI). These MSI-high (MSI-H) CRC tumors differ from colon carcinomas following the adenoma-carcinoma sequence in several ways, e.g., they are more frequently located in the proximal colon³³, are characterized by a higher density of tumor-infiltrating lymphocytes³⁴, and have a significantly better prognosis than their microsatellite stable (MSS) counterparts³⁵. Moreover, Guinney et al. classified CRC tumors into four consensus molecular subtypes (CMS), namely CMS1 (14%, MSI immune), CMS2 (37%, canonical), CMS3 (13%, metabolic), and CMS4 (23%, mesenchymal), based on genetic, epigenetic and transcriptomic characteristics, clinical features, and differences in the tumor microenvironment (TME)³⁶. This allows for a better assessment of the prognosis of CRC patients as well as their response to specific therapies^{36,37}.

Patients with non-metastatic colon cancer usually undergo surgery in a curative attempt. For lymph node positive disease (stage III or higher), R0 resection, i.e., resection to microscopically tumor-free margins, should be followed by additional fluorouracil-based adjuvant therapy. However, regarding stage II colon carcinomas, such adjuvant chemotherapy should only be given to MSS tumors, as no benefit has been demonstrated for MSI-H tumors³⁸.

Patients with metastatic, unresectable CRC require systemic therapy and should preferably be treated with doublet chemotherapy in combination with targeted therapy using monoclonal antibodies against EGFR or vascular endothelial growth factor A (VEGF-A). However, because the efficacy of antibodies against EGFR has been shown to be confined to patients with rat sarcoma virus (*RAS*) gene wildtype (WT) status, they should not be used in patients with a *RAS* mutation³⁹.

In 2017, the checkpoint inhibitors pembrolizumab and nivolumab, blocking PD-1, were approved by the United States Food and Drug Administration (FDA) for MSI-H CRC after patients with this type of cancer were shown to benefit from such therapy in terms of prolonged PFS^{40,41}. Recently, combination therapy with nivolumab and low-dose ipilimumab, a checkpoint inhibitor targeting cytotoxic T-lymphocyte-associated protein 4 (CTLA-4), as first-line therapy for patients with metastatic MSI-H CRC has demonstrated a disease control rate of 84% in a phase II study⁴². This suggests promising prospects for future combination treatment regimens for CRC.

3.2 The immune system

The immune system is commonly divided into two groups (*Fig. 2*). Cells part of the innate immune system are responsible for the initial response against pathogen structures and include granulocytes, macrophages, eosinophils, basophils, natural killer cells (NK), and dendritic cells (DC). These cells are able to recognize pathogen-associated molecular patterns (PAMP) and damage-associated molecular patterns (DAMP) via toll-like receptors (TLR) on their surface. Upon recognition of such molecular patterns, cells are activated and produce pro-inflammatory cytokines and interferons (IFN).

The second subsystem, adaptive immunity, follows this initial response with some delay. B lymphocytes mediate humoral immunity against extracellular targets by producing soluble antibodies that specifically bind to surface molecules of the invading pathogen. This effect, known as opsonization, marks pathogens for neutralization or phagocytosis by other immune cells or the complement system. The cellular immune response is directed against intracellular structures and is mediated by T cells. Depending on the type of receptors, or cluster of differentiation (CD), expressed on their surface, the latter can be divided into CD8⁺ cytotoxic T lymphocytes (CTL) and CD4⁺ helper T cells.

B and T lymphocytes originate in the bone marrow. While B cells remain there, T cells migrate to the thymus in the course of their development. Here, in a complex process of rearrangement of different DNA segments, T cell receptors (TCR) are formed that specifically recognize different antigens when presented via major histocompatibility complex (MHC) molecules. Positive selection ensures that only T cells that do not recognize self-antigens leave the thymus and migrate to the lymph nodes.

If a specific pathogen persists after the first line of defense of the innate immune system, macrophages and DCs, also known as antigen-presenting cells (APC), phagocytose pathogen debris and present corresponding peptides via MHC-I (intracellular pathogens) or MHC-II (extracellular pathogens) receptors on their surface. After APCs have migrated to local lymph nodes, peptides presented via MHC receptors can be recognized by naïve T cells via their TCR, which initiates the priming process. In addition, complete activation of T cells also requires co-stimulatory signals mediated by molecules on APCs and T cells, respectively, as well as another CD4⁺ T cell-dependent priming step. In the absence of this last step, CD8⁺ T cells exhibit an 'exhausted' phenotype characterized by impaired cytotoxicity, cellular migration, and invasive potential. Upon activation, CD8⁺ T cells bind to cells presenting their cognate peptide in the periphery, causing cell death of the target. Meanwhile, CD4⁺ T cells assist in either the activation of additional CTLs or the B cell-mediated antibody response^{43,44}. Regulatory T cells (T_{reg}) represent an anti-inflammatory subtype of CD4⁺ T lymphocytes. These cells exert an immunosuppressive activity through various mechanisms, including CTLA-4

mediated suppression of APC function, production of immunosuppressive cytokines, and elimination of effector cells via secretion of granzyme and perforin⁴⁵.

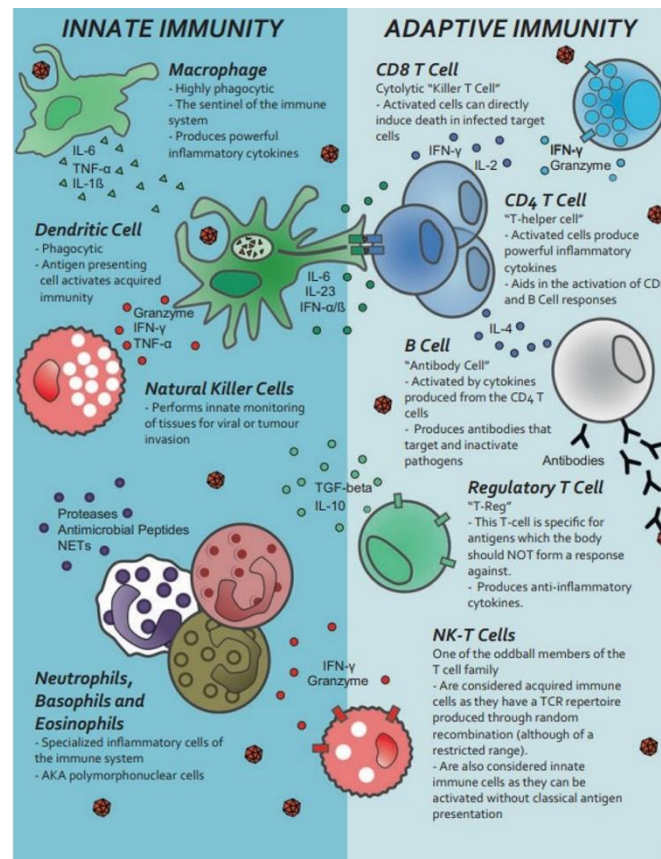


Figure 2: Common cells of the immune system (McComb et al., 2019)⁴³

Cells of the immune system are classified into two groups: Innate immune cells form the first line of defense against invading pathogens and include macrophages, dendritic cells, natural killer cells, neutrophils, basophils, and eosinophils. B and T lymphocytes as well as NK-T cells are part of adaptive immunity and are capable of eliciting an antigen-specific immune response.

3.3 Tumor immunogenicity

The term tumor immunogenicity describes "the ability of a tumor to induce an immune response that can prevent its growth"⁴⁶. In 1909, Paul Ehrlich was among the first scientists to establish that the immune system is capable of eliminating cells in the process of malignant degeneration, thus preventing cancer development⁴⁷. However, this concept of 'cancer immune surveillance' soon proved to be inadequate, as malignant transformations arise even in immunocompetent host organisms. It is known today that while immune cells can recognize and possibly eliminate tumor cells, they exert not only host-protective but also potential tumor-promoting effects. This process of the immune system shaping tumor immunogenicity has been termed cancer immunoediting and proceeds in three discrete steps: elimination, equilibrium, and escape⁴⁸.

The elimination phase involves the process of recognition and subsequent eradication of neoplastic cells by the immune system. Innate immune cells primarily involved in this process include NK cells, NK1.1⁺ / CD3⁺ (NKT), and $\gamma\delta$ T cells. NKT cells are a population of $\alpha\beta$ T cells that also express some NK-specific receptors. They are therefore capable of eliminating cells via TCR recognition as well as killing NK-sensitive targets and are present in most tissues where T cells are found. On the other hand, T cells carrying the $\gamma\delta$ TCR reside either in peripheral blood or within epithelial tissues. They differ from their $\alpha\beta$ -counterparts primarily in their ability to recognize tumor-specific antigens without the precondition of antigen processing and presentation via conventional MHC molecules. Moreover, they express receptors normally found on NK cells, providing them with additional effector mechanisms^{49,50}.

Upon recognition of malignantly transformed cells, NK, NKT, and $\gamma\delta$ T cells are stimulated to release IFN γ , which exerts multiple tumor suppressive effects. Apart from its direct antiproliferative effect on the developing tumor, IFN γ promotes the recruitment of immune effector cells, which in turn cause tumor cell death through various mechanisms. Cell debris is then transported by DCs to local lymph nodes, leading to priming of tumor-specific CD4⁺ and CD8⁺ T cells (Fig. 3)⁴⁸.

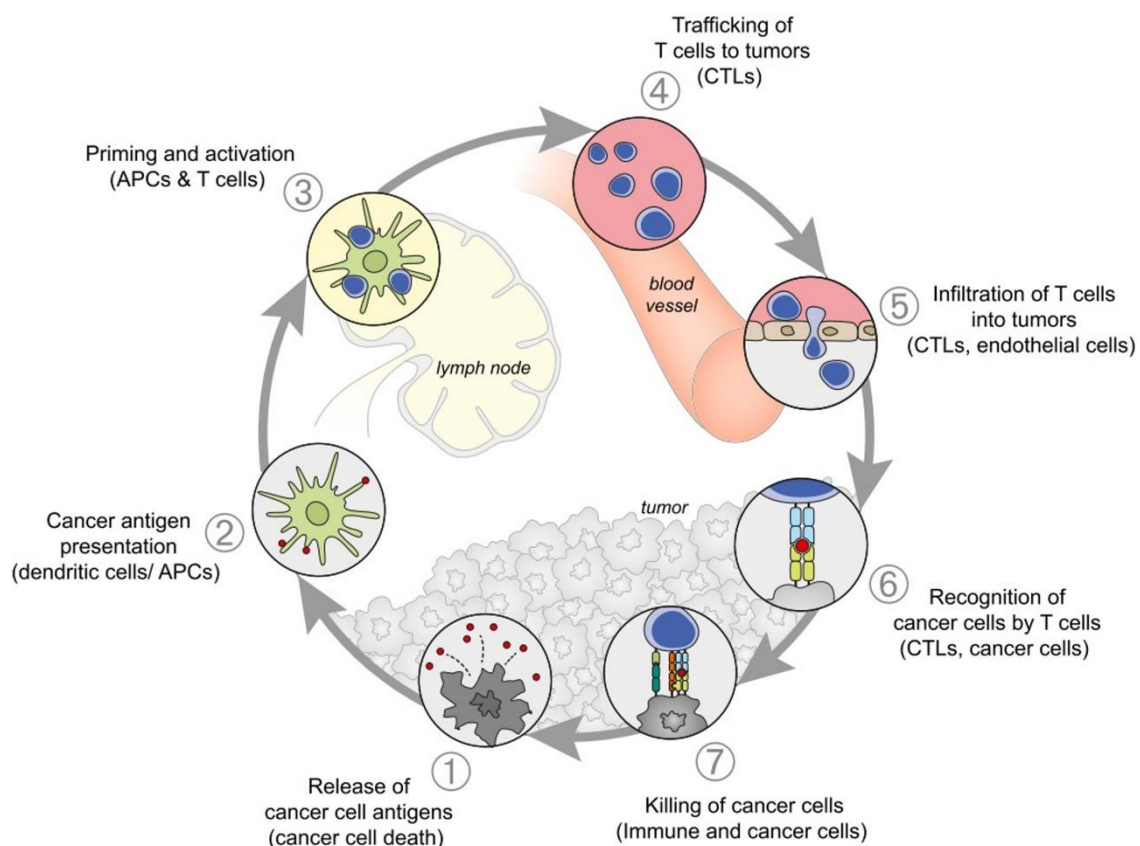


Figure 3: The cancer-immunity cycle (D.S. Chen and Mellman, 2013)⁵¹

Antigens released by cancer cells can be processed by APCs and presented to naïve T cells in lymph nodes. Following priming, activation, and differentiation, effector T cells infiltrate the tumor and trigger cell death of cancer cells upon recognition of their corresponding antigen. This leads to a renewed release of antigens and thus to a self-reinforcing cyclic process.

While mutations in the genome of neoplastic cells are mainly responsible for promoting and maintaining tumorigenesis, they also result in the expression of altered proteins. After processing of these proteins, tumor-specific peptides, called neoantigens, are presented on the tumor cell surface via MHC class I molecules, where they can be recognized by TCRs on CTLs and thus initiate a CD8⁺ T cell-mediated immune response⁵².

In case of tumor cell clones surviving the elimination phase, they enter a state of equilibrium with host immune cells. This equilibrium is likely to present the longest phase of the immunoeediting process, with proliferating tumor cells being kept in check by the host immune system. This state of persisting yet clinically nonprogressive neoplastic disease is referred to as cancer dormancy⁵³. At this point, the effector functions of the adaptive immune system are able to prevent the spread of tumor cells but cannot eliminate them completely. As a result of selection pressure on surviving cancer cells with consecutive genomic mutations, tumor cells can thus develop mechanisms that allow them to completely evade the immune system. This is referred to as tumor immune escape⁴⁸.

Tumor immune escape mechanisms are the result of a variety of genetic and epigenetic alterations. For example, loss or downregulation of human leukocyte antigen (HLA) class I molecules has been described in several tumor entities, including melanoma and CRC. This renders the corresponding tumor cells undetectable to CTLs, but at the same time more susceptible to NK-mediated lysis. There are several possible explanations for why tumors exhibiting loss of HLA class I molecules are nevertheless not consistently eliminated by NK cells alone. Pathways resulting in activation of NK cells include binding of natural killer group 2D (NKG2D) receptors to the stress-induced ligands MHC class I polypeptide-related sequence A and B (MICA/B). Therefore, simultaneous downregulation of these ligands as well as certain co-stimulatory molecules on tumor cells may impede NK activation. In addition, stimulatory interleukins and type I IFNs play a crucial role in NK activation in inflamed tissues but are not necessarily present in the TME, which further impairs NK-mediated tumor cell killing⁵⁴.

A similar escape mechanism resulting in impaired recognition of tumor cells by CTLs is the loss of tumor-specific antigens. 'Immunodominance' is a concept referring to an immune response that targets a single or very few antigens on malignant cells. Cell clones lacking the immunodominant antigen are therefore advantaged in tumor progression, resulting in tumor cell populations evading recognition by TCRs⁵⁵.

During immunosurveillance, death receptor signaling pathways play a central role in the initiation of apoptosis in tumor cells. Defects can occur at multiple sites in these pathways, such as downregulation and loss of Fas or TNF-related apoptosis-inducing ligand (TRAIL) receptors, promoting tumor immunoresistance⁵⁴. In addition, several tumor entities, including lung carcinomas, melanomas, and colon carcinomas, have been found to express functional

Fas ligands and therefore may be capable of inducing apoptosis themselves in Fas⁺ cells, including T cells⁵⁶⁻⁵⁸.

The identification of tumor immune escape mechanisms represents an important topic in cancer research because it could lead to a better understanding of why immunotherapeutic approaches fail in some cancer patients.

3.4 Immunotherapy

As described previously, our immune response to cancer is dependent on T cells recognizing neoplastic cells via cancer-associated antigens. However, the activation and effector functions of immune cells that would normally attack malignant cells and potentially lead to tumor regression are impaired by specific molecular pathways triggered by receptor to ligand interactions. The first checkpoint receptors to be discovered were PD-1 and CTLA-4, and the idea of blocking these immune checkpoints to enable the immune system to fight malignancies more effectively has since led to new approaches that have revolutionized cancer therapy⁵⁹. The first immunotherapeutic agent approved by both the FDA and the European Medicines Agency (EMA) in 2011 was the anti-CTLA-4 monoclonal antibody ipilimumab after it demonstrated prolonged survival in patients with metastatic melanoma⁶⁰.

Apart from TCRs recognizing their cognate antigen, provided it is presented via MHC molecules, the activation of T lymphocytes also depends on certain co-stimulatory signals. One important co-stimulatory receptor is CD28, which is expressed by all human CD4⁺ and around 50% of human CD8⁺ T cells. Interaction of CD28 with its ligands CD80 and CD86 on APCs results in T cell expansion and differentiation, promoting an antigen-specific T cell-mediated immune response. Within 48 hours of T cell activation, CTLA-4 expression is upregulated on the T cell surface⁶¹. Just as CD28, CTLA-4 functions as a receptor to CD80 and CD86 but has a higher affinity to these ligands⁶². Thus, it out-competes CD28 signaling, resulting in opposing effects, i.e., attenuation and inhibition of T cell activation. Several other inhibitory mechanisms mediated by CTLA-4 have been proposed, including secretion of soluble CTLA-4, indoleamine 2,3-dioxygenase (IDO) production, involvement of T_{regs}, and depletion of CD80 and CD86 by trans-endocytosis^{63,64}.

While CTLA-4 signaling is mainly localized in the secondary lymphoid organs where T cell activation occurs, clinical approaches using PD-1/PD-L1 blockade take effect directly in the TME. This is due to PD-L1 being expressed on several solid tumors, including lung-, colon cancer, and melanoma. Additionally, PD-1 expression is upregulated on tumor-infiltrating T lymphocytes⁶⁵. Interaction of PD-1 and PD-L1 is known to inhibit TCR-mediated proliferation of activated T cells. This effect has been shown to vary depending on TCR and co-stimulatory signaling strength, leading to the possibility that TCR or CD28 signaling may antagonize

PD-1-mediated immunosuppressive effects⁶⁶. Additionally, PD-L1 was found to bind to CD80 *in cis* on the same cell⁶⁷, preventing PD-1/PD-L1 interaction and thus inhibiting T cell-mediated effects. Since this type of *in cis* interaction occurs mainly on DCs, they play a pivotal role in immunotherapeutic approaches that block the PD-L1/PD-1 pathway. Therefore, it has been proposed that antibodies targeting PD-L1 exert additional effects in comparison to anti-PD-1 agents by disrupting not only the PD-L1/PD-1 interaction between tumor and T cells but also PD-L1/CD80 *in cis* binding on DCs. In this way, CD80 could be liberated for interaction with CD28, resulting in enhanced T cell proliferation and activation⁶⁸.

Checkpoint inhibitors targeting PD-1 (nivolumab, pembrolizumab) or PD-L1 (atezolizumab, avelumab, durvalumab) have been approved for a variety of cancers and have led to unprecedented improvement in patient outcomes. Nevertheless, only a minority of patients experience complete remission of tumor disease or benefit long-term⁶⁹. Therefore, as research moves toward personalized cancer therapy, it is essential to identify factors predicting an individual patient's response to immunotherapy. The seemingly most intuitive predictive biomarker for response to checkpoint blockade, i.e., tumor expression of PD-L1, proved to be inadequate. Thus, nivolumab has been approved for the treatment of advanced NSCLC regardless of PD-L1 expression status^{70,71}.

One biomarker that is generally considered predictive of the response to immune checkpoint blockade agents is the tumor mutational burden (TMB), i.e., the number of mutations within a megabase of tumor genome⁷². Since high TMB results in expression of neoantigens, predictive value can also be attributed to the latter. High TMB has been found to correlate with prolonged overall survival in melanoma patients treated with ipilimumab or tremelimumab, targeting CTLA-4,⁷³ as well as in patients with NSCLC tumors treated with pembrolizumab⁷⁴. However, both studies also identified tumors that displayed high TMB but did not respond well to therapy. Thus, even though TMB seems to be predictive overall, it is not sufficient to impart a good response to immune checkpoint blockade on its own.

3.5 Radiation therapy

Alongside surgery and chemotherapy, RT remains one of the most important modalities in cancer treatment. Approximately 50% of all cancer patients receive RT, which contributes to about 40% to curative treatment. Different types of cancer, however, differ significantly in their sensitivity to RT⁷⁵. Research suggests that tumor radiosensitivity depends, *inter alia*, on the cells' antioxidant capacity⁷⁶, alterations in onco- and tumor suppressor genes, DNA damage repair (DDR) mechanisms, regulatory mechanisms regarding cell cycle arrest, cancer stem cell formation, tumor metabolism, autophagic regulation, and changes in the TME⁷⁷. Treatment regimens using RT as a monotherapeutic approach, whether external beam radiation or

brachytherapy, primarily exploit the direct effects of ionizing radiation, i.e., induction of DNA damage with consecutive cell cycle arrest and cell death⁷⁸.

Ionizing radiation can either directly damage DNA by causing mutations and base modifications as well as DNA single- or double-strand breaks⁷⁹, or attack tumor cells by inducing chromosomal instability, plasma membrane or subcellular organelle damage⁷⁷. While direct effects result from energy deposition on DNA, irradiation also generates reactive oxygen species (ROS) that induce oxidative stress with accompanying alterations in cell proteins and lipids. This can lead to disruptions in various signaling pathways⁸⁰.

In addition to the effects on the tumor cells themselves, ionizing radiation also induces a mutagenic response in cells that are not directly exposed to it but are situated in close proximity⁸¹. These reactions are called bystander or off-target effects and are most likely exerted via long-lived radicals⁸², nitric oxide⁸³, and transmission of damage signals via gap junctions⁸⁴. As a result, neighboring cells experience oxidative stress as well as changes in gene expression and epigenetics⁸⁵.

Types of cell death that commonly result from irradiation include necrosis, autophagy-dependent cell death, and most importantly mitotic catastrophe and apoptosis. Apoptosis, or programmed cell death, is characterized by chromatin condensation, nuclear and DNA fragmentation, as well as blebbing of and formation of apoptotic bodies in the cell membrane⁸⁶. Radiation-induced apoptosis has been shown to be closely related to the expression of p53 in the tumor cell. Depending on the extent of DNA damage, activation of p53 can either promote cell survival through growth arrest and DNA repair or trigger cell death by apoptosis. Thus, p53 expression may represent a prognostic marker for radiosensitivity, with cells that suppress p53 activation being largely resistant to RT. Moreover, p53 activation after RT activates transcription of several proapoptotic genes, some of which play critical roles in triggering the intrinsic, or mitochondrial, apoptosis signaling pathway, leading to permeabilization of the outer mitochondrial membrane⁸⁷. As a result, several proteins are released from mitochondria into the cytosol, including cytochrome c. The latter forms a complex with cytosolic apoptotic protease-activating factor 1 (Apaf-1). This complex, called the apoptosome, then induces autoactivation of pro-caspase 9. Activated caspase 9 thereafter initiates a cascade of other caspase proteins that eventually induces apoptosis⁸⁸.

Apart from apoptosis, mitotic catastrophe resulting from impaired mitosis represents another important form of cell death induced by ionizing radiation. Due to disturbed chromosome segregation and cell division, cells undergoing mitotic catastrophe form envelopes around individual clusters of missegregated chromosomes. These micronuclei can be identified under a light microscope, allowing the cells to be easily distinguished from apoptotic tumor cells. Most malignant cells harbor mutations in genes involved in cell cycle checkpoints. As a result, damaged cells are no longer prevented from entering mitosis, so that mutations driving

carcinogenesis may in fact also promote cell death through mitotic catastrophe⁸⁹. Furthermore, irradiation of tumor cells causes prolongation of S and G₂ phases, resulting in premature initiation of mitosis and ultimately promoting mitotic catastrophe⁹⁰.

However, some tumor cells do not undergo cell death despite severe external and internal stress, but instead enter a senescent state with complete cell cycle arrest characterized by a unique gene expression pattern. Interestingly, some of these genes also play an important role in cancer development itself, leading to an ambivalent perception of senescence in cancer therapy⁹¹. In this context, the proinflammatory secretory phenotype of senescent cells has been found to cause or exacerbate side effects of chemotherapy such as fatigue, bone marrow suppression, as well as cardiac dysfunction, and may even promote cancer recurrence⁹².

Cancer therapies involving RT depend heavily on the aforementioned deleterious effects on tumor cells. Additionally, RT is known to have an impact on tumor immunogenicity. For example, it has been found that both the expression of MHC-I molecules on the cell surface and presentation of neoantigens are increased after irradiation⁹³. Furthermore, RT contributes to a pro-immunogenic TME by promoting DC activation and priming of effector T cells⁹⁴, as well as enhancing the expression of NKG2D ligands on tumor cells, rendering them susceptible to NK cells⁹⁵. Additionally, the expression of vascular adhesion molecules is augmented upon γ -irradiation, resulting in recruitment of tumor-specific T cells to the TME and differentiation of macrophages toward their tumoricidal M1 phenotype⁹⁶. High-dose irradiation enhances antitumor immunity through increased infiltration of CD8⁺ T cells and depletion of myeloid-derived suppressor cells (MDSC)⁹⁷, which normally contribute to the immunosuppressive network in cancer by inhibiting antigen-specific T cells via direct cell-cell contact⁹⁸. Hence, tumor regression following ablative radiation has even been found to be dependent on CD8⁺ T cell activity⁹⁹.

3.6 The cGAS/STING pathway

Regarding the immunomodulatory effects of RT, the cGAS/STING pathway is of utmost importance as its activation by cytosolic DNA ultimately leads to secretion of type I IFNs, which are known to mediate most of the effects explained above^{101,102}. In 2008, Ishikawa and Barber identified a molecule that induces expression of type I IFNs (IFN α and IFN β) in cells infected with DNA viruses. This molecule, residing primarily in the endoplasmic reticulum, has been termed stimulator of interferon genes (STING) and, in the presence of cytosolic DNA, activates transcriptional pathways via nuclear factor kappa B (NF- κ B) as well as interferon regulatory factor 3 (IRF3). In STING-knockout mice, plasmid DNA vaccination failed to elicit an effective innate immune response, highlighting the importance of STING protein in regulating the type I IFN-dependent immune response mediated by intracellular DNA^{103,104}.

The exact mechanism of how cytosolic DNA triggers STING-mediated effects remained unclear until the discovery of cyclic-GMP-AMP synthase (cGAS) in 2013. Predominantly localized in the cytosol, cGAS catalyzes the synthesis of cyclic guanosine monophosphate-adenosine monophosphate (cGAMP) from adenosine triphosphate (ATP) and guanosine-5'-triphosphate (GTP) upon binding to DNA but not RNA¹⁰⁵. In turn, newly synthesized cGAMP binds directly to STING and triggers downstream signaling cascades¹⁰⁶. Moreover, cGAMP can be transferred between adjacent cells via gap junctions, causing STING activation in neighboring cells as well¹⁰⁷.

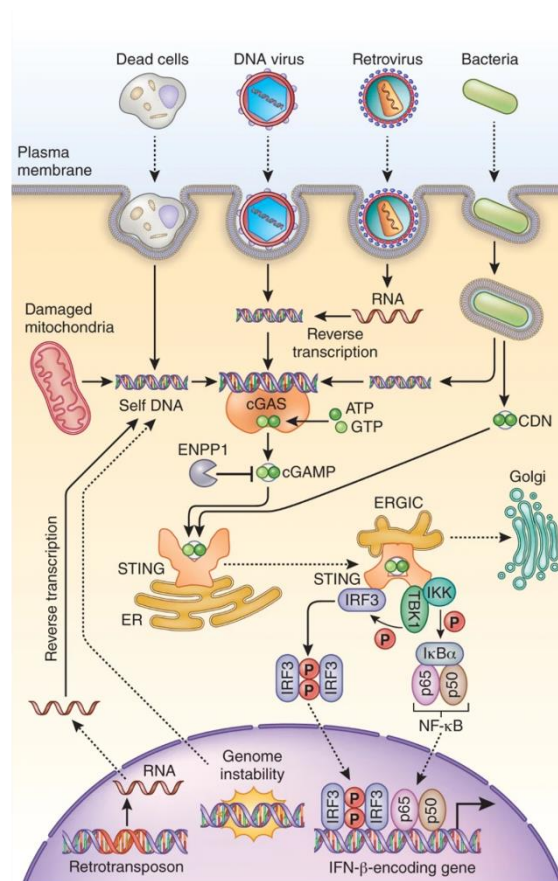


Figure 4. cGAS/STING pathway (Q. Chen et al., 2016)¹⁰⁰

DNA acts as a PAMP when it enters the cytosol from the nucleus, e.g., because of DNA damage by RT. It binds to and activates cGAS, triggering synthesis of cGAMP, which then binds to STING. STING activates TBK1, which in turn phosphorylates STING. IRF3 is recruited for phosphorylation by TBK1 and migrates to the nucleus, where it initiates the expression of type I interferons.

Upon binding to cGAMP, the STING protein changes its conformation toward a closed homodimer. After release of the C-terminal tail, which belongs to the transmembrane domain of the molecule, closed STING molecules form polymers stabilized by disulfide bridges. This process occurs in the endoplasmic reticulum and precedes translocation of ligand-bound STING polymers to the Golgi¹⁰⁸. Following activation by cGAMP, STING polymers recruit and form a complex with TANK binding kinase 1 (TBK1), which in return phosphorylates STING.

Remarkably, the conformation of the STING/TBK1 complex renders contact of the phosphorylation site Ser³⁶⁶ of the STING molecule with the active site of bound TBK1 impossible. Thus, the STING molecule phosphorylated by TBK1 is not the one that binds TBK1 directly, but its neighboring molecule within the STING polymer, while at the same time TBK1 dimers phosphorylate each other by trans-autophosphorylation. The phosphorylated motif in STING subsequently provides a binding site for IRF3 to recruit IRF3 for phosphorylation by TBK1. In addition to Ser³⁶⁶, Leu³⁷⁴ at the C-terminus of STING has also been found to be indispensable for IRF3 activation^{109,110}. After its phosphorylation and dimerization, IRF3 translocates to the nucleus, where it functions as a transcription factor and initializes the production of type I IFNs¹¹¹ (*Fig. 4*).

On the one hand, the immune response triggered by activation of the cGAS/STING pathway is part of the first line of defense against pathogens. On the other hand, persistent transcription of innate immune genes can cause pathologic inflammation and must be prevented by negative feedback mechanisms. To this end, another kinase, UNC-51-like kinase (ULK1), is also activated by cGAS and subsequently re-phosphorylates STING at Ser³⁶⁶ to mark it for degradation, thereby inhibiting STING-dependent IRF3 activity^{112,113}.

Cytosolic DNA, which leads to cGAS/STING activation and ultimately promotes the immune response via induction of type I IFNs, arises as a result of DNA damage in the nucleus. Moreover, micronuclei formed during mitosis following double-stranded DNA (dsDNA) breaks are also recognized by cGAS, thus triggering cGAS/STING pathway activation¹¹⁴.

The importance of the cGAS/STING pathway regarding tumorigenesis or tumor suppression, respectively, is clearly demonstrated by its role in the immune evasion of *TP53* mutated tumors. It was shown that mutant p53 interacts with TBK1, thus impeding the secretion of type I IFNs following initial pathway activation¹¹⁵. WT *TP53*, on the other hand, was found to trigger activation of the cGAS/STING pathway by promoting degradation of three prime repair exonuclease 1 (TREX1), resulting in enhanced occurrence of cytosolic DNA¹¹⁶.

3.7 Heat shock protein 90

Since cytosolic DNA occurs as a result of DNA damage and ultimately leads to improved tumor immunogenicity, interfering with DDR mechanisms may provide a potential means to further enhance this effect. A recent study confirmed that inhibition of DDR indeed causes release of DNA to the cytosol in tumor cells, which in turn triggers activation of the cGAS/STING pathway¹¹⁷.

A promising therapeutic target to impair DDR is the molecular chaperone heat shock protein 90 (HSP90), named according to its specific weight in gel electrophoresis. Molecular chaperones are proteins involved in the folding and assembly process of their structurally labile target

proteins, called clients¹¹⁸. Their activity is important for maintaining cell homeostasis under constantly changing conditions, including stress conditions. Major stress response pathways are the heat shock response (HSR) in reaction to proteome stress in the cytoplasm and the unfolded protein response following protein damage in the endoplasmic reticulum¹¹⁹.

The HSR is induced by binding of damaged proteins in the cytosol to chaperones such as HSP90, which prevents the stabilization of heat shock transcription factor 1 (HSF1) monomers by HSP90. As a result, HSF1 trimerizes, translocates to the nucleus, and eventually promotes transcription of genes encoding molecular chaperones and proteolytic enzymes, among others^{120,121}. The HSR therefore plays a critical role in maintaining cell integrity.

Additionally, HSF1 controls a transcriptional program that influences, for example, the cell cycle, regulation of apoptotic cell death, cellular adhesion molecules, and immune-associated signaling. Accordingly, continuous activation of the HSR was found to correlate with poor prognosis in breast-, colon-, and lung cancer patients¹²² while also promoting neoplastic growth in stromal cells¹²³.

HSP90 facilitates protein folding, assembly of multiprotein complexes, and binding of clients to their respective ligands¹²⁴, but unlike other heat shock proteins, it is hardly involved in de novo folding of proteins¹²⁵. These effects are dependent on binding and hydrolysis of ATP¹²⁶. HSP90 forms homodimers and recruits client proteins that can no longer be released after ATP binding and subsequent conformational changes of the HSP90/client complex. Activation and release of client proteins is then triggered by ATP hydrolysis. This process is further modified by post-translational modifications as well as by interactions with co-chaperones¹²⁷.

Despite its abundant presence in normal cells, HSP90 is a possible target protein in cancer therapy due to distinct differences of the HSP90 phenotypes between neoplastic and healthy cells. First, upregulation of HSP90 expression by HSF1 is said to be indispensable for tumor cell survival under challenging microenvironmental conditions. Moreover, mutation and deregulation in the cancer phenotype result in higher affinity for client proteins, rendering HSP90 more susceptible to pharmaceutical inhibitors in tumor tissue¹²⁸. HSP90, however, may facilitate oncogenesis by contributing to the maintenance of driver mutations. This is due to proteins with functional mutations being particularly unstable¹²⁹.

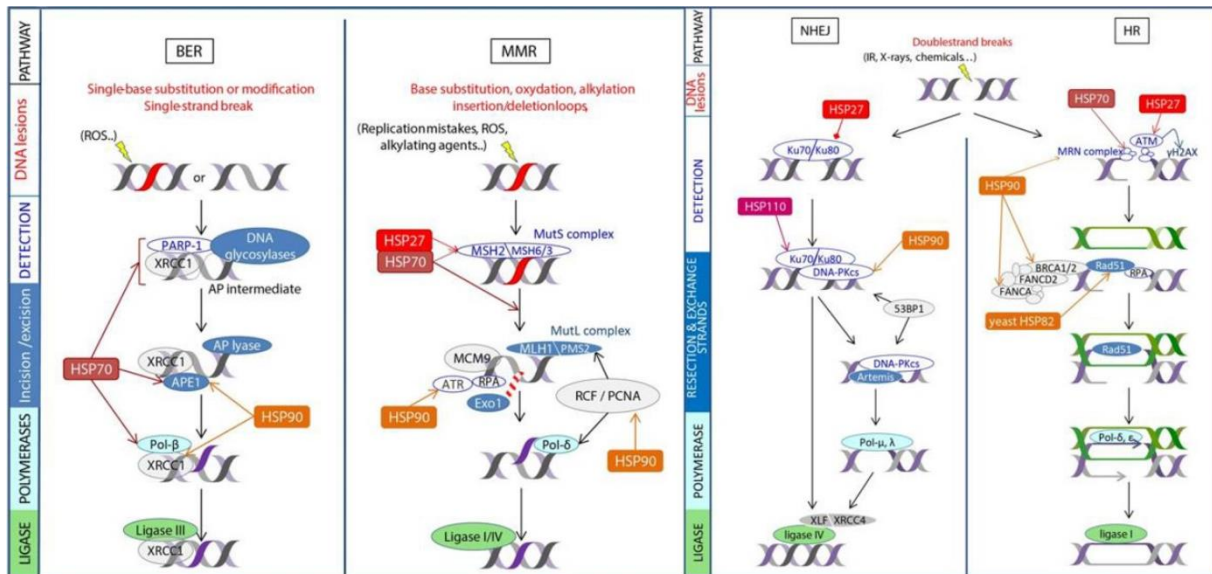


Figure 5: DNA damage repair signaling pathways (Dubrez et al., 2020)

DNA single-strand lesions, e.g., due to ROS or replication mistakes, activate mismatch repair (MMR), base excision repair (BER), or nucleotide excision repair (NER, not shown). DNA double-strand breaks, which can be induced by RT, additionally activate non-homologous end joining (NHEJ) and homologous recombination (HR). HSP90 plays a central role in the function of these pathways.

Apart from its intracellular effects, HSP90 can be secreted by normal cells under stress. Cancer cells, on the other hand, secrete HSP90 permanently, resulting in enhanced chaperoning of extracellular proteins. Thus, when secreted via exosomes, extracellular HSP90 mediates activation of matrix metalloproteinase 2 (MMP-2), human epidermal growth factor (HER-2), and plasmin, promoting tumor migration, invasion, and angiogenesis^{130,131}. In addition, HSP90 also functions as a tumor antigen following incorporation into the plasma membrane¹³².

The list of HSP90 clients includes over 200 different proteins¹³³. Apart from many proteins involved in various signaling pathways, e.g., kinases and transcription factors¹³⁴, these include molecules involved in DDR mechanisms such as MMR, base excision repair (BER), non-homologous end joining (NHEJ), and homologous recombination (HR) (Fig. 5). Inhibition of HSP90 therefore impairs said DDR mechanisms due to impaired stabilization and activation of said proteins¹³⁵. It was found that, first, low HSP90 expression is associated with longer survival in NSCLC patients, and second, in vitro treatment with an HSP90 inhibitor displays antiproliferative activity in NSCLC cells¹³⁶.

One challenge in implementing HSP90 inhibition in cancer therapy is the simultaneous induction of the HSR due to HSF1 also being a client of HSP90. This may be a possible explanation for the rather disappointing effects of HSP90-inhibiting drugs in the past. Further limiting factors include suppression of immune functions by HSP90 inhibition and toxicity to healthy cells^{137,138}. Because these factors drastically limit the maximum applicable dose of HSP90 inhibitors, monotherapeutic approaches have not proven effective enough in clinical

trials¹³⁹. Combined treatment regimens including HSP90 inhibition, RT, and immunotherapy are therefore an emerging field in cancer research.

3.8 TAS-116

Preclinical studies investigating the therapeutic effects of early HSP90 inhibitors yielded promising results in terms of reduced tumor cell proliferation rates. However, various severe adverse events that occurred in clinical trials highlighted the limitations of HSP90 inhibition as a monotherapeutic approach in cancer treatment¹⁴⁰.

In this thesis, the HSP90 inhibitor 3-ethyl-4-[4-[4-(1-methylpyrazol-4-yl)imidazol-1-yl]-3-propan-2-yl]pyrazolo[3,4-b]pyridin-1-yl]benzamide (TAS-116) was used in various experimental setups. In contrast to first-generation HSP90 inhibitors, TAS-116 specifically inhibits cytosolic HSP90 α and β , but not HSP90 paralogs such as GRP94 or TRAP1 in the endoplasmic reticulum or mitochondria, respectively. Because TAS-116 does not inhibit Cytochrome P450 (CYP450), an enzyme involved in the metabolism of many pharmaceutical agents, within the effective concentration range, a low drug-drug interaction potential allows for combined administration with other compounds. Additionally, TAS-116 has been found to accumulate in tumor tissue, providing a better side effect profile¹⁴¹.

The first in-human phase I study of TAS-116 was conducted from 2014 to 2017¹⁴². This trial enrolled 61 patients with advanced solid tumors in Japan and the United Kingdom who were no longer responding to standard treatment. TAS-116 was administered orally either daily for 5 days per week followed by 2 days without treatment, or every other day in doses of 160 mg/d or 340 mg/d, respectively. The most frequently reported treatment-related adverse events were diarrhea (83.6%), creatinine increase (55.7%), anorexia (50.8%), nausea (42.6%), eye disorder (32.8%), transaminase increase (32.8% for aspartate transaminase; 29.5% for alanine transaminase), and fatigue (29.5%). Serious adverse events occurred in 9.8% of patients. However, all of these resolved after interruption, dose reduction, or discontinuation of treatment.

At 38.9%, the best disease control rate was achieved in patients who received the 5 days on / 2 days off treatment scheme. Therefore, this regimen with a dose of 160 mg/d was further investigated in a phase II study involving 41 Japanese patients between 2016 and 2017¹⁴³. All patients suffered from gastrointestinal stromal tumors (GIST) refractory to the TKIs imatinib, sunitinib, and regorafenib. Although no patient in this study experienced complete or partial response, it should be noted that TAS-116 was herein administered as a fourth-line treatment or even later. Therefore, the median PFS of 4.4 months suggests important clinical activity. By comparison, phase II trials evaluating the HSP90 inhibitors ganetespib and luminespib in a third-line setting showed a PFS of 2.7 months and 3.9 months, respectively^{144,145}.

The efficacy of TAS-116 as a monotherapeutic approach in the fourth-line setting in patients with GIST was confirmed in a randomized, double-blind phase III study, which showed that it prolonged median PFS by 1.4 months and overall survival by as much as 6.2 months compared to placebo. However, the extension of overall survival may also be partly due to treatment with TKIs following study treatment¹⁴⁶. These results led to the first approval of TAS-116, under the name pimitespib, for treatment of GIST after progression under chemotherapy in Japan in 2022¹⁴⁷.

To date, pimitespib has not received approval from either the FDA or the EMA. Despite its clinical efficacy as a fourth-line therapy for GIST patients, there remains great potential for pimitespib to be of benefit to patients suffering from other cancers as well as to be effective as an earlier treatment approach. For the reasons described above, this increase in efficacy could be achieved by combination of pimitespib with immunotherapy and/or RT.

Combinatory treatment regimens involving pimitespib have already been the subject of several studies. In combination with sunitinib, pimitespib was found to be effective on imatinib-resistant cell lines and murine xenograft models¹⁴⁸. In a phase I trial, pimitespib in combination with nivolumab demonstrated promising antitumor activity, especially in MSS-CRC patients¹⁴⁹. Response to the study treatment was found to correlate with upregulation of the G2M checkpoint pathway and mutations of the DNA polymerase epsilon catalytic subunit (*POLE*) gene¹⁵⁰. The latter, however, is likely due to nivolumab treatment, as *POLE* mutations were shown to be associated with the effectiveness of anti-PD-1 monotherapy¹⁵¹. Another phase I study, investigating the effect of pimitespib in combination with imatinib in patients with GIST, is currently underway¹⁵².

3.9 Rationale

Although immunotherapeutic approaches currently represent a large field of cancer research and have contributed to remarkable improvements in the treatment of some cancer patients, the administration of immune checkpoint inhibitors is still associated with many limitations. While response rates are generally low in some common cancers, most patients who initially respond develop resistance over time¹⁵³. Because RT has been shown to improve tumor immunogenicity, combined treatment regimens that include both radiation and immunotherapy may be a way to overcome the limitations of immunotherapy alone.

The immunomodulatory effects of RT are predominantly mediated by type I IFNs after activation of the cGAS/STING pathway¹⁵⁴. Since the cGAS/STING pathway is triggered by the recognition of cytosolic dsDNA following DNA damage in the nucleus, such as in response to RT, inhibition of DDR mechanisms is a promising target to further enhance this effect.

In 2019, a study by Sen et al. confirmed that DDR inhibition in SCLC cells does indeed lead to increased cytosolic DNA appearance in vitro and that this results in activation of the cGAS/STING pathway and subsequent induction of IFN β secretion. In addition to the induction of various chemokines and recruitment of CD8⁺ T cells, the authors of this study also found upregulation of PD-L1 expression on the tumor cell surface upon DDR inhibition. The clinical implication of these findings was further underlined by demonstrating that the combination of DDR inhibition and anti-PD-L1 checkpoint blockade mediated synergistic anti-tumor benefits in SCLC in vivo models¹¹⁷. Therefore, DDR inhibition represents a promising means to enhance cGAS/STING-mediated immunomodulatory effects after RT in a synergistic manner, thereby improving tumor susceptibility to immunotherapeutic approaches such as PD-1/PD-L1 checkpoint blockade. To further illuminate this synergy in this thesis, the HSP90 inhibitor TAS-116 was applied to various murine tumor cell lines in vitro.

HSP90 clients include many proteins involved in DDR mechanisms¹³⁵, and HSP90 inhibition has previously been shown to sensitize tumor cells to the effects of RT¹⁵⁵. Combined treatment regimens with HSP90 inhibition and RT should thus increase tumor susceptibility to immune checkpoint blockade through increased activation of the cGAS/STING pathway.

In Japan, the drug pimitespib (TAS-116) is already approved for the treatment of refractory GIST tumors. However, tumor type-specific differences regarding treatment with TAS-116, especially in combination with RT, have been insufficiently investigated so far.

In this work, TAS-116 was therefore administered in combination with RT to various murine tumor cell lines in vitro to investigate cancer type-specific differences in terms of immunomodulatory effects. This may provide the basis for improved efficacy of immunotherapeutic approaches for a larger group of patients by maximizing the synergistic effects of HSP90 inhibition, RT, and immune checkpoint blockade.

4. Materials and methods

4.1 Materials

4.1.1.Devices

| Equipment | Company |
|-------------------------------------------------|--------------------------------------------------------------------------------------------------------------------|
| Cell culture centrifuge | HERMLE Labortechnik GmbH |
| Cell culture incubator | Axon Labortechnik GmbH |
| Cytoflex S | Beckman Coulter |
| Fluorescence Microscope AXIO Vert.A1 | Zeiss |
| Fluorescence microscope IX83 | Olympus (Center for Molecular Medicine Cologne – Microscopy Facility) |
| Heating and magnetic stirrer | Carl Roth |
| Laminar airflow cabinet (Biowizard Golden Line) | LMS |
| Light microscope CKX41SF | Olympus |
| Linear accelerator (SLi20) | Elekta (Klinik und Poliklinik für Radioonkologie, Cyberknife- und Strahlentherapie – Universitätsklinikum Köln) |
| Precision X-Ray MultiRad 160 | Faxitron |
| Tabletop centrifuge | LMS |
| Vortex | LMS |

4.1.2.Laboratory and cell culture material

| Material | Company |
|-------------------------------------------|----------------------------|
| 1, 2, 5, 10 ml syringes | BD |
| 1.5, 2 ml microcentrifuge tubes | VWR |
| 15, 50 ml polypropylene tubes | Corning |
| 5, 10, 25 ml serological pipettes | Sarstedt |
| 6-, 12-, 24-, 96-well cell culture plates | Corning |
| 60, 100 mm cell culture dishes | Corning |
| 70 µm cell strainer | VWR |
| Coverslips | VWR |
| LS columns | Miltenyi |
| Magnetic holder | Miltenyi |
| Neubauer chamber | Glaswarenfabrik Karl Hecht |
| Pipette 0.2-2 µl | Gilson |

| | |
|---------------------------------|----------------|
| Pipette 0.5-10 µl | Gilson |
| Pipette 100-1,000 µl | Gilson |
| Pipette 10-100 µl | Gilson |
| Pipette tips | VWR / Sarstedt |
| Sterile filter pipette tips | Sarstedt |
| Vacuum filtration system 0.2 µm | VWR |

4.1.3. Solutions

| Solution | Ingredients | Volume / Concentration |
|------------------------|-------------------------|------------------------|
| cDMEM | DMEM | 417 ml |
| | FBS | 10% |
| | L-glutamine | 6 ml |
| | NEAA | 6 ml |
| | Sodium pyruvate | 6 ml |
| | Sodium bicarbonate | 6 ml |
| | Penicillin/Streptomycin | 1% |
| | β-Mercaptoethanol | 0.00168% |
| MACS buffer | PBS (w/o Ca, Mg) | 500 ml |
| | BSA | 0.5% |
| | EDTA | 2 mM |
| Mowiol mounting medium | ddH ₂ O | 6 ml |
| | TRIS-HCl pH 8.5 (2 M) | 24% |
| | Glycerol | 12% |
| | Mowiol 4-88 | 9.8% |

4.1.4. Reagents

| Reagent | Company |
|-----------------------------------------------------------|---------------|
| 7-AAD viability staining solution (7-amino-actinomycin D) | BioLegend |
| Accutase cell detachment solution | BioLegend |
| ACK lysing buffer | Lonza |
| Ammonium chloride | Sigma-Aldrich |
| Anti-mouse PD-1 (RMP1-14) | BioXCell |
| BSA (bovine serum albumin) | VWR |
| CD8α microbeads | Miltenyi |
| Collagenase type IV | Gibco |

| | |
|----------------------------------------------------------|--------------------------------|
| DAPI solution (diamidino-2-phenylindole) | Thermo Scientific |
| DMEM (Dulbecco's modified eagle medium) | Gibco |
| DMSO (dimethyl sulfoxide) | AppliChem |
| DNase I from bovine pancreas | AppliChem |
| DPBS (Dulbecco's phosphate-buffered saline, with Ca, Mg) | Gibco |
| EDTA (ethylenediaminetetraacetic acid) | Sigma-Aldrich |
| FBS (fetal bovine serum) | Gibco |
| Geneticin (G418 sulfate) | Bertin Pharma |
| Glycerol | Carl Roth |
| Hoechst 33342 solution in water | Invitrogen |
| Isoflurane | Piramal |
| Ketamine | Zoetis Inc. |
| L-glutamine solution | Lonza |
| Methanol | Carl Roth |
| Mowiol 4-88 | Sigma-Aldrich |
| NEAA (non-essential amino acid) solution | Lonza |
| Paraformaldehyde | Merck |
| PBS (w/o Ca, Mg) | Gibco |
| Penicillin/Streptomycin | Gibco |
| Pharm Lyse lysing buffer | BD |
| Propidium Iodide solution | BioLegend |
| Purified anti-CD3e | BioLegend |
| Purified anti-mouse CD28 | BioLegend |
| Recombinant mouse IL-2 (carrier-free) | BioLegend |
| RPMI (Roswell Park Memorial Institute) medium | Gibco |
| Sodium bicarbonate solution | Biozym |
| Sodium pyruvate | Thermo Scientific |
| Tag-it violet proliferation and cell tracking dye | BioLegend |
| TAS-116 | Taiho Pharmaceutical Co., Ltd. |
| TRIS hydrochloride (Tris-aminomethane) | Carl Roth |
| Triton X-100 | Sigma-Aldrich |
| Trypan blue solution | Sigma-Aldrich |
| Trypsin-EDTA (10x) | Gibco |
| Tween 20 | Carl Roth |
| Xylazine | Bayer |

| | |
|------------------------------------|---------------|
| Zombie green fixable viability kit | BioLegend |
| Zombie NIR fixable viability kit | BioLegend |
| β -Mercaptoethanol | Sigma-Aldrich |

4.1.5. Antibodies

(1) Antibodies for flow cytometry

| Target | Clone | Fluorophore | Company |
|-------------------------------------------|-------------|-----------------|-----------|
| CD4 | RM4-5 | BV650 | BioLegend |
| CD45 | 30-F11 | FITC | BioLegend |
| CD8 α | 53-6.7 | BV510 | BioLegend |
| CD8 α | 53-6.7 | FITC | BioLegend |
| PD-L1 | 10F.9G2 | PE/Dazzle | BioLegend |
| PD-L2 | TY25 | APC | BioLegend |
| TCR <i>Vα11.1, 11.2</i> | RR8-1 | PE | BioLegend |
| TCR <i>Vα2</i> | B20.1 | Alexa-700 | BioLegend |
| TCR <i>Vα3.2(b,c)</i> | RR3-16 | PE | BioLegend |
| TCR <i>Vα8.3</i> | KT50 | PE | BioLegend |
| TCR <i>Vβ11</i> | KT11 | PerCp-Cy5.5 | BioLegend |
| TCR <i>Vβ11</i> | RR3-15 | PE | BioLegend |
| TCR <i>Vβ12</i> | MR11-1 | PE | BioLegend |
| TCR <i>Vβ13</i> | MR12-4 | PE | BioLegend |
| TCR <i>Vβ2</i> | B20.6 | Alexa Fluor 647 | BioLegend |
| TCR <i>Vβ5.1, 5.2</i> | MR9-4 | PE-Cy7 | BioLegend |
| TCR <i>Vβ6</i> | RR4-7 | APC | BioLegend |
| TCR <i>Vβ7</i> | TR310 | PE | BioLegend |
| TCR <i>Vβ8.1, 8.2</i> | KJ16-133.18 | Alexa Fluor 647 | BioLegend |
| TCR <i>Vβ8.3</i> | 1B3.3 | PE | BioLegend |
| TCR <i>Vβ9</i> | MR10-2 | PE | BioLegend |

(2) Antibodies for immunofluorescence staining

| Antibody | Clone | Company |
|----------------------------------------|----------|-----------|
| Alexa Fluor 488 donkey anti-mouse IgG | ab150105 | Abcam |
| Alexa Fluor 555 donkey anti-rabbit IgG | Poly4064 | BioLegend |
| Alexa Fluor 647 donkey anti-rabbit IgG | Poly4064 | BioLegend |

| | | |
|---------------------------------------|-----------|----------------|
| dsDNA mouse | 35I9 DNA | Abcam |
| IFN beta rabbit | PA5-20390 | Invitrogen |
| Phospho-histone H2A.X (Ser139) rabbit | 20E3 | Cell Signaling |
| Phospho-STING (Ser365) rabbit | D1C4T | Cell Signaling |

4.1.6. Software

| Software | Version |
|------------------|----------|
| CytExpert | 2.3.1.22 |
| EndNote | X9.3.3 |
| GraphPad Prism | 9.4.1 |
| Image J | 1.53k |
| Microsoft Office | 2209 |

4.2 Methods

4.2.1. Cell lines

Tumor cells were cultured on 100 mm sterile polystyrene Petri dishes in 10 ml full cell culture medium containing 1% Penicillin/Streptomycin and 10% fetal bovine serum (FBS). Cells adherent to plastic were washed with phosphate-buffered saline (PBS) prior to detachment with 5 ml trypsin or accutase for five minutes at 37°C. All cells were cultured at 37°C and 5% CO₂. Cell counting for all experiments was performed using a counting chamber after suspension in trypan blue.

(1) Small cell lung cancer – RP157.8

RP157.8 is a murine SCLC cell line driven by both *RB1* and *Trp53* knockout. Since these cells were derived from a liver metastasis, they grow adherently and therefore require detachment with accutase or trypsin. This cell line was kindly provided by the group of Prof. Dr. Dr. Roland Ullrich.

(2) Non-small cell lung cancer – ACF135.10

The murine ACF135.10 (KP135.10) NSCLC cell line harbors a *Trp53* knockout as well as a *KRAS* mutation. The cells are adherent to plastic and were cultured as described above. This cell line was kindly provided by the group of Prof. Dr. Christian Reinhardt.

(3) Colon carcinoma – MC38

MC38 is a murine adenocarcinoma cell line of the colon derived from a C57BL/6 mouse. Since MC38 cells are of epithelial origin, they grow adherently to plastic. This cell line was kindly provided by PD. Dr. Hans Schlösser's group.

(4) Melanoma – B16F₁₀

B16F₁₀ is a metastatic clone of the spontaneous murine melanoma cell line B16F₀. B16F₁₀ cells do not express the tumor suppressor proteins p16^{Ink4a} and p19^{Arf} due to a deletion of exons 1 α , 1 β and 2 of the *Ink4a/Arf* locus¹⁵⁶. The cells are adherent to plastic and have an epithelial morphology. This cell line was kindly provided by the group of Prof. Dr. Dr. Roland Ullrich.

(5) Lymphoma – E.G7

The E.G7 cell line is a derivative of the EL4 lymphoma cell line induced in a C57BL/6 mouse by 9,10-dimethyl-1,2-benzanthracene. EL4 cells were transfected with a plasmid containing a cDNA copy of chicken-derived ovalbumin mRNA, the human β -actin promoter, and the neomycin resistance gene. Thus, the E.G7-OVA line continuously synthesizes and secretes ovalbumin and the peptide OVA₂₄₂₋₂₈₅ is subsequently presented on the cell surface via MHC-I molecules¹⁵⁷. Selection of transfected cells was ensured by supplementing 0,4 mg/ml G418 (Geneticin) to the cell culture medium. This cell line was kindly provided by PD. Dr. Hans Schlösser's group.

4.2.2. OT-I mice

Transgenic OT-I mice originate from a C57BL/6 background and are genetically modified to express the TCRs *V α 2* and *V β 5*, which are designed to recognize the ovalbumin peptide OVA₂₅₇₋₂₆₄¹⁵⁸. These mice produce CD8⁺ T lymphocytes specific for the OVA₂₅₇₋₂₆₄ peptide when presented via MHC class I H-2Kb molecules. They also show a greater proportion of CD8⁺ T cells to total T lymphocytes than non-transgenic animals¹⁵⁹ and can be used to study CD8⁺ T cell-mediated immune responses.

Mice were kept in groups of two to five animals per cage in a 12-hour dark/light cycle with unrestricted access to food and water under specific pathogen-free conditions. All animal experiments were performed in accordance with the animal experiment guidelines of the German Animal Welfare Act according to a protocol approved by the District Government of Cologne (Animal Experiment Application 81-02.04.2019.A179). Appropriate measures were taken to minimize pain or discomfort. Individual evaluation forms were completed and signed daily for each mouse.

4.2.3. Isolation and activation of T cells

CD8⁺ T cells were isolated from splenocytes of OT-I transgenic mice. To obtain a single-cell suspension, the dissected spleen was triturated through a 70 µm cell strainer, rinsed with MACS buffer, and centrifuged at 500 g for five minutes. Splenocytes were suspended in 500 µl MACS buffer and magnetically labeled with 20 µl of CD8 microbeads for 30 minutes on ice. Cells were then added to 20 ml MACS buffer, centrifuged at 500 g for five minutes at 4°C, resuspended in 5 ml MACS buffer, and the suspension was filtered through a cell strainer to prevent clumping in subsequent steps. The cell suspension was applied to an LS MACS column previously moistened with 5 ml MACS buffer in a magnetic field and unlabeled cells were flushed out of the column with 8 ml of MACS buffer. The column was then removed from the magnetic field and CD8⁺ T cells were collected by washing twice with 5 ml MACS buffer. After centrifugation at 500 g for five minutes at 4°C, the isolated T cells were resuspended in complete Eagle's minimal essential medium (cDMEM) supplemented with 1000 U/ml recombinant mouse interleukin-2 (IL-2) and anti-mouse CD28 (1:100) to induce differentiation into cytotoxic CD8⁺ T lymphocytes. The cell suspension was transferred onto a 24-well plate that had been coated 24 hours prior with anti-CD3e (1:100 in PBS) and cells were then stored at 37°C for three days.

On the third day after activation, CD8⁺ T cells were harvested, centrifuged at 500 g for five minutes at 4°C, and resuspended in cDMEM supplemented with 1000 U/ml IL-2. The cell suspension was then transferred to a new plate and stored at 37°C. The CD8⁺ OT-I T cells were used five days after isolation and activation.

4.2.4. TAS-116

TAS-116 (Taiho Pharmaceutical Co., Ltd.) was dissolved in dimethyl sulfoxide (DMSO) at a concentration of 20 mM and stored at -20°C. Working solutions were stored at -4°C for a limited time. For intraperitoneal injection in mice, the application volume was adjusted by diluting the stock solution in 95% PBS and 5% Tween 20.

4.2.5. TAS-116 cytotoxicity assay

The tumor type-dependent cytotoxicity of the HSP90 inhibitor TAS-116 was determined by titration of the reagent and measurement of consecutive cell death by staining with 7-amino-actinomycin D (7-AAD), a fluorescent DNA-binding agent that intercalates between cytosine and guanine bases but is excluded by intact cells¹⁶⁰.

For this purpose, cells were transferred to a 96-well plate at a density of 10⁵ cells per well in 100 µl cell culture medium containing 1% Penicillin/Streptomycin and 10% FBS, and adherent

cells were allowed to settle overnight. Cells were then treated with the reagent TAS-116 in concentrations ranging from 0.01 μM to 10,000 μM or the diluent DMSO, respectively.

Cells growing in suspension were centrifuged at 500 g for five minutes at 4°C 24 hours after treatment. Adherent cells were incubated with trypsin for five minutes at 37°C and transferred to a new plate prior to centrifugation. After washing once with 1% bovine serum albumin (BSA) in PBS, cells were centrifuged again at 500 g for five minutes at 4°C and resuspended in 1% BSA in PBS containing 1.5 μl 7-AAD per well. Staining was performed for 30 minutes at 4°C in the dark. Cells were then washed once with PBS and resuspended in 100 μl PBS for subsequent flow cytometric analysis.

4.2.6. Viability assay after TAS-116 treatment and irradiation

To quantify the susceptibility of cells to cell death induced by irradiation alone and in combination with TAS-116 treatment, a viability assay was performed for each cell line.

Cells were transferred to 24-well plates at a density of 3×10^4 cells per well in 500 μl cell culture medium containing 1% Penicillin/Streptomycin and 10% FBS and allowed to settle overnight. The next day, cells were treated with concentrations of TAS-116 known to be subtoxic to each cell line tested, i.e., 0.5 μM and 10 μM , or the diluent DMSO, respectively. One hour after treatment, cells were irradiated with 2, 4, 8, 10, and 12 Gy using an X-ray irradiation system (MultiRad 160 by Faxitron®). Irradiation was performed at 160 kV with a tube current of 25 mA at 1.9 Gy/s.

Six hours after irradiation, cell culture plates were centrifuged at 500 g for five minutes at 4°C and the medium containing TAS-116 was carefully removed. Fresh medium containing 1% Penicillin/Streptomycin and 10% FBS was added, and the cells were maintained at 37°C until the fifth day post irradiation.

Propidium Iodide (PI) at a dilution of 1:100 and Hoechst 33342 diluted 1:10,000 were added to the cell culture medium 72 hours after irradiation and incubated for 30 minutes at 37°C in the dark. Similar to 7-AAD, the nuclear stain PI can be used to assess cell viability because it does not stain cells with an intact plasma membrane¹⁶¹. Hoechst 33342, on the other hand, binds to adenine-thymine-rich regions of DNA and, due to its ability to penetrate the cell membrane, stains live cells as well¹⁶².

After staining, cells were centrifuged at 500 g for five minutes at 4°C to attach dead cells to the bottom of the plate, and the proportion of PI positive cells, i.e., cells that had undergone cell death, was examined using a fluorescence microscope (Zeiss AXIO Vert.A1). The total number of cells per image was determined by counting the cell nuclei in the blue channel (Hoechst 33342), and the percentage of cells that were also positive for PI staining was calculated. For each condition, an average of approximately 170 cells were counted.

4.2.7. Analysis of cGAS/STING pathway activation

(1) DNA double-strand breaks - γ H2AX

To analyze the induction of DNA double-strand breaks by combination therapy with TAS-116 and RT, immunofluorescence staining was performed for phosphorylated histone H2AX (γ H2AX). Histone H2AX is phosphorylated at ser¹³⁹ within seconds of inducing of DNA double-strand breaks and subsequently forms foci, each representing a single double-strand break¹⁶³. Cells were transferred to coverslips in 24-well plates at a density of 3×10^4 cells per well in 500 μ l cell culture medium containing 1% Penicillin/Streptomycin and 10% FBS and allowed to settle overnight. One hour after treatment with 0.5 μ M, 10 μ M TAS-116, or the diluent DMSO, the next day, cells were irradiated as described above.

Fixation by incubation in 4% paraformaldehyde (PFA) solution for 15 minutes at room temperature was performed three hours after irradiation to not only assess the induction of DNA double-strand breaks, but also to distinguish the extent of DDR. The coverslips were then transferred to new 24-well plates and stored in 1 ml PBS each until immunofluorescence staining.

To block unreacted formaldehyde groups and reduce background fluorescence, cells were quenched with 50 mM ammonium chloride (NH_4Cl) for 15 minutes at room temperature and then washed with PBS for five minutes. Cells were permeabilized with 0,1% Triton-X100 for ten minutes at room temperature, washed once with PBS and blocked with 5% BSA in PBS for two hours at room temperature. The primary antibody targeting γ H2AX was diluted 1:1,000 in 1% BSA in PBS and applied to the samples overnight at 4°C in a wet chamber.

The next day, samples were washed three times with 1% BSA in PBS, and the secondary antibody Alexa Fluor 647 anti-rabbit (1:250 in 1% BSA-PBS) was applied for one hour in a wet chamber at room temperature in the dark. Finally, cells were washed twice in PBS, stained with 1 μ g/ml diamidino-2-phenylindole (DAPI) for five minutes in the dark, washed with PBS and once with double-distilled water (ddH_2O) and mounted with Mowiol.

(2) Cytosolic double-stranded DNA

It has been previously described that irradiation-induced DNA damage leads to an increased occurrence of cytosolic dsDNA¹⁰¹. To determine whether HSP90 inhibition exacerbates this effect, immunofluorescence staining for cytosolic dsDNA was performed.

Cells were transferred to coverslips in 24-well plates at a density of 3×10^4 cells per well in 500 μ l cell culture medium containing 1% Penicillin/Streptomycin and 10% FBS and allowed to settle overnight. The next day, cells were treated with 0.5 μ M, 10 μ M TAS-116, or the diluent DMSO, respectively, and irradiated one hour later as described above.

Fixation of samples was performed as described above three hours after irradiation.

To block unreacted formaldehyde groups and reduce background fluorescence, cells were quenched with 50 mM ammonium chloride for 15 minutes at room temperature and then washed in PBS for five minutes. Cells were permeabilized with 0,02% Tween20 in PBS for 15 minutes at room temperature to prevent the primary antibody from entering the nucleus¹⁶⁴. Samples were washed once in PBS and blocked with 5% BSA in PBS for two hours at room temperature. The primary antibody against dsDNA was diluted 1:1,000 in 1% BSA in PBS and applied to the samples overnight at 4°C in a wet chamber.

The next day, the samples were washed three times with 1% BSA in PBS, and the secondary antibody Alexa Fluor 488 anti-mouse (1:1,000 in 1% BSA in PBS) was applied for one hour in a wet chamber at room temperature in the dark. Lastly, cells were washed twice in PBS, stained with 1 µg/ml DAPI for five minutes in the dark, washed with PBS and once with ddH₂O and mounted with Mowiol.

(3)STING phosphorylation

To quantify the activation of the cGAS/STING pathway induced by irradiation and HSP90 inhibition, immunofluorescence staining for phosphorylated STING protein (pSTING) was performed for each cell line.

Preparation, treatment with TAS-116, and irradiation were carried out as described above, and cells were fixed using 4% PFA eight hours after irradiation. Immunofluorescence staining was performed according to the previously mentioned protocol with slight differences in terms of permeabilization of the tumor cells, which was achieved by incubating the samples in ice-cold methanol on ice for ten minutes¹⁶⁵. After blocking with 5% BSA in PBS the primary antibody targeting pSTING (1:400 in 1% BSA in PBS) was applied overnight at 4°C in a wet chamber. The protocol was then continued as described above, using Alexa Fluor 647 anti-rabbit diluted 1:250 in 1% BSA in PBS as the secondary antibody.

(4)IFNβ

Because HSP90 is also known to stabilize the protein kinase TBK1, which is involved in the cGAS/STING pathway¹⁶⁶, the possibility of incomplete pathway activation despite STING phosphorylation was ruled out by analyzing IFNβ secretion as one of the main effects of complete cGAS/STING pathway activation¹⁶⁷.

Immunofluorescence staining according to the known protocol was therefore conducted again for each cell line after treatment with TAS-116 and irradiation with doses up to 12 Gy. Fixation was performed 48 hours after irradiation. Tumor cells were permeabilized by incubation in 0.1% Triton-X100 for ten minutes at room temperature. The primary antibody targeting IFNβ

was diluted 1:50 in 1% BSA in PBS and, after overnight incubation, conjugated with the secondary antibody Alexa Fluor 555 anti-rabbit at a dilution of 1:300 in 1% BSA in PBS.

(5)Quantification of fluorescence signal intensity

Images of cells stained for γ H2AX, dsDNA, pSTING, and IFN β were acquired using a fluorescence microscope (Olympus IX83), and signal intensity analysis was performed using ImageJ software. First, regions of interest (ROI) were defined for each nucleus in the blue channel (DAPI). For this purpose, the blue channel was converted to a binary black and white image and a threshold for DAPI staining intensity was set. Next, the existing “convert to mask” and “watershed” commands were applied to best distinguish individual nuclei. Particles with a minimum size of 1,000 pixels and minimum circularity of 0.2 were defined as ROIs and fluorescence parameters of these nuclei were measured. The ROIs were then transferred as an overlay to the respective channel, i.e., the magenta (γ H2AX, pSTING), green (dsDNA) or red channel (IFN β), and the fluorescence parameters for the respective staining were also measured.

To quantify γ H2AX staining in the nuclei, the mean integrated density of ROI in the magenta channel was analyzed. Analysis of dsDNA, pSTING, and IFN β staining required measurement of staining intensity in the cytosol, which is not included in the ROI. Therefore, cells in each channel were outlined by freehand selection. The integrated density of the nucleus, i.e., the ROI, was then subtracted from that of the corresponding whole cell, and the mean integrated density within the cytosol was normalized to an untreated control sample for each staining. An average of 16 cells per condition was analyzed.

4.2.8.CD8⁺ T cell-mediated killing assay

It has been previously shown that the anti-tumor immune response following DNA damage and activation of the cGAS/STING pathway is mainly mediated by the recruitment of CD8⁺ T lymphocytes¹¹⁷. To assess whether a combination treatment of HSP90 inhibition and RT could enhance this effect, a CD8⁺ T cell cytotoxicity assay was performed. To this end, RP157.8 SCLC and ACF133.3 cells, another subset of the previously used ACF135.10 NSCLC cell line, were transfected to secrete ovalbumin as described above for the E.G7 lymphoma cell line.

RP157.8-OVA and ACF133.3-OVA cells were transferred to 6-well plates at a density of 2×10^5 cells per well in cell culture medium containing 1% Penicillin/Streptomycin and 10% FBS as well as 0,4 mg/ml G418 to maintain positive selection. The next day, cells were treated with 0.5 μ M, 10 μ M TAS-116, or the diluent DMSO, respectively, and irradiated with 8 Gy one hour later as previously described. Cells were kept on ice during irradiation, and the non-irradiated

control group was likewise kept on ice for the same time. Immediately after irradiation, the medium was carefully removed and replaced with fresh cell culture medium supplemented as described above.

Two days after irradiation, cells were incubated in 1 ml 5 μ M Tag-it-violet in PBS for 20 minutes at room temperature in the dark. After the tagging process was terminated by adding 5 ml of cell culture medium, cells were centrifuged at 500 g for five minutes at 4°C and transferred to a 96-well plate at a density of 10^4 cells per well in medium supplemented as described above. 72 hours post irradiation, 3×10^5 OT-I CD8⁺ T cells in cDMEM supplemented with 1000 U/ml IL-2 as well as 10 μ g/ml anti-PD1 antibody were added to the tumor cells. Cells were co-cultured at 37°C for five hours before the supernatant containing CD8⁺ T cells was transferred to a new 96-well plate. Tumor cells were washed with 50 μ l of PBS before detachment with 50 μ l of accutase per well for seven minutes at 37°C. They were then again transferred to the CD8⁺ T cells and co-cultured cells were centrifuged at 500 g for five minutes at 4°C and washed once with 200 μ l per well 1% BSA in PBS. Cells were then resuspended in 50 μ l per well 1% BSA in PBS containing 1.5 μ l of 7-AAD and anti-CD8 α FITC antibody 1:100 and stained for 30 minutes at 4°C in the dark. After staining, cells were washed once in PBS, resuspended in 100 μ l per well of PBS and analyzed by flow cytometry.

The same procedure was performed on tumor cells without co-cultured CD8⁺ T cells. These cells were not stained with 7-AAD but were incubated for 30 minutes at 4°C in the dark in 50 μ l per well 1% BSA in PBS containing anti-PDL1 PE/Dazzle and anti-PDL2 APC antibodies, each at a dilution of 1:200, prior to flow cytometric analysis.

4.2.9. Analysis of TCR clonality

ACF135.10 NSCLC cells were harvested from cell culture plates as previously described and washed once with PBS. Cell density was adjusted to 5×10^7 cells/ml in PBS and 100 μ l of the cell solution was injected subcutaneously into both flanks of C57BL/6 WT mice anesthetized with isoflurane.

Once the tumors had grown to approximately 300 mm³, the mice were treated with 16 mg/kg TAS-116 by intraperitoneal injection and irradiated one hour later. Animals were anesthetized by intraperitoneal injection of ketamine (100 mg/kg) and xylazine (10 mg/kg) before irradiation. Cream was applied to protect the mice' eyes from drying out during anesthesia and animals were kept under observation until awakening.

Mice received a single dose of 8 Gy per tumor delivered by a linear electron accelerator (Elekta SLi20). To increase the radiation dose at the skin surface, the tumor region was covered with a 5 mm wax bolus. Irradiation was performed at a dose rate of approximately 3.5 Gy/min at 15 MeV.

The mice were terminated one hour after irradiation, and the tumors and spleen were dissected. Blood was collected from the heart and diluted 1:10 in Pharm Lyse before incubation in a water bath at 37°C for 15 minutes. After centrifugation at 400 g for four minutes at room temperature, the cell pellet was resuspended in 1 ml PBS and stored on ice until staining.

The tumors were cut into pieces and digested in 1 ml / 100 mg tissue of pre-warmed Roswell Park Memorial Institute medium (RPMI) containing 10% FBS, collagenase IV 1:1,000, and deoxyribonuclease (DNase) 1:200 for 50 minutes in a water bath at 37°C. The tumor pieces were then triturated through a 70 µm cell strainer and rinsed twice with 5 ml RPMI containing 10% FBS. Cells were centrifuged at 500 g for five minutes at 4°C, resuspended in 5 ml PBS, and stored on ice until staining.

The spleen was likewise passed through a cell strainer and rinsed twice with 5 ml PBS. Following centrifugation at 500 g and 4°C for five minutes, the cells were resuspended in 1 ml lysing buffer and incubated at room temperature for five minutes. After addition of 5 ml PBS, splenocytes were centrifuged again at 500 g and 4°C for five minutes, then resuspended in 5 ml PBS and stored on ice until staining.

| | | I | II | III | IV | V | VI | VII | VIII | IX |
|--------|-----------------|--------------|------------|-----|------|------|-------------|-----|-------|-------|
| 405 nm | BV510 | CD8α | | | | | | | | |
| | BV650 | CD4 | | | | | | | | |
| 488 nm | FITC | CD45 | | | | | | | | |
| | PerCp-Cy5.5 | Vβ11 | | | | | | | | |
| 561 nm | PE | Vα11.1, 11.2 | Vβ12 | Vβ9 | Vβ11 | Vβ13 | Vα3.2 (b,c) | Vβ7 | Vβ8.3 | Vα8.3 |
| | PE-Cy7 | Vβ5.1, 5.2 | | | | | | | | |
| 633 nm | APC / Alexa 647 | Vβ6 | Vβ8.1, 8.2 | Vβ2 | | | | | | |
| | Alexa-700 | Vα2 | | | | | | | | |
| | APC-Cy7 | Zombie Nir | | | | | | | | |

Figure 6: Flow cytometry panel for TCR staining

Samples were stained with Zombie Nir 1:500 in PBS for 30 minutes at room temperature in the dark. All other antibodies were diluted 1:40 in PBS and staining was performed for 20 minutes at 4°C in the dark.

Prior to staining, all samples were centrifuged at 500 g and 4°C for five minutes. Splenocytes and blood cells were resuspended in 100 µl, tumor samples were resuspended in 500 µl Zombie Nir 1:500 in PBS and incubated for 30 minutes at room temperature in the dark. After washing once with PBS, blood and tumor samples were resuspended in 6 ml, splenocytes in 2 ml of PBS. All samples were aliquoted at 40 µl per well onto a 96-well plate. To each well,

10 μ l of PBS containing 0.25 μ l of each antibody was added according to the panel in *Fig. 6*, and incubation was performed for 20 minutes at 4°C in the dark. Staining was then terminated by addition of 100 μ l PBS, cells were centrifuged for five minutes at 500 g and 4°C, washed once with 200 μ l PBS, resuspended in 100 μ l PBS, and measured by flow cytometry.

5. Results

5.1 Cell line specific cytotoxicity of TAS-116

To administer the HSP90 inhibitor TAS-116 in effective yet subtoxic concentrations in the following experiments, the tumor type-specific cytotoxicity of the compound was determined for ACF135.10 NSCLC, RP157.8 SCLC, MC38 colon carcinoma, B16F₁₀ melanoma, and E.G7 lymphoma cells (*Fig. 7*). For this purpose, cells were treated with concentrations ranging from 0.01 μM to 10,000 μM TAS-116, or the diluent DMSO, respectively. FACS analysis of 7-AAD positive, i.e., dead cells, was performed 24 hours after treatment. While no effect was observed in any cell line when treated with the lowest concentration (0.01 μM), all cells underwent cell death within 24 hours of treatment with 10,000 μM . Thus, it was confirmed that the concentration range in this experimental design was sufficiently chosen to evaluate cytotoxicity for each cell line included in this study.

Survival curves and IC₅₀ values, i.e., cell line-specific concentrations of TAS-116 that induce cell death in 50% of the original cell population, were calculated using a non-linear regression model. IC₅₀ values were comparable for ACF135.10 (115.1 μM ; *Fig. 7A*), RP157.8 (168.4 μM ; *Fig. 7B*), B16F₁₀ (147.3 μM ; *Fig. 7D*), and E.G7 cells (103.8 μM ; *Fig. 7E*). However, with a more than 10-fold higher IC₅₀ value, MC38 colon carcinoma cells were found to be much more resistant to TAS-116-induced cell death (1964 μM ; *Fig. 7C*).

Remarkably, most cell lines, with the exception of MC38, displayed a plateau phase at concentrations between 0.01 μM to 0.5 μM , and the first marked effects on cell viability were observed following treatment with 1 μM TAS-116. RP157.8 SCLC cells appeared to respond differently in this regard, as the percentage of cells that suffered cell death increased noticeably by 4.79% after treatment with 0.2 μM compared to 0.1 μM . For all other cell lines except ACF135.10, the increase in this concentration range was less than 1%. However, this is difficult to assess for the latter because of the rather high standard deviation at this point of measurement (19.62% \pm 10.74%). Although the cell death inducing effect in RP157.8 cells started at lower concentrations, they still exhibited the second highest IC₅₀ value, owing to a flatter ascent of the curve at higher concentrations.

The first concentration used in the following experiments was set at 0.5 μM in synopsis of these results, on the assumption that this concentration would have stronger effects in RP157.8 cells than in the other cell lines. For comparison, cells were also treated with 10 μM TAS-116, as this concentration was found to affect cell viability but was still at least one power of ten below the IC₅₀ value of each cell line.

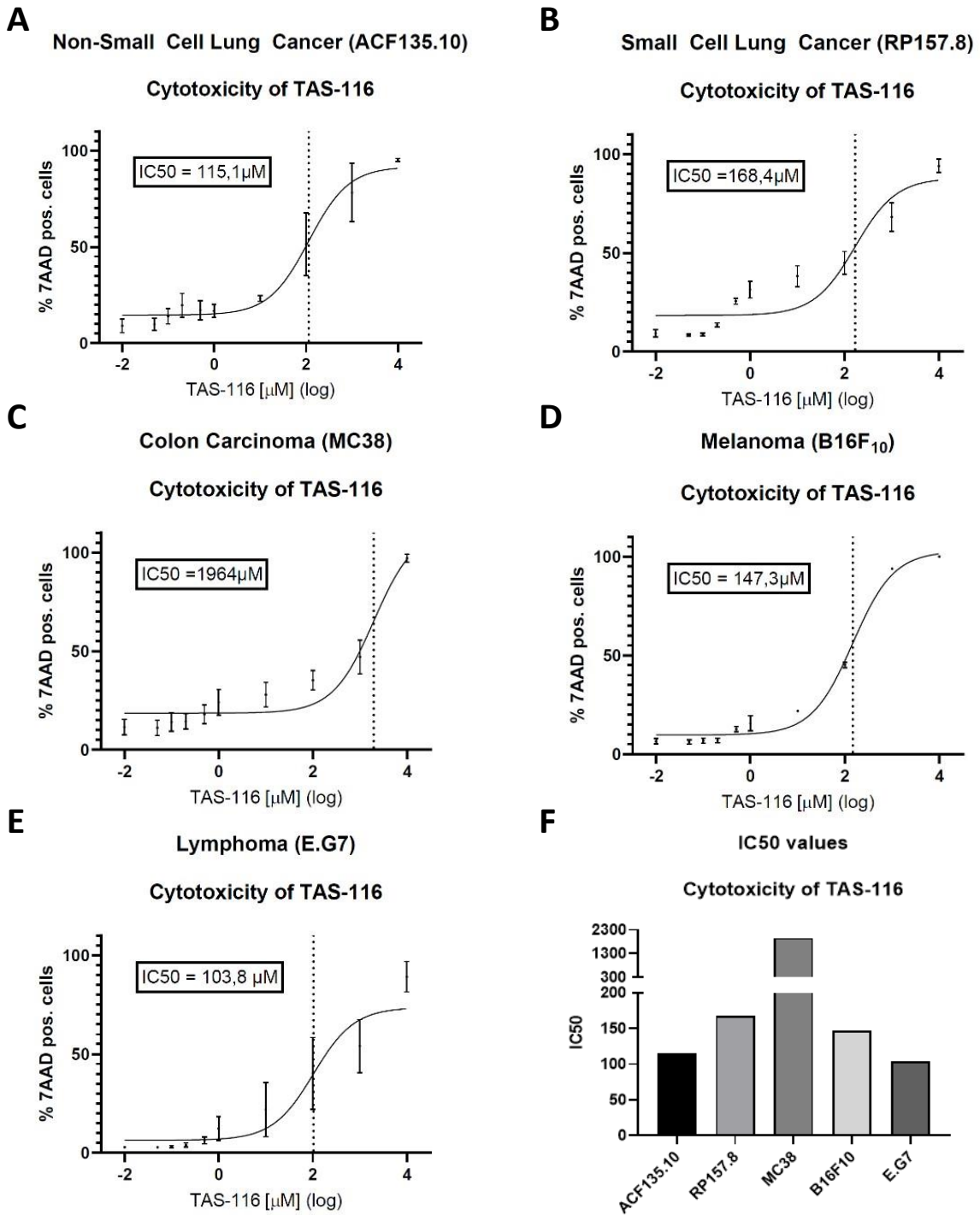


Figure 7: Cytotoxicity of TAS-116

ACF135.10 (A), RP157.8 (B), MC38 (C), B16F₁₀ (D), and E.G7 (E) cells were treated with rising concentrations of TAS-116 for 24 hours. Cells were stained with 7-AAD and the IC₅₀ was determined (F) using a non-linear regression model. Mean with SEM; n=3

5.2 Viability after TAS-116 treatment and irradiation

The aim of this study is to analyze the effects of TAS-116 administration in combination with RT on different tumor cell lines. Therefore, it is essential to investigate not only the cytotoxicity of TAS-116 itself, but foremost the toxic effects of TAS-116 and RT in combination. ACF135.10, RP157.8, MC38, and B16F₁₀ cells were thus treated with 0.5 μ M and 10 μ M TAS-116, and irradiated one hour later with doses up to 12 Gy. To assess cell death induced by this treatment, tumor cells were stained with Hoechst 33342 and PI 72 hours after RT and observed under a fluorescent microscope. Dead, i.e., PI positive cells, were subsequently counted and set into relation to the total number of cells per image.

Consistent with the previously mentioned results, MC38 cells were found to be relatively resistant to the study treatment, with no statistically significant increase in cell death under any condition (*Fig. 8C; Fig. 11*). At each irradiation dose (except 4 Gy, which is most likely due to an artifact), there was a slight trend toward increased cell death after treatment with 10 μ M TAS-116, but no visible effect was induced by 0.5 μ M TAS-116 up to 8 Gy irradiation. Unexpectedly, no consistent effects of combination of TAS-116 with RT on cell viability were detected in B16F₁₀ cells, either (*Fig. 8D; Fig. 12*).

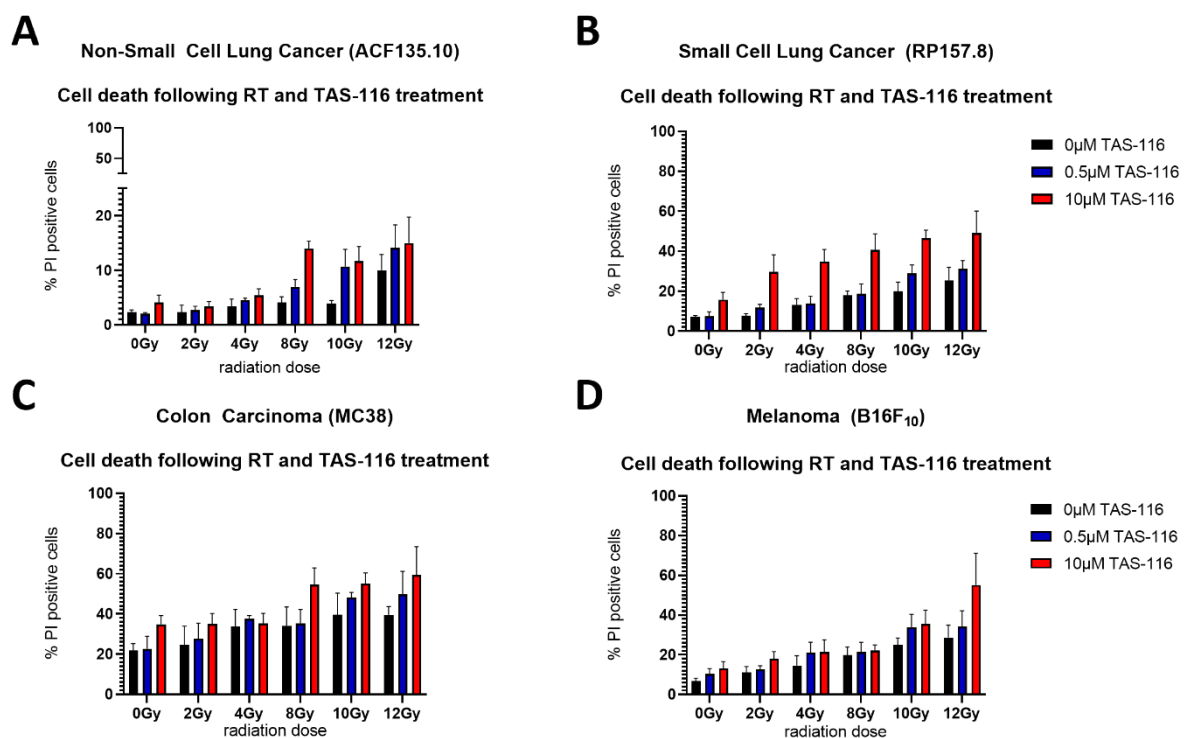


Figure 8: Cell viability following RT and TAS-116 treatment

Tumor cells were treated with 0.5 and 10 μ M TAS-116, and irradiated one hour later. Cells were stained with PI 72 hours after irradiation. PI positive cells were counted and are illustrated for ACF135.10 (A), RP157.8 (B), MC38 (C), and B16F₁₀ (D) cells. Mean with SEM; n=3

On the other hand, there was a trend toward enhanced cell death induction in both lung cancer cell lines. In ACF135.10 cells, the percentage of PI positive cells was slightly increased after HSP90 inhibition and RT with doses of at least 8 Gy compared to RT only (*Fig. 8A; Fig. 9*). Interestingly, the ability of the combined treatment with TAS-116 and RT to induce cell death, as suggested by the observed trend, apparently reached its maximum in cells that received 10 μ M TAS-116 and 8 Gy RT, as higher treatment conditions did not exceed the effect observed in this group. It should be noted, however, that the mean percentage of PI positive ACF135.10 cells did not exceed 15% in any group.

In contrast, the proportion of PI positive RP157.8 cells treated with 10 μ M TAS-116 gradually increased across all radiation doses, yet this effect was not statistically significant (*Fig. 8B; Fig. 10*). This trend, however, was not observed following treatment with 0.5 μ M, except for a slight tendency toward an increase in the 10 and 12 Gy groups, respectively.

Overall, neither RT or TAS-116 alone, nor the combined treatment resulted in a statistically significant increase of PI positive cells in any cell line. Both lung cancer cell lines, however, seemed to be somewhat more susceptible to the study treatment than MC38 and B16F₁₀ cells, with a trend toward a synergistic effect in RP157.8 cells even at very low doses of radiation. The following experiments were therefore conducted on ACF135.10, RP157.8 and MC38 cells only.

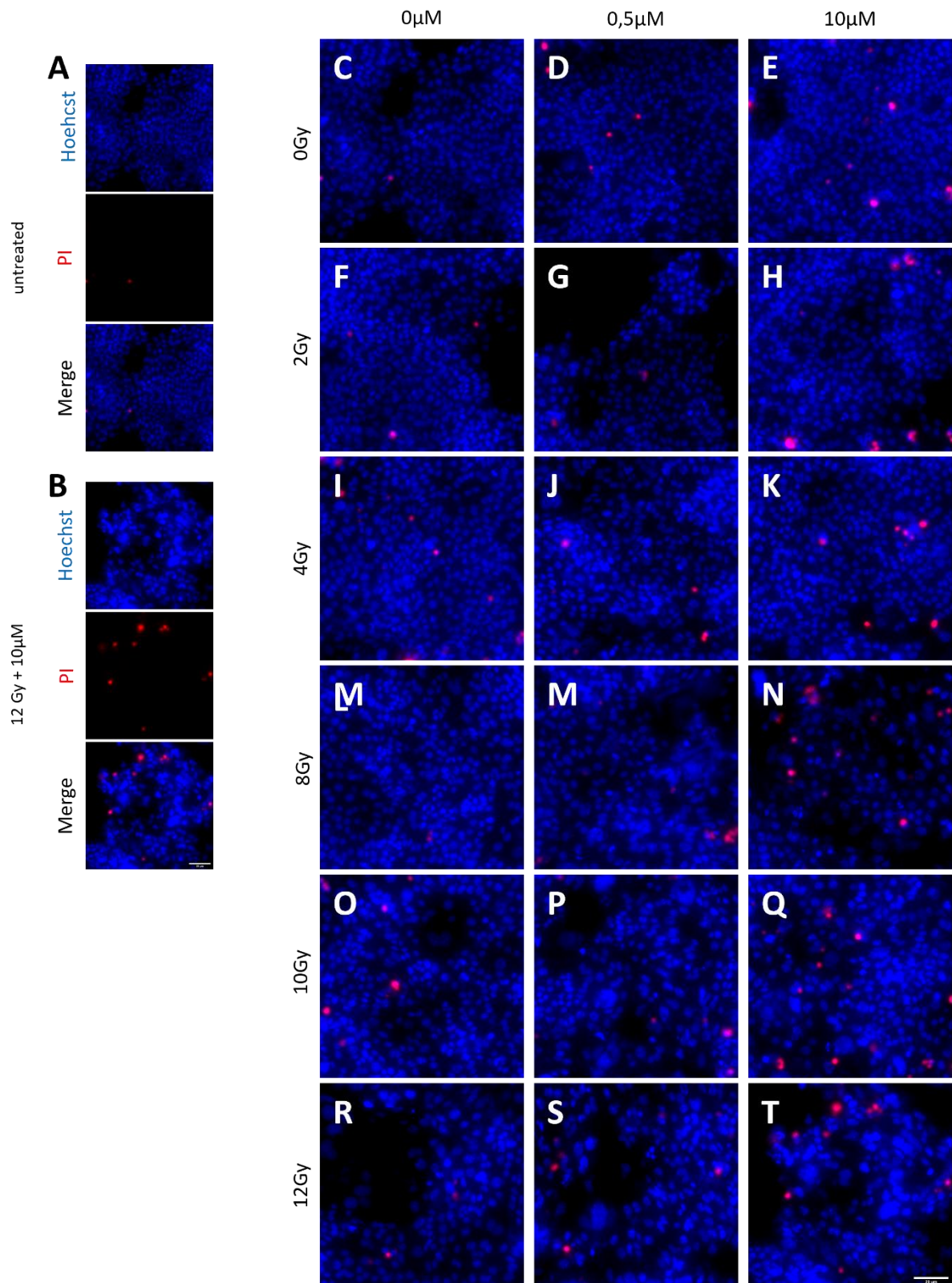


Figure 9: Propidium Iodide staining of ACF135.10 cells

ACF135.10 cells were treated with 0.5 and 10 μM TAS-116, irradiated one hour later, and stained with Hoechst (blue) and PI (red) 72 hours after irradiation. Single color images for untreated cells (A), and for cells treated with 12 Gy and 10 μM TAS-116 (B) are shown. One exemplary multicolor image is shown for every condition (C-T). Scale bar in B accounts for all images in A-B; Scale bar in T accounts for C-T. Scale bars correspond to 20 μm .

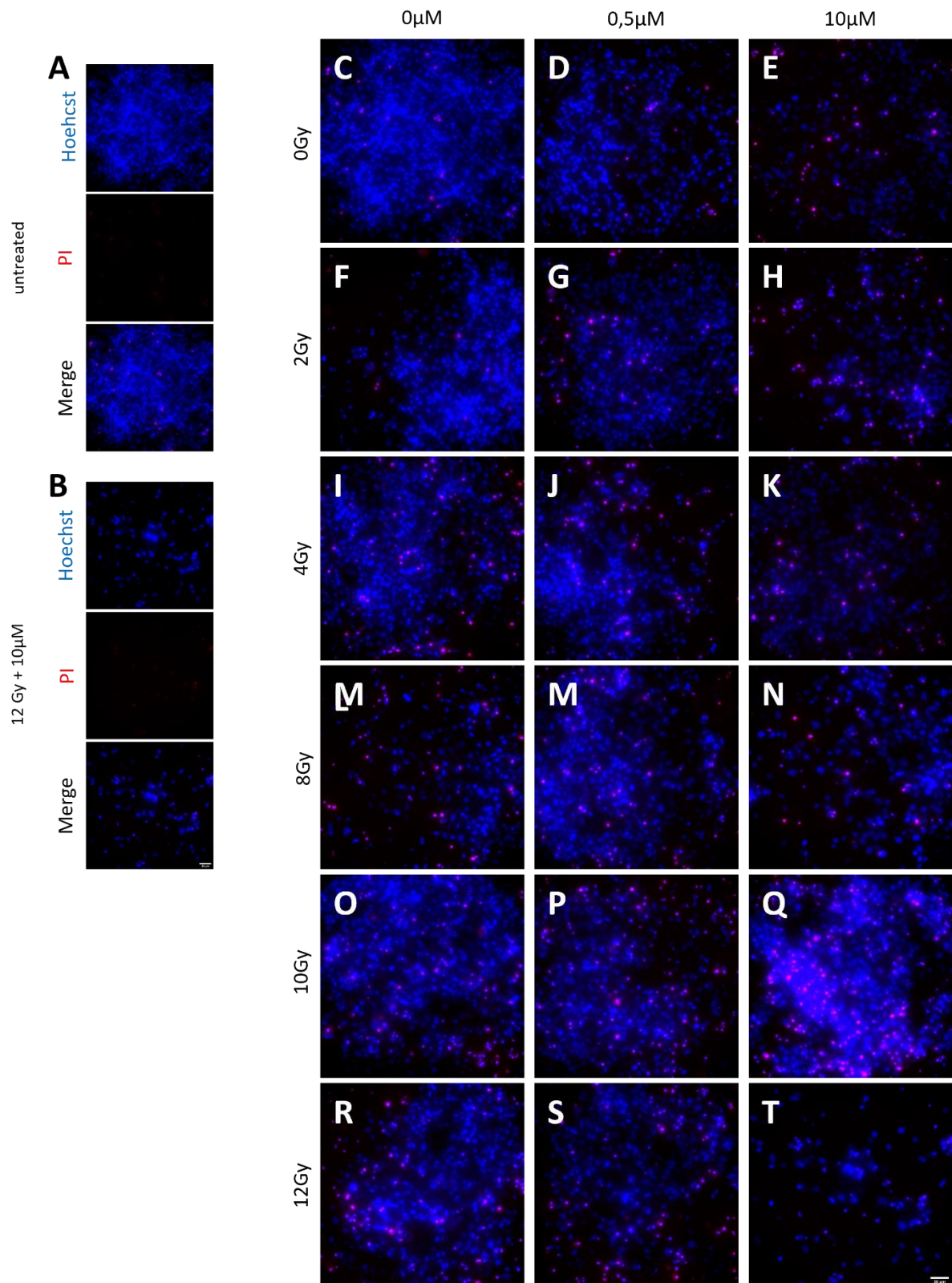


Figure 10: Propidium Iodide staining of RP157.8 cells

RP157.8 cells were treated with 0.5 and 10 μM TAS-116, irradiated one hour later, and stained with Hoechst (blue) and PI (red) 72 hours after irradiation. Single color images for untreated cells (A), and for cells treated with 12 Gy and 10 μM TAS-116 (B) are shown. One exemplary multicolor image is shown for every condition (C-T). Scale bar in B accounts for all images in A-B; Scale bar in T accounts for C-T. Scale bars correspond to 20 μm .

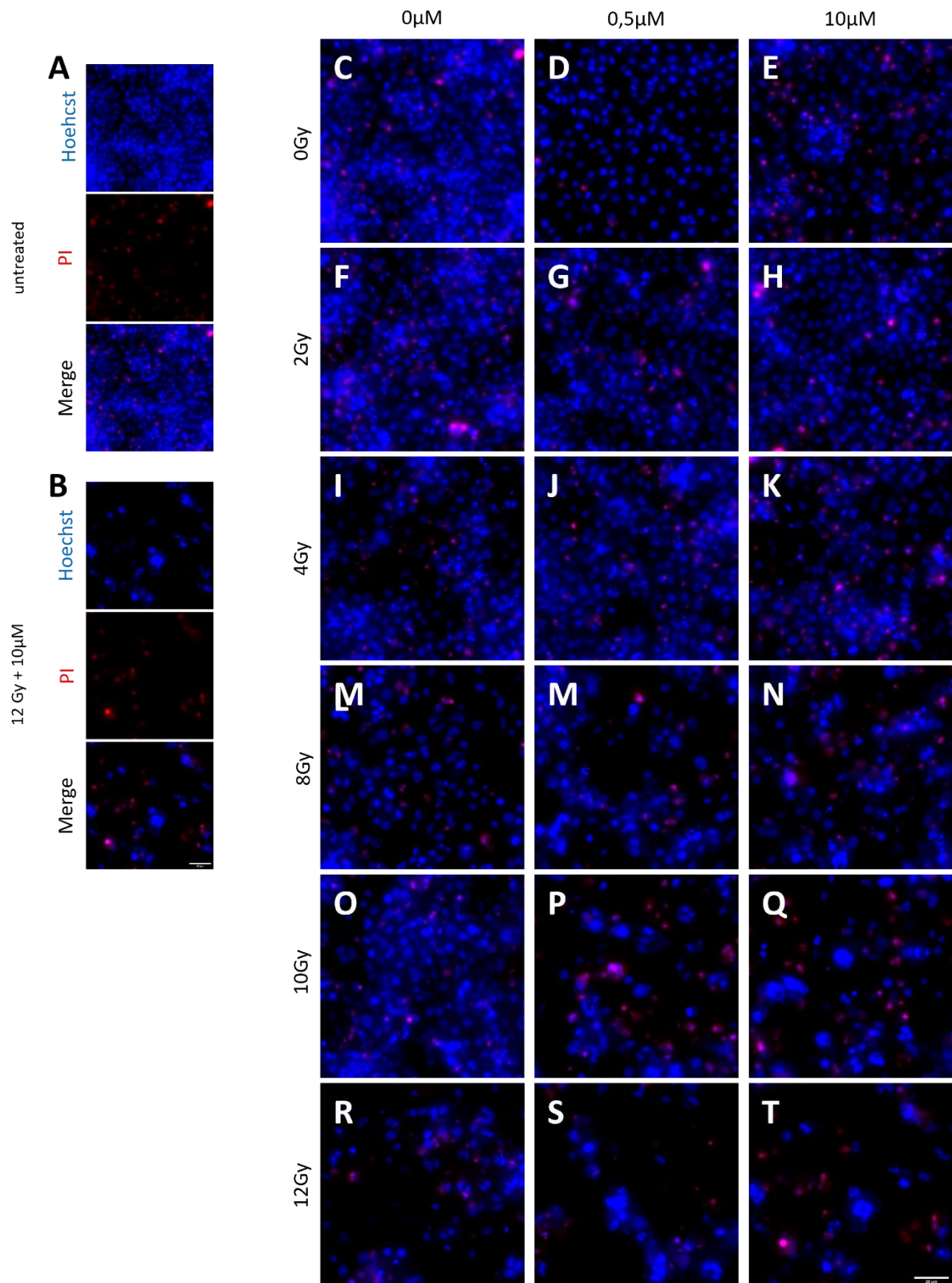


Figure 11: Propidium Iodide staining of MC38 cells

MC38 cells were treated with 0.5 and 10 μM TAS-116, irradiated one hour later, and stained with Hoechst (blue) and PI (red) 72 hours after irradiation. Single color images for untreated cells (A), and for cells treated with 12 Gy and 10 μM TAS-116 (B) are shown. One exemplary multicolor image is shown for every condition (C-T). Scale bar in B accounts for all images in A-B; Scale bar in T accounts for C-T. Scale bars correspond to 20 μm .

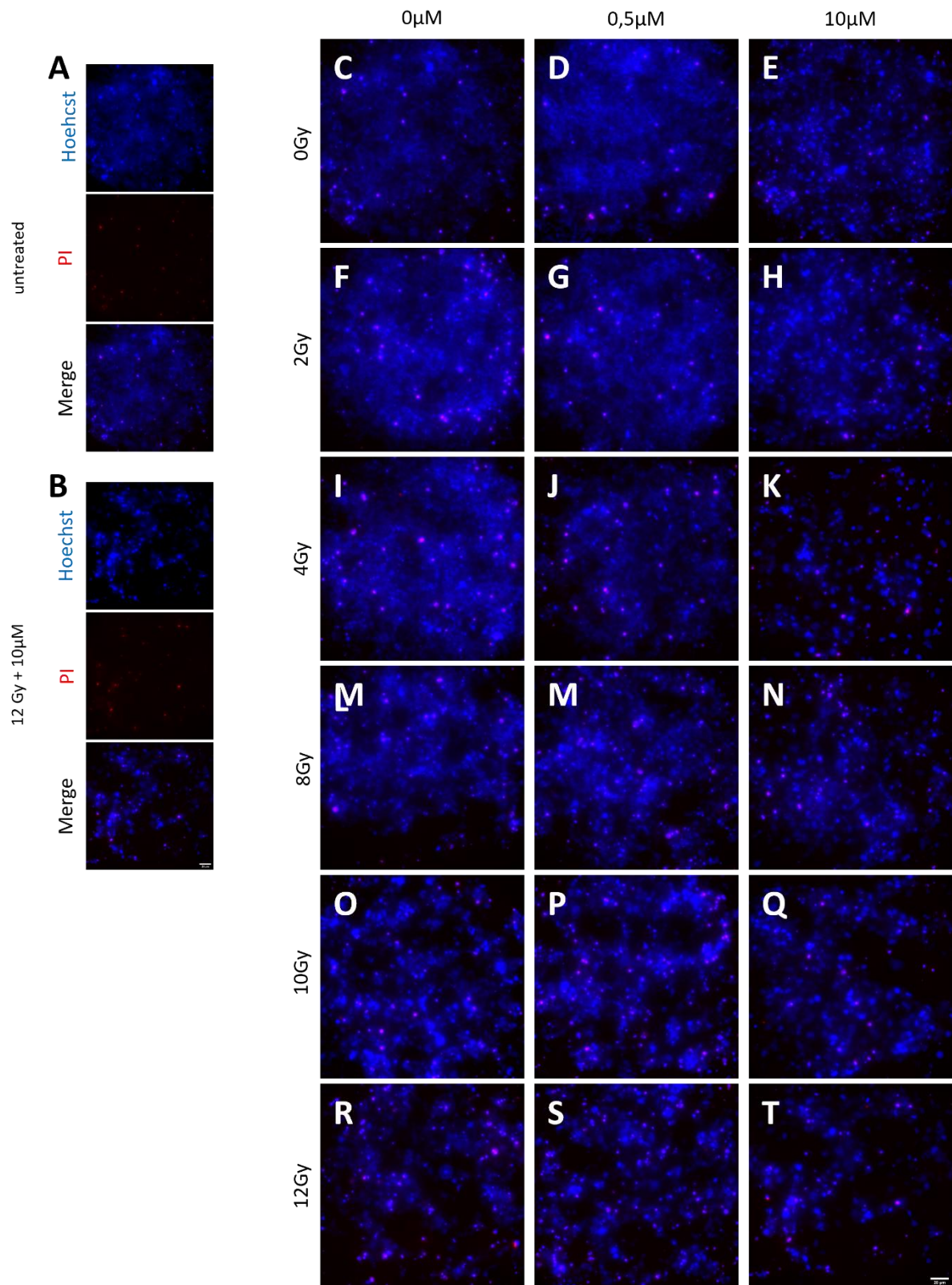


Figure 12: Propidium Iodide staining of B16F₁₀ cells

B16F₁₀ cells were treated with 0.5 and 10 μ M TAS-116, irradiated one hour later, and stained with Hoechst (blue) and PI (red) 72 hours after irradiation. Single color images for untreated cells (A), and for cells treated with 12 Gy and 10 μ M TAS-116 (B) are shown. One exemplary multicolor image is shown for every condition (C-T). Scale bar in B accounts for all images in A-B; Scale bar in T accounts for C-T. Scale bars correspond to 20 μ m.

5.3 Induction of DNA double-strand breaks

In reaction to DNA damage, as caused by RT for example, histone H2AX is phosphorylated and thus serves as a marker for DNA double-strand breaks. One hypothesis of this work is that TAS-116 impairs mechanisms for repair of radiation-induced DNA damage by inhibiting HSP90, resulting in enhanced γ H2AX signal.

Phosphorylation of histone H2AX occurs within seconds upon DNA double-strand breaks. However, staining for γ H2AX was not performed immediately after treatment with TAS-116 and RT, but three hours later to analyze the extent of residual DNA damage after repair mechanisms should normally have already started.

Since phosphorylation of histone H2AX occurs at every DNA double-strand break, the latter are normally quantified by counting the γ H2AX foci. However, the experimental setup for this thesis resulted in DNA damage on a scale that rendered counting impossible (*Fig. 14; Fig. 15; Fig. 16*). This problem was overcome by alternatively quantifying H2AX phosphorylation by measuring the integrated density of γ H2AX staining signal for each cell and normalizing to the untreated control.

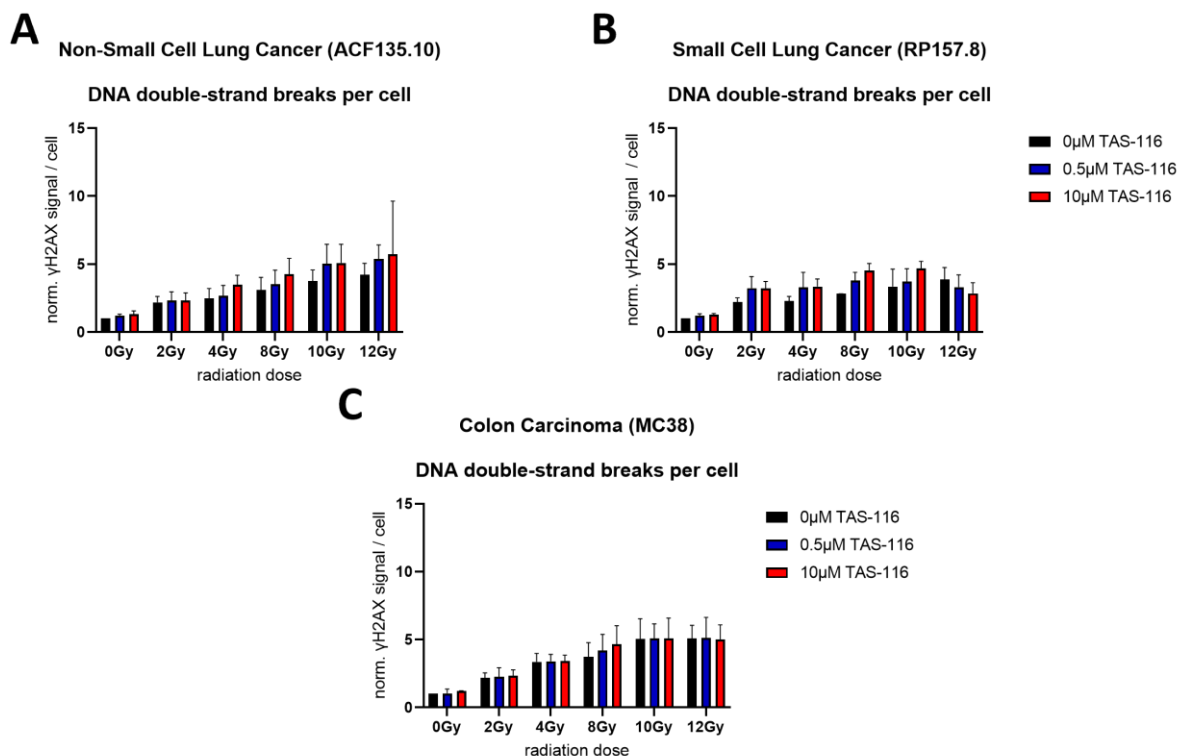


Figure 13: DNA double-strand breaks following RT and TAS-116 treatment

Tumor cells were treated with 0.5 and 10 μ M TAS-116, and irradiated one hour later. Cells were stained for γ H2Ax three hours after irradiation. Normalized γ H2Ax signal per cell is illustrated for ACF135.10 (A), RP157.8 (B), and MC38 (C) cells. Mean with SEM; $n=3$

TAS-116 did not exhibit a tendency to cause DNA double-strand breaks by itself in any cell line. In ACF135.10 cells, there was a trend toward increased H2AX phosphorylation by RT

alone in a dose-dependent manner (*Fig. 13A; Fig. 14*). The addition of 10 μM TAS-116 mildly enhanced this effect at radiation doses of 4 Gy and above, whereas the lower concentration did not result in any visible augmentation up to an irradiation of 10 Gy.

Irradiation alone likewise exhibited a tendency to increase γH2AX staining in RP157.8 cells (*Fig. 13B; Fig. 15*). Consistent with the cytotoxicity results, a trend toward an increase in γH2AX foci was observed in RP157.8 cells after TAS-116 administration at both concentrations, even at the lowest radiation dose. While no difference was observed between the different concentrations of the drug in cells irradiated with 2 and 4 Gy, the 10 μM group outperformed the 0.5 μM group in terms of induction of DNA damage after RT with 8 and 10 Gy, respectively, yet this was not statistically significant. Unexpectedly, this trend reversed in the 12 Gy group, and γH2AX foci seemingly decreased after treatment with TAS-116 compared to cells that received RT only.

Irradiation also showed the tendency to slightly increase induction of γH2AX foci in MC38 colon carcinoma cells in a dose-dependent manner up to 10 Gy (*Fig. 13C; Fig. 16*). The addition of TAS-116 demonstrated a tendency to enhance this effect only in cells irradiated with 8 Gy. Summing up, there was only a moderate trend toward RT- and TAS-116-mediated enhanced induction of γH2AX foci for every cell line, and the results did not reach statistical significance.

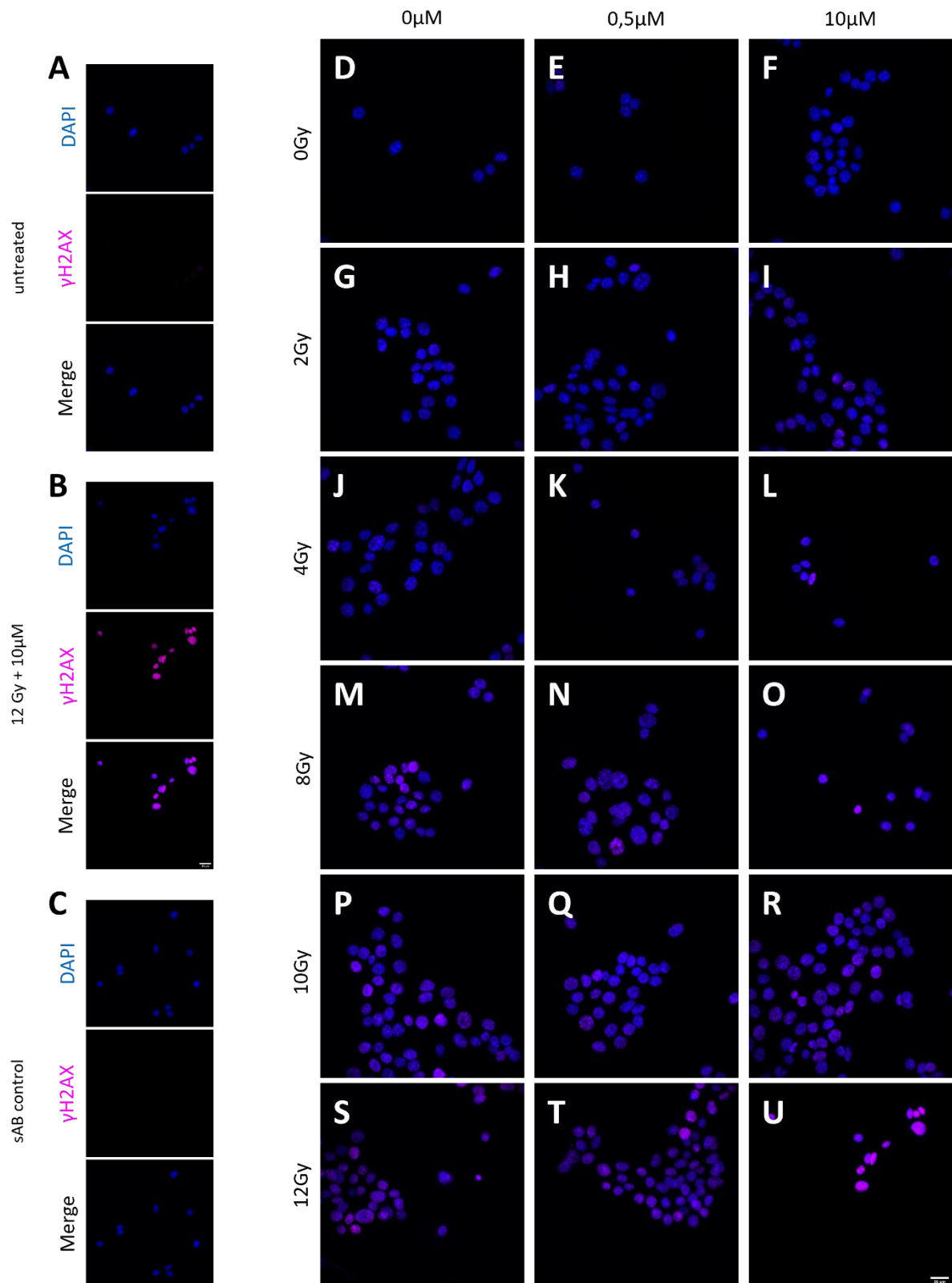


Figure 14: Immunofluorescence staining for γ H2AX on ACF135.10 cells

ACF135.10 cells were treated with 0.5 and 10 μ M TAS-116, irradiated one hour later, and stained with DAPI (blue) and anti- γ H2AX with Alexa Fluor 647 (magenta) three hours after irradiation. Single color images for untreated cells (A), cells treated with 12 Gy and 10 μ M TAS-116 (B), and for untreated cells stained without the secondary antibody (C) are shown. One exemplary multicolor picture is shown for every condition (D-U). Scale bar in B accounts for all images in A-C; Scale bar in U accounts for D-U. Scale bars correspond to 20 μ m.

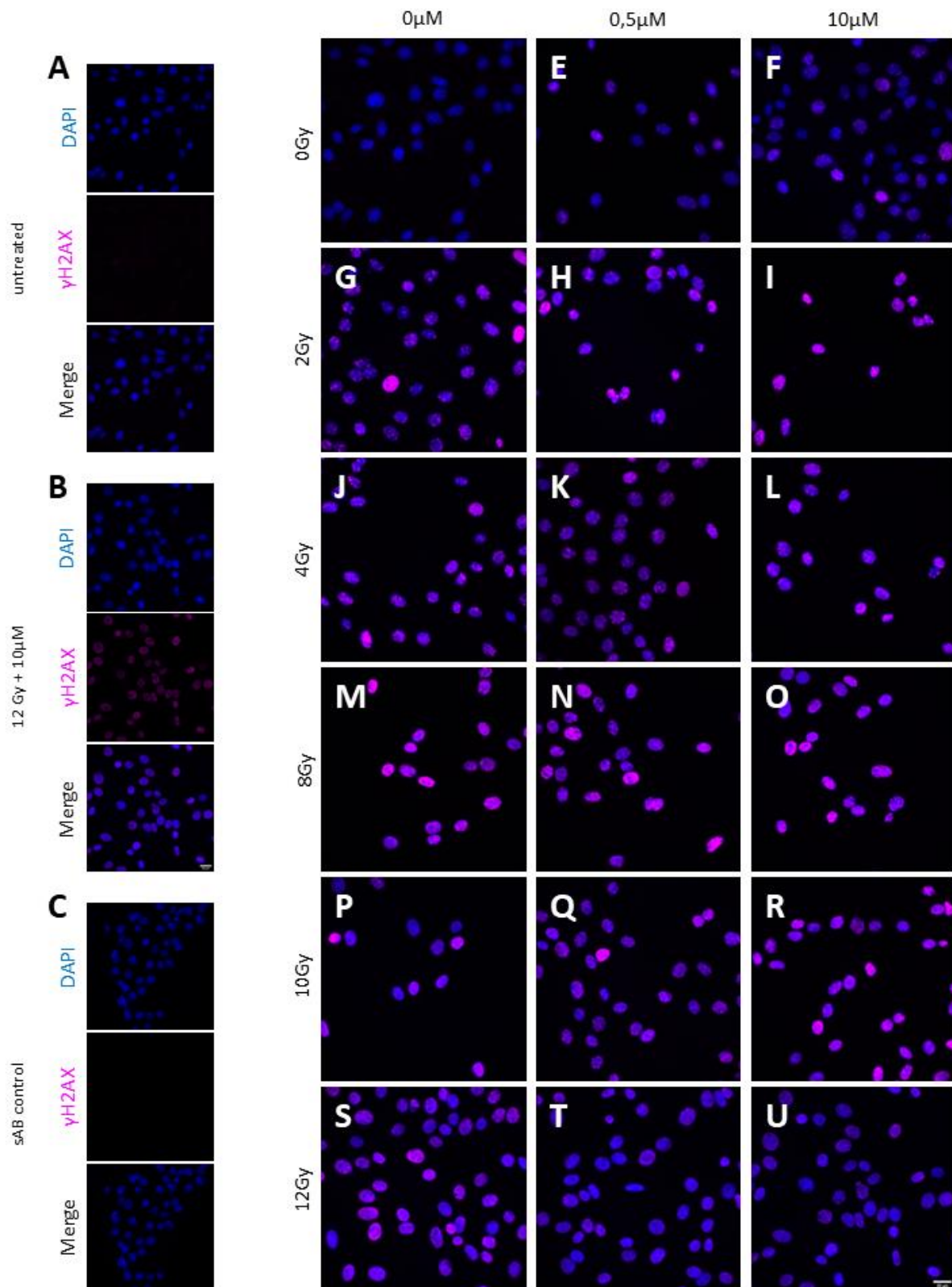


Figure 15: Immunofluorescence staining for γ H2AX on RP157.8 cells

RP157.8 cells were treated with 0.5 and 10 μ M TAS-116, irradiated one hour later, and stained with DAPI (blue) and anti- γ H2AX with Alexa Fluor 647 (magenta) three hours after irradiation. Single color images for untreated cells (A), cells treated with 12 Gy and 10 μ M TAS-116 (B), and for untreated cells stained without the secondary antibody (C) are shown. One exemplary multicolor picture is shown for every condition (D-U). Scale bar in B accounts for all images in A-C; Scale bar in U accounts for D-U. Scale bars correspond to 20 μ m.

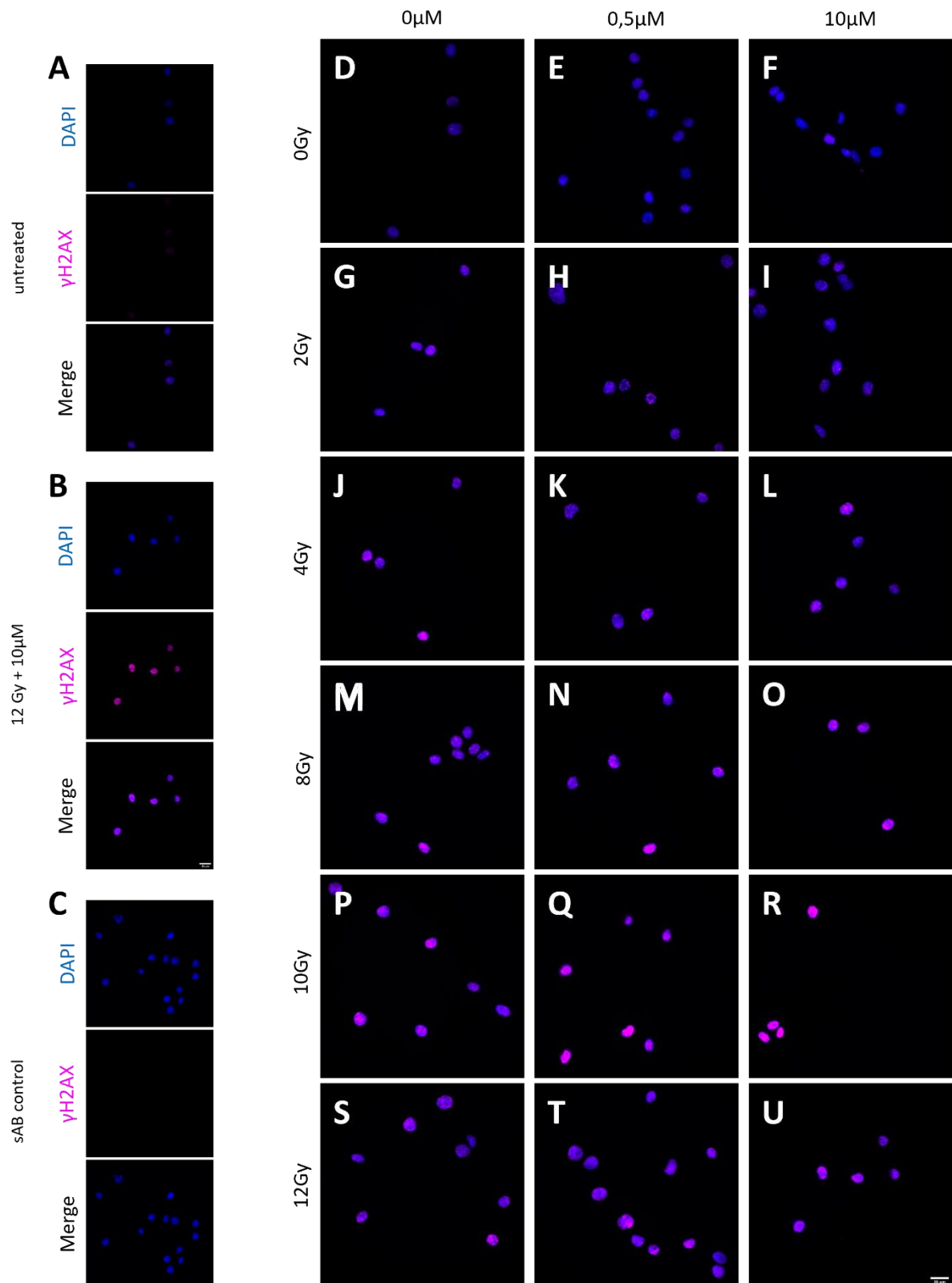


Figure 16: Immunofluorescence staining for γ H2AX on MC38 cells

MC38 cells were treated with 0.5 and 10 μ M TAS-116, irradiated one hour later, and stained with DAPI (blue) and anti- γ H2AX with Alexa Fluor 647 (magenta) three hours after irradiation. Single color images for untreated cells (A), cells treated with 12 Gy and 10 μ M TAS-116 (B), and for untreated cells stained without the secondary antibody (C) are shown. One exemplary multicolor picture is shown for every condition (D-U). Scale bar in B accounts for all images in A-C; Scale bar in U accounts for D-U. Scale bars correspond to 20 μ m.

5.4 Analysis of cGAS/STING pathway activation

As previously explained, activation of the cGAS/STING pathway is induced via sensing of dsDNA in the cytosol by cGAS which eventually leads to phosphorylation of STING protein. Cytosolic dsDNA and pSTING can therefore serve as markers to assess cGAS/STING pathway activation. In this thesis, however, cGAS/STING pathway activation was induced via inhibition of HSP90. TBK1, a kinase whose function is indispensable for complete pathway activation, is one of many HSP90 client proteins. Inhibition of HSP90 could thus also result in incomplete activation of the cGAS/STING pathway which would not be detected via quantification of pSTING alone. Secretion of IFN β was therefore included as another marker to assess not only pathway activation but also achievement of its final effects.

To ensure the experimental setup to assess cGAS/STING pathway activation was correct, immunofluorescence staining for dsDNA, pSTING, and IFN β was performed on RP157.8 SCLC cells at various time points following preincubation with either 0.5 or 10 μ M TAS-116 one hour prior to RT with 8 Gy.

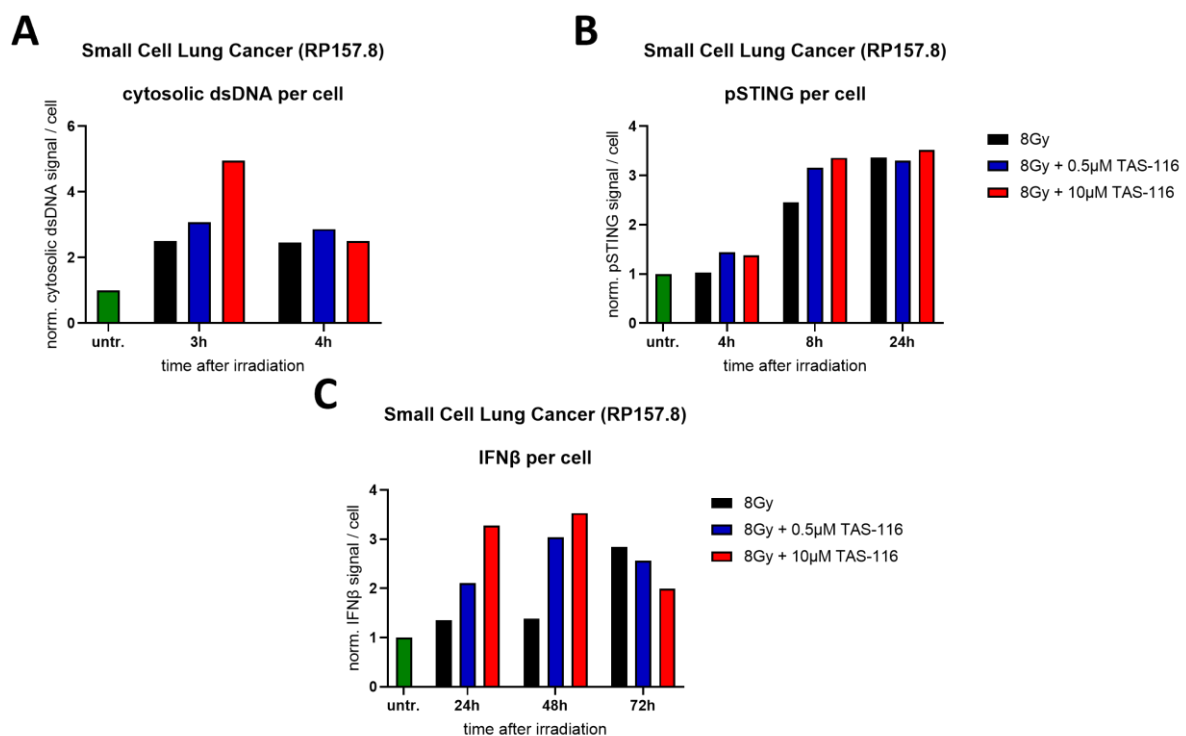


Figure 17: cGAS/STING pathway activation by RT and TAS-116

RP157.8 cells were treated with 0.5 and 10 μ M TAS-116, and irradiated one hour later. Cells were stained for dsDNA (A), pSTING (B), and IFN β (C) at various time points after irradiation. Normalized immunofluorescence signal is illustrated for every staining. $n=1$

As dsDNA in the cytosol is known to occur directly following irradiation-induced DNA damage, which was quantified three hours after RT in this study, staining of dsDNA was performed three and four hours after irradiation with 8 Gy with or without TAS-116 preincubation (Fig. 17A).

Immunofluorescence signal for dsDNA in the cytosol was analyzed for individual cells and normalized to an untreated control. Irradiation alone resulted in a 2.5-fold increase of cytosolic dsDNA signal within three hours and this effect prevailed until four hours after treatment. Whereas TAS-116 further enhanced this effect in a concentration-dependent manner in cells fixed for staining three hours after RT, no such increase could be observed anymore one hour later.

To find the time point best suited to assess upregulation of STING phosphorylation, RP157.8 cells were first irradiated with 8 Gy without TAS-116 preincubation and immunofluorescence staining for pSTING was performed at various time points ranging from three to 48 hours after RT. There was an incremental upregulation of STING phosphorylation between four and 24 hours, but this effect seemed to cease within 48 hours of RT (data not shown). The same staining was therefore repeated four, eight, and 24 hours after irradiation with 8 Gy and preceding administration of TAS-116 (*Fig. 17B*). While pSTING signal per cell increased up to 24 hours in line with the previous experiment, enhancement of this effect by TAS-116 was observed only in cells that were fixed for staining eight hours after treatment.

Because secretion of IFN β results from cGAS/STING pathway activation only after the pathway has run down completely, I hypothesized that this effect could be best assessed within several days following study treatment. SCLC cells were therefore fixed 24, 48, and 72 hours after treatment as described above and stained for IFN β (*Fig. 17C*). Interestingly, RT alone did not increase IFN β secretion further than 1.3-fold in cells fixed both 24 and 48 hours after irradiation compared to the untreated control. At 72 hours following irradiation with 8 Gy, on the other hand, IFN β signal per cell was enhanced 2.8-fold. In contrast to the earlier time points, IFN β signal quantified 72 hours after RT was not further amplified by TAS-116 administration but even seemed to decrease. A concentration-dependent enhancement of IFN β secretion caused by HSP90 inhibition was most distinct in cells stained 48 hours after irradiation.

In synopsis of these results, tumor cells were hereafter fixed three hours after RT for dsDNA, eight hours for pSTING, and 48 hours for IFN β staining, respectively.

5.4.1. Cytosolic double-stranded DNA

The presence of dsDNA in the cytosol is essential for the activation of the cGAS/STING pathway and occurs as a consequence of DNA damage in the nucleus.

Consistent with the aforementioned results regarding the induction of DNA double-strand breaks by RT alone, there was a similar trend toward a dose-dependent increase of dsDNA in the cytosol throughout all radiation doses in ACF135.10 NSCLC and RP157.8 SCLC cells (*Fig. 18A, B*). In MC38 colon carcinoma cells, however, cytosolic dsDNA signal only seemingly intensified up to 4 Gy RT and stayed at a plateau thereafter (*Fig. 18C*).

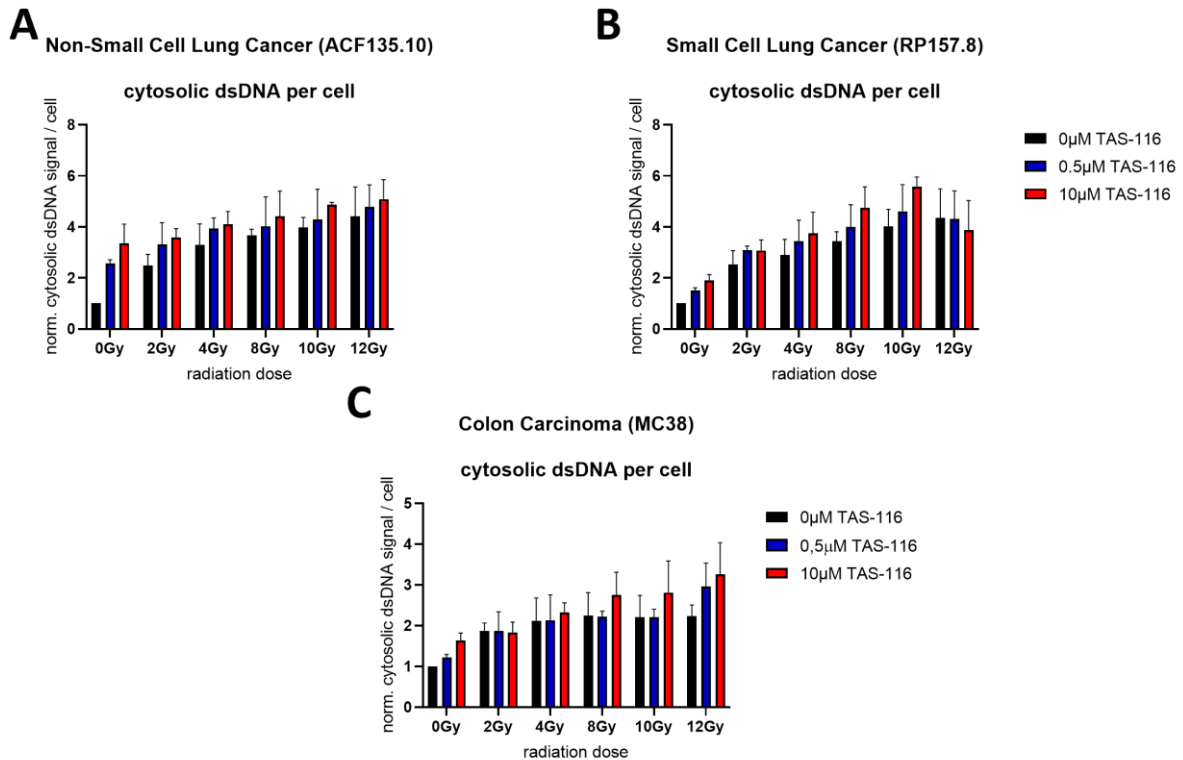


Figure 18: dsDNA in the cytosol following RT and TAS-116 treatment

Tumor cells were treated with 0.5 and 10 μM TAS-116, and irradiated one hour later. Cells were stained for dsDNA three hours after irradiation. Normalized cytosolic dsDNA signal per cell is illustrated for ACF135.10 (A), RP157.8 (B), and MC38 (C) cells. Mean with SEM; $n=3$

In every cell line, there was a tendency toward increased dsDNA staining signal mediated by treatment with TAS-116 alone in a concentration-dependent manner. Moreover, the lung cancer cell lines ACF135.10 and RP157.8 displayed a steady trend toward enhanced occurrence of dsDNA following both 0.5 and 10 μM TAS-116 treatment prior to RT, with greater effects gained by the higher concentration (Fig. 18A, B; Fig. 19; Fig. 20). However, integrated density for cytosolic dsDNA signal seemed to decrease in RP157.8 cells following 12 Gy RT in the same manner as was already observed for γH2AX staining.

In MC38 cells, the addition of 10 μM TAS-116 did not further increase the RT-mediated response at radiation doses lower than 8 Gy (Fig. 18C; Fig. 21). Effects following pretreatment with 0.5 μM TAS-116 were only observed in the 12 Gy group. However, these effects did not prove to be statistically significant.

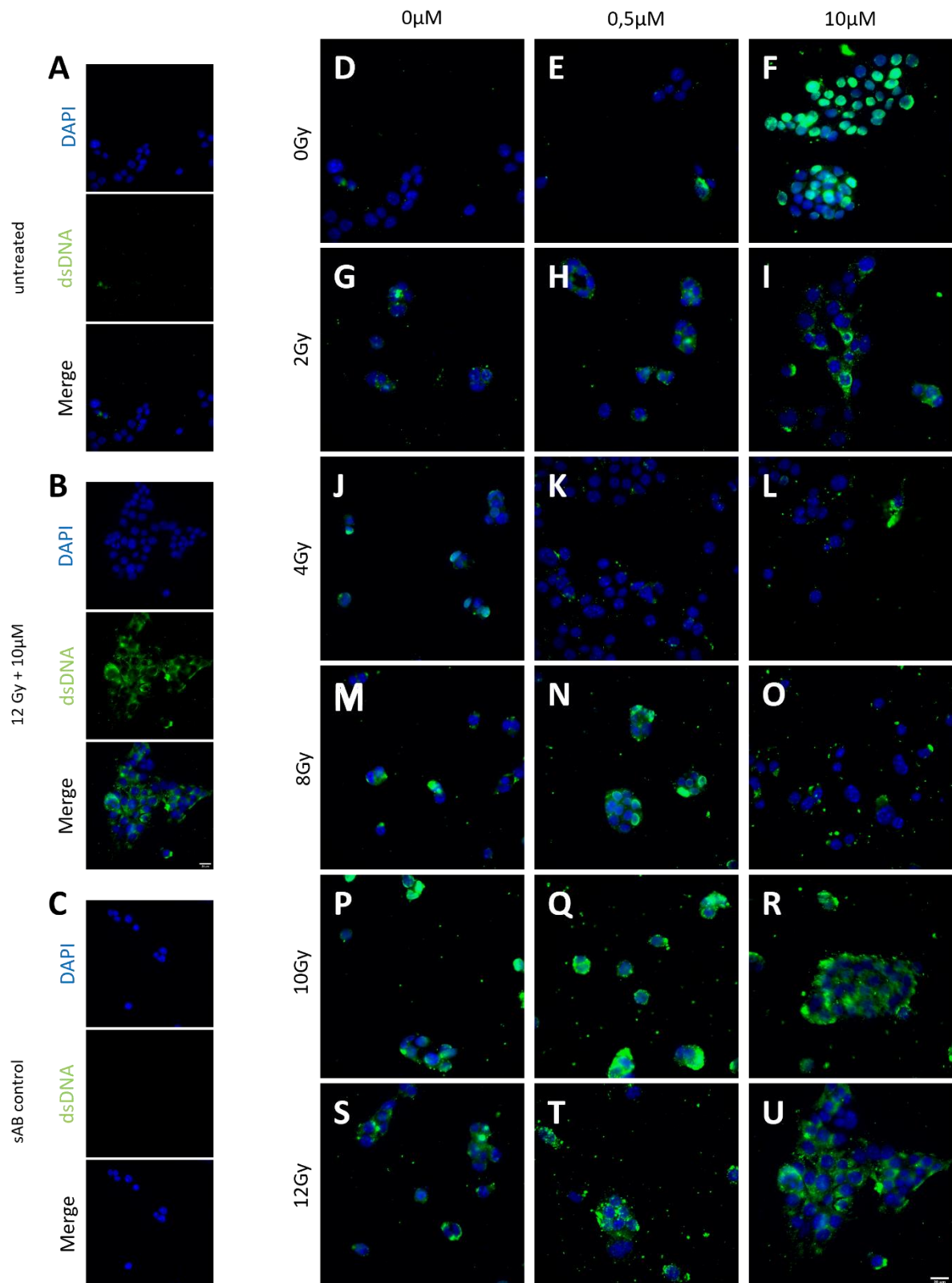


Figure 19: Immunofluorescence staining for dsDNA on ACF135.10 cells

ACF135.10 cells were treated with 0.5 and 10 μM TAS-116, irradiated one hour later, and stained with DAPI (blue) and anti-dsDNA with Alexa Fluor 488 (green) three hours after irradiation. Single color images for untreated cells (A), cells treated with 12 Gy and 10 μM TAS-116 (B), and for untreated cells stained without the secondary antibody (C) are shown. One exemplary multicolor picture is shown for every condition (D-U). Scale bar in B accounts for all images in A-C; Scale bar in U accounts for D-U. Scale bars correspond to 20 μm .

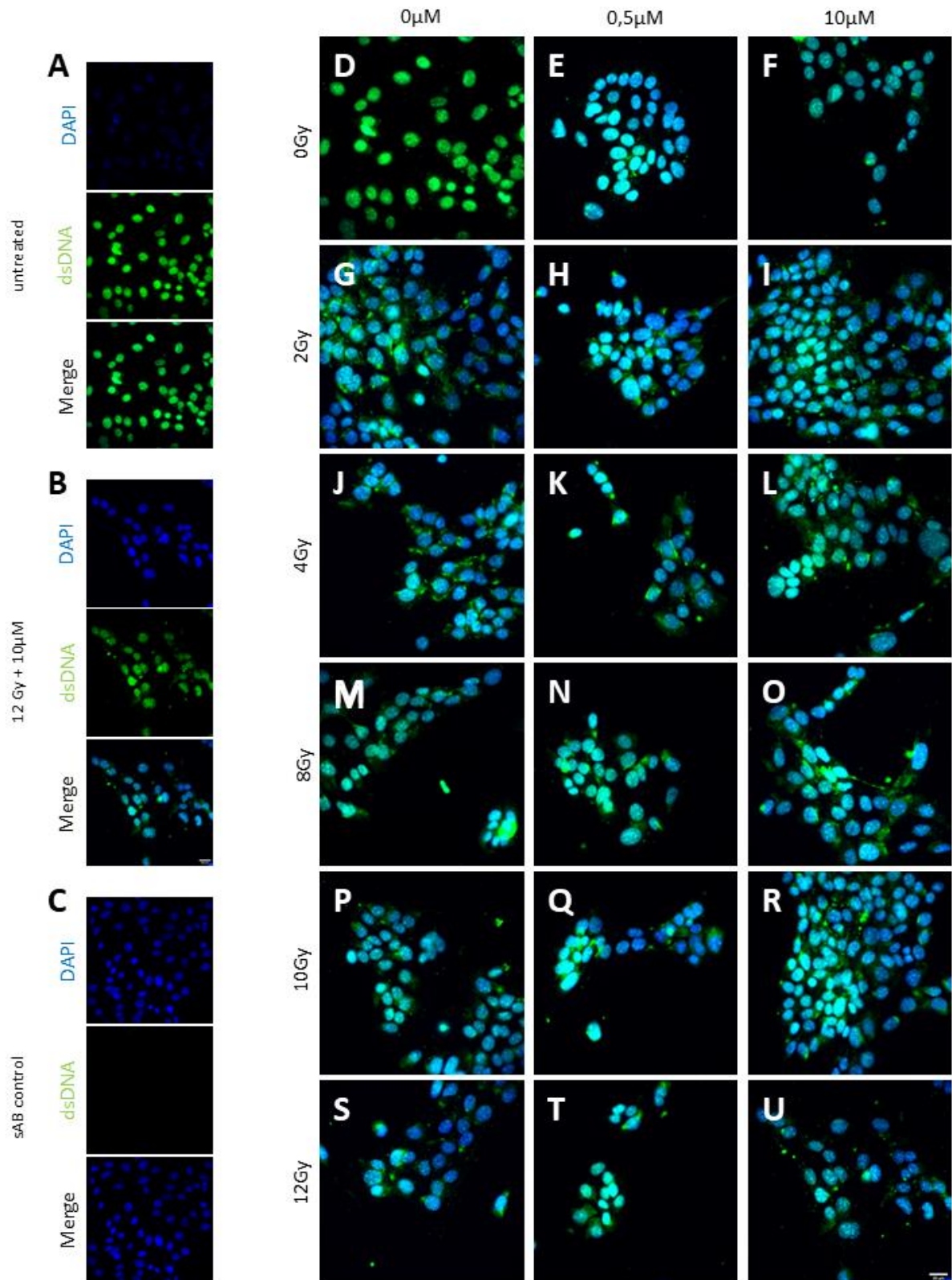


Figure 20: Immunofluorescence staining for dsDNA on RP157.8 cells

RP157.8 cells were treated with 0.5 and 10 μM TAS-116, irradiated one hour later, and stained with DAPI (blue) and anti-dsDNA with Alexa Fluor 488 (green) three hours after irradiation. Single color images for untreated cells (A), cells treated with 12 Gy and 10 μM TAS-116 (B), and for untreated cells stained without the secondary antibody (C) are shown. One exemplary multicolor picture is shown for every condition (D-U). Scale bar in B accounts for all images in A-C; Scale bar in U accounts for D-U. Scale bars correspond to 20 μm .

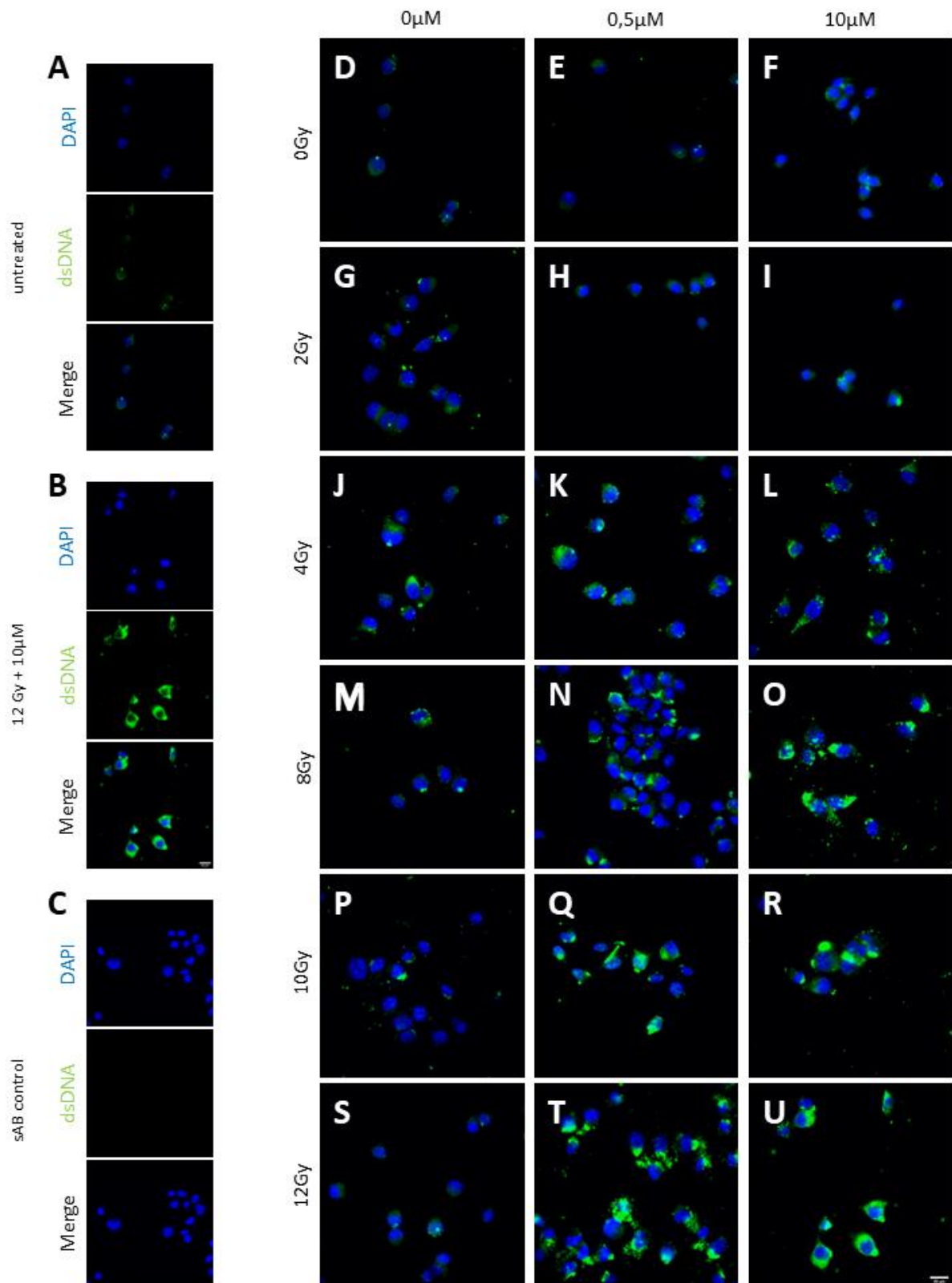


Figure 21: Immunofluorescence staining for dsDNA on MC38 cells

MC38 cells were treated with 0.5 and 10 μM TAS-116, irradiated one hour later, and stained with DAPI (blue) and anti-dsDNA with Alexa Fluor 488 (green) three hours after irradiation. Single color images for untreated cells (A), cells treated with 12 Gy and 10 μM TAS-116 (B), and for untreated cells stained without the secondary antibody (C) are shown. One exemplary multicolor picture is shown for every condition (D-U). Scale bar in B accounts for all images in A-C; Scale bar in U accounts for D-U. Scale bars correspond to 20 μm .

5.4.2. STING phosphorylation

Next, activation of the cGAS/STING pathway was analyzed by measuring pSTING eight hours after RT with or without TAS-116 preincubation one hour prior (Fig. 22).

TAS-116 treatment without subsequent irradiation resulted in a trend toward augmented STING phosphorylation in all cell lines. With a 3.5-fold increase in cells treated with 10 μ M TAS-116 compared to untreated cells, this effect was most pronounced in MC38 cells (Fig. 22C; Fig. 25).

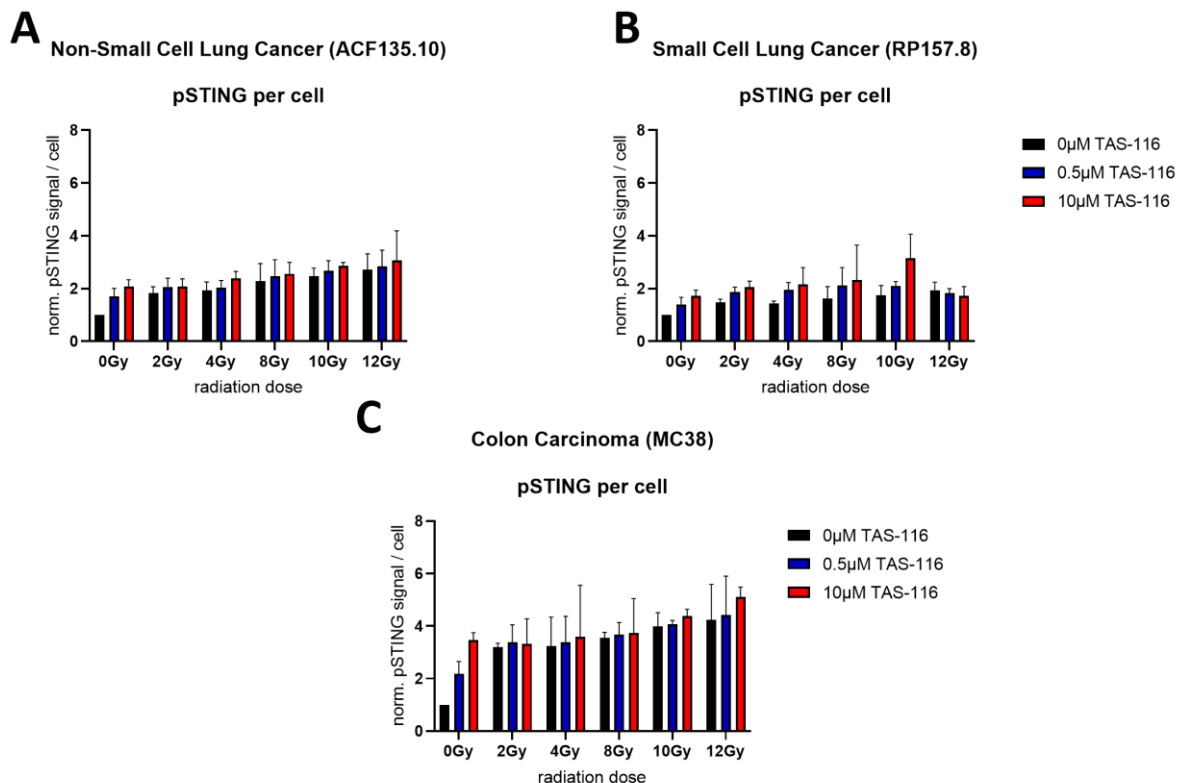


Figure 22: STING phosphorylation following RT and TAS-116 treatment

Tumor cells were treated with 0.5 and 10 μ M TAS-116, and irradiated one hour later. Cells were stained for pSTING eight hours after irradiation. Normalized pSTING signal per cell is illustrated for ACF135.10 (A), RP157.8 (B), and MC38 (C) cells. Mean with SEM; $n=3$

Increment of STING phosphorylation following 2 Gy RT in the absence of TAS-116 was most distinct in MC38 cells as well, being 3.2-fold higher than in the untreated control. Neither increasing the radiation dose nor addition of TAS-116, however, resulted in a notable further enhancement of pSTING signal in colon carcinoma cells.

ACF135.10 cells behaved similarly, with a 1.8-fold increase following 2 Gy irradiation and a slight dose-dependent ascent with higher radiation doses (Fig. 22A; Fig. 23). However, combination with HSP90 inhibition hardly seemed to enhance STING phosphorylation.

A distinct trend toward synergism of TAS-116 treatment and RT to increase pSTING signal was only observed in RP157.8 cells (Fig. 22B; Fig. 24). Whereas RT alone was not able to

increase STING phosphorylation in the SCLC cell line, there was a visible effect following preincubation with TAS-116 for every radiation dose. With a 1.8-fold increase from cells that received RT alone to cells preincubated with 10 μ M TAS-116, this tendency was most prominent in the 10 Gy group. Regardless of the applied TAS-116 concentration, pSTING signal in RP157.8 cells decreased following 12 Gy RT to approximately the level of cells that had received 10 Gy RT only. Once more, none of the effects observed for this staining were statistically significant in any cell line.

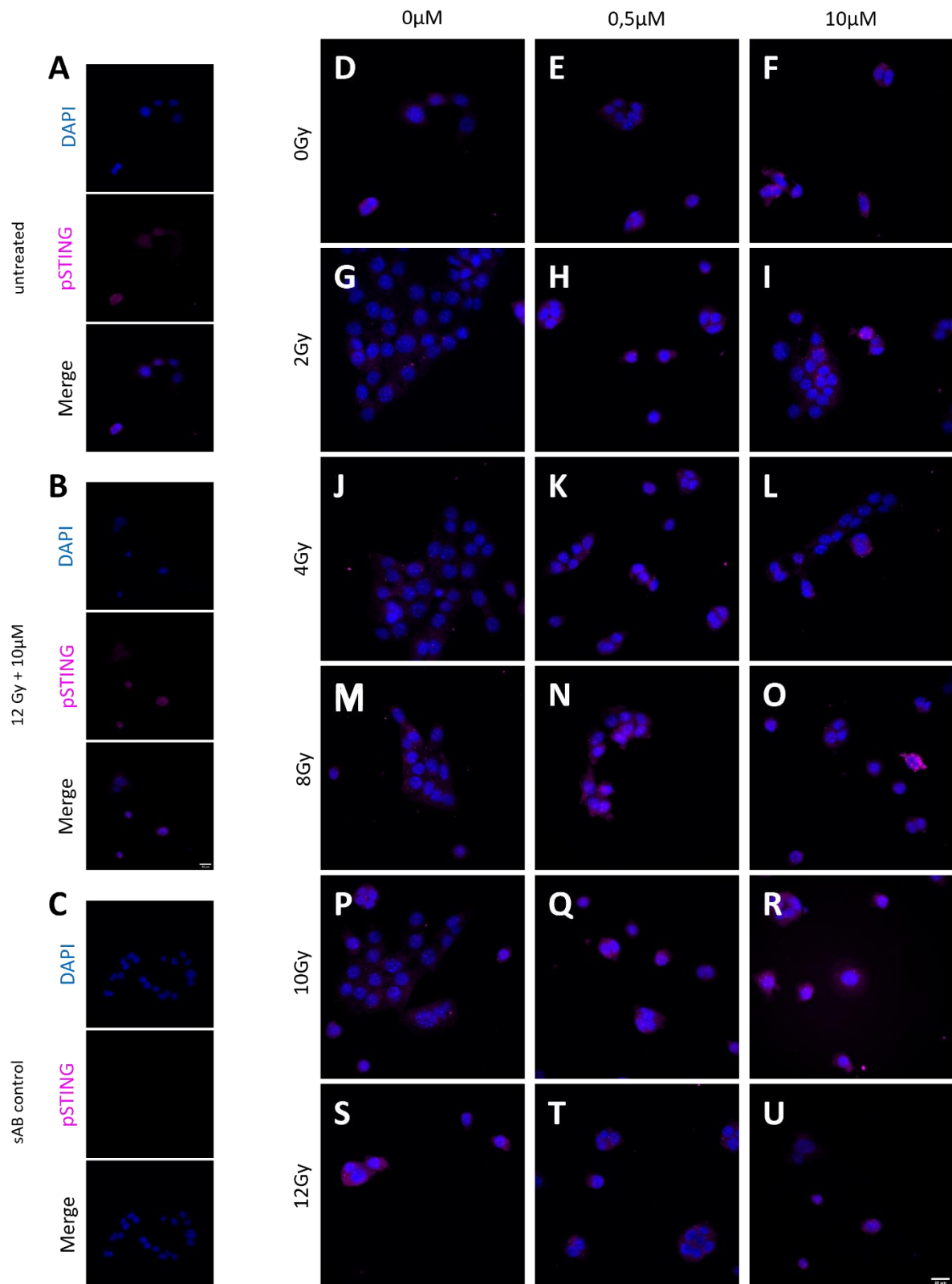


Figure 23: Immunofluorescence staining for pSTING on ACF135.10 cells

ACF135.10 cells were treated with 0.5 and 10 μM TAS-116, irradiated one hour later, and stained with DAPI (blue) and anti-pSTING with Alexa Fluor 647 (magenta) eight hours after irradiation. Single color images for untreated cells (A), cells treated with 12 Gy and 10 μM TAS-116 (B), and for untreated cells stained without the secondary antibody (C) are shown. One exemplary multicolor picture is shown for every condition (D-U). Scale bar in B accounts for all images in A-C; Scale bar in U accounts for D-U. Scale bars correspond to 20 μm .

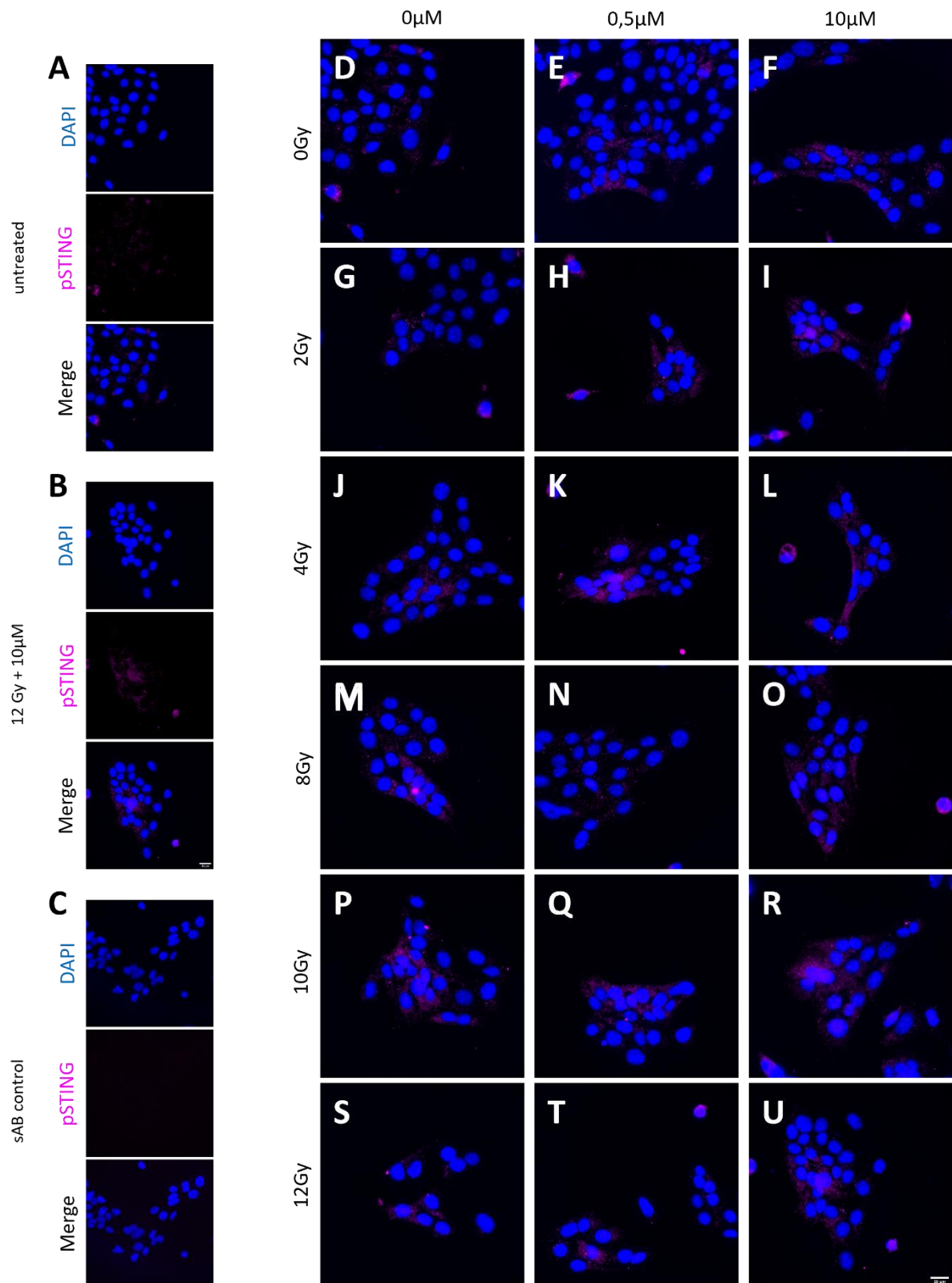


Figure 24: Immunofluorescence staining for pSTING on RP157.8 cells

RP157.8 cells were treated with 0.5 and 10 μM TAS-116, irradiated one hour later, and stained with DAPI (blue) and anti-pSTING with Alexa Fluor 647 (magenta) eight hours after irradiation. Single color images for untreated cells (A), cells treated with 12 Gy and 10 μM TAS-116 (B), and for untreated cells stained without the secondary antibody (C) are shown. One exemplary multicolor picture is shown for every condition (D-U). Scale bar in B accounts for all images in A-C; Scale bar in U accounts for D-U. Scale bars correspond to 20 μm .

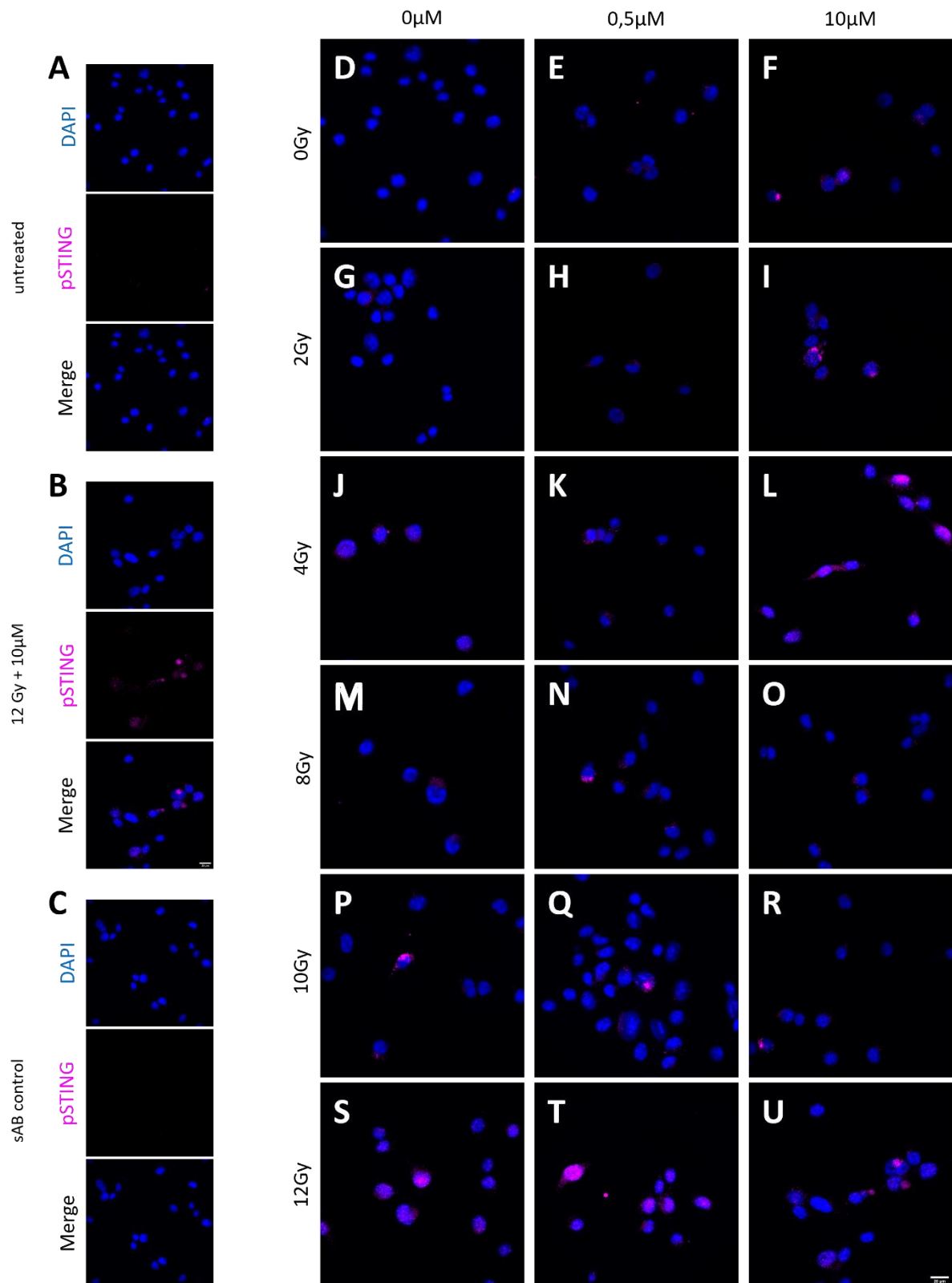


Figure 25: Immunofluorescence staining for pSTING on MC38 cells

MC38 cells were treated with 0.5 and 10 μM TAS-116, irradiated one hour later, and stained with DAPI (blue) and anti-pSTING with Alexa Fluor 647 (magenta) eight hours after irradiation. Single color images for untreated cells (A), cells treated with 12 Gy and 10 μM TAS-116 (B), and for untreated cells stained without the secondary antibody (C) are shown. One exemplary multicolor picture is shown for every condition (D-U). Scale bar in B accounts for all images in A-C; Scale bar in U accounts for D-U. Scale bars correspond to 20 μm .

5.4.3. IFN β secretion

To assess whether induction of the cGAS/STING pathway by RT and HSP90 inhibition would indeed result in completion of the whole pathway, secretion of IFN β was measured 48 hours after treatment as described above (Fig. 26).

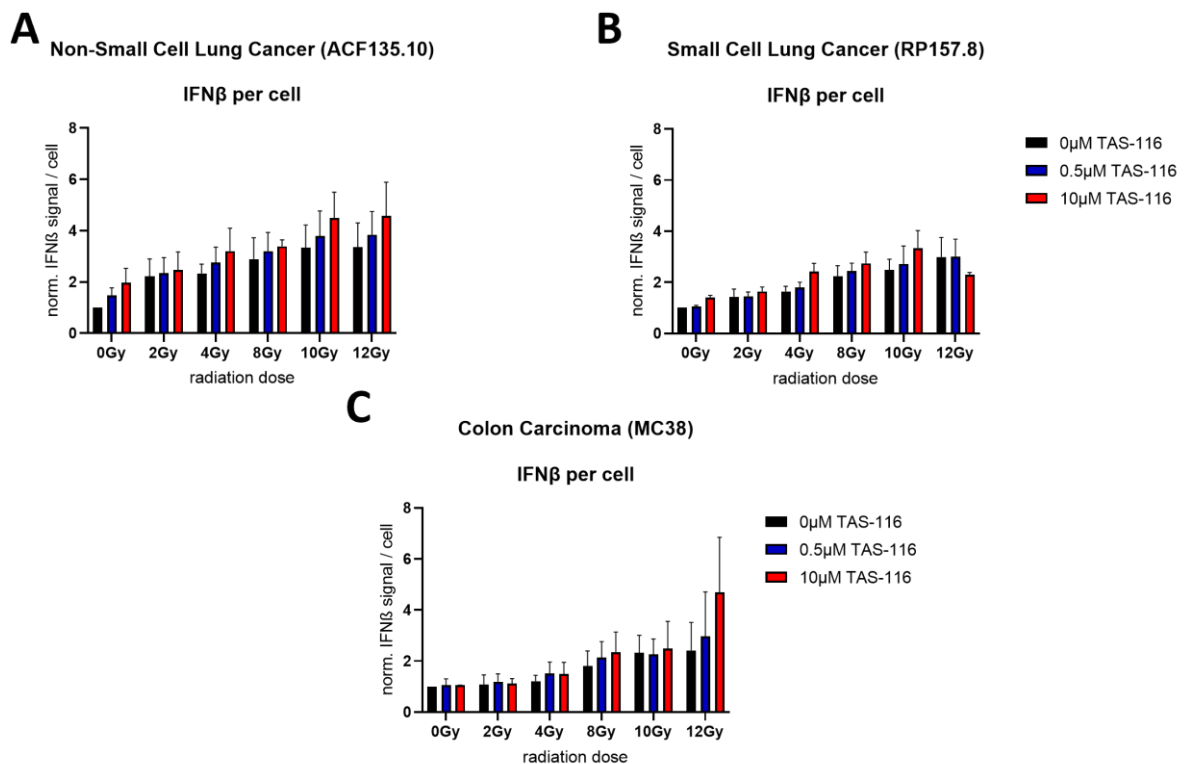


Figure 26: IFN β induction following RT and TAS-116 treatment

Tumor cells were treated with 0.5 and 10 μ M TAS-116, and irradiated one hour later. Cells were stained for IFN β 48 hours after irradiation. Normalized IFN β signal per cell is illustrated for ACF135.10 (A), RP157.8 (B), and MC38 (C) cells. Mean with SEM, n=3

Both TAS-116 treatment and RT alone exhibited a trend toward a concentration- and dose-dependent increase of IFN β secretion in ACF135.10 cells, respectively (Fig. 26A; Fig. 27). Moreover, HSP90 inhibition showed a tendency to further enhance the RT-induced response at radiation doses of at least 4 Gy in this cell line.

In RP157.8 cells, TAS-116 treatment seemed to mildly increase IFN β secretion only at a concentration of 10 μ M, whereas there was a dose-dependent trend toward enhanced staining mediated by RT alone throughout all groups. Mild additive effects of combined treatment were only observed in cells irradiated with 4, 8, and 10 Gy in combination with 10 μ M TAS-116 (Fig. 26B; Fig. 28). In line with the results obtained from the previous experiments, this trend did not proceed in the 12 Gy group.

MC38 colon carcinoma cells, however, were not found to visibly increase IFN β secretion following either treatment with TAS-116 or RT with doses lower than 8 Gy alone (Fig. 26C;

Fig. 29). TAS-116 at a concentration of 10 μM showed a tendency to increase IFN β secretion in MC38 cells only when combined with 12 Gy irradiation. In accordance with the previous experiments, the results did not reach statistical significance in any group.

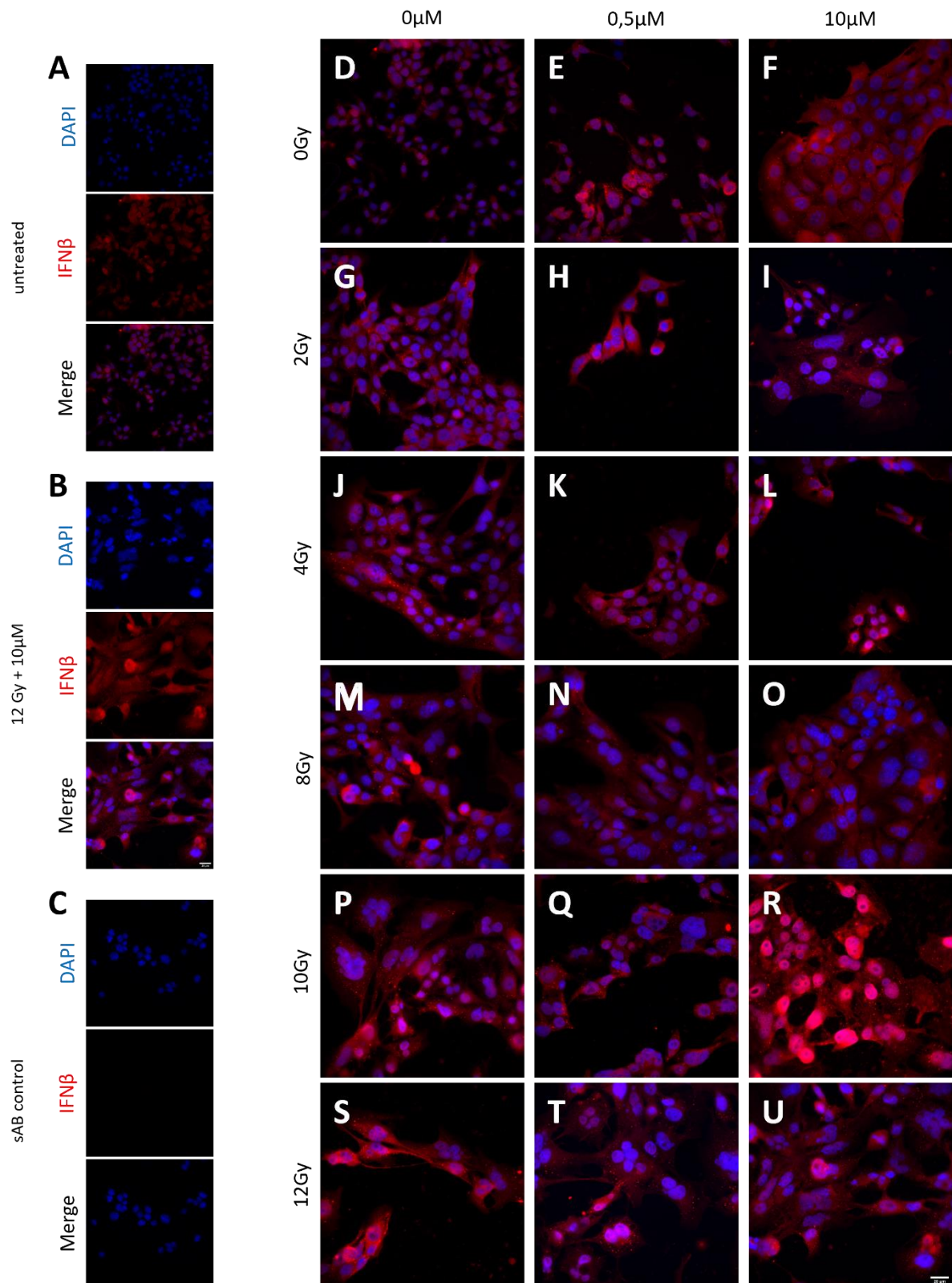


Figure 27: Immunofluorescence staining for IFN β on ACF135.10 cells

ACF135.10 cells were treated with 0.5 and 10 μ M TAS-116, irradiated one hour later, and stained with DAPI (blue) and anti-IFN β with Alexa Fluor 555 (red) 48 hours after irradiation. Single color images for untreated cells (A), cells treated with 12 Gy and 10 μ M TAS-116 (B), and for untreated cells stained without the secondary antibody (C) are shown. One exemplary multicolor picture is shown for every condition (D-U). Scale bar in B accounts for all images in A-C; Scale bar in U accounts for D-U. Scale bars correspond to 20 μ m.

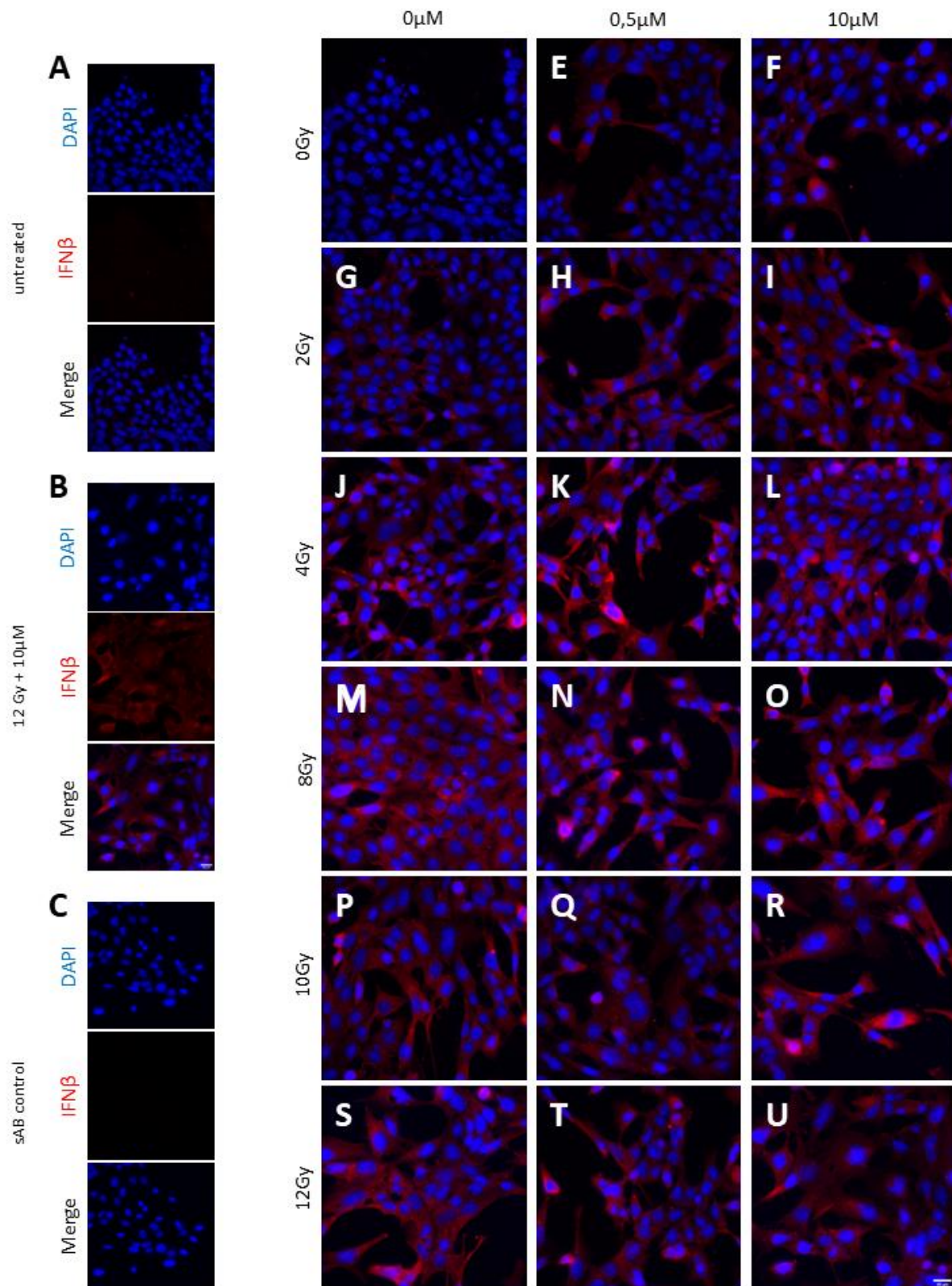


Figure 28: Immunofluorescence staining for IFN β on RP157.8 cells

RP157.8 cells were treated with 0.5 and 10 μ M TAS-116, irradiated one hour later, and stained with DAPI (blue) and anti-IFN β with Alexa Fluor 555 (red) 48 hours after irradiation. Single color images for untreated cells (A), cells treated with 12 Gy and 10 μ M TAS-116 (B), and for untreated cells stained without the secondary antibody (C) are shown. One exemplary multicolor picture is shown for every condition (D-U). Scale bar in B accounts for all images in A-C; Scale bar in U accounts for D-U. Scale bars correspond to 20 μ m.

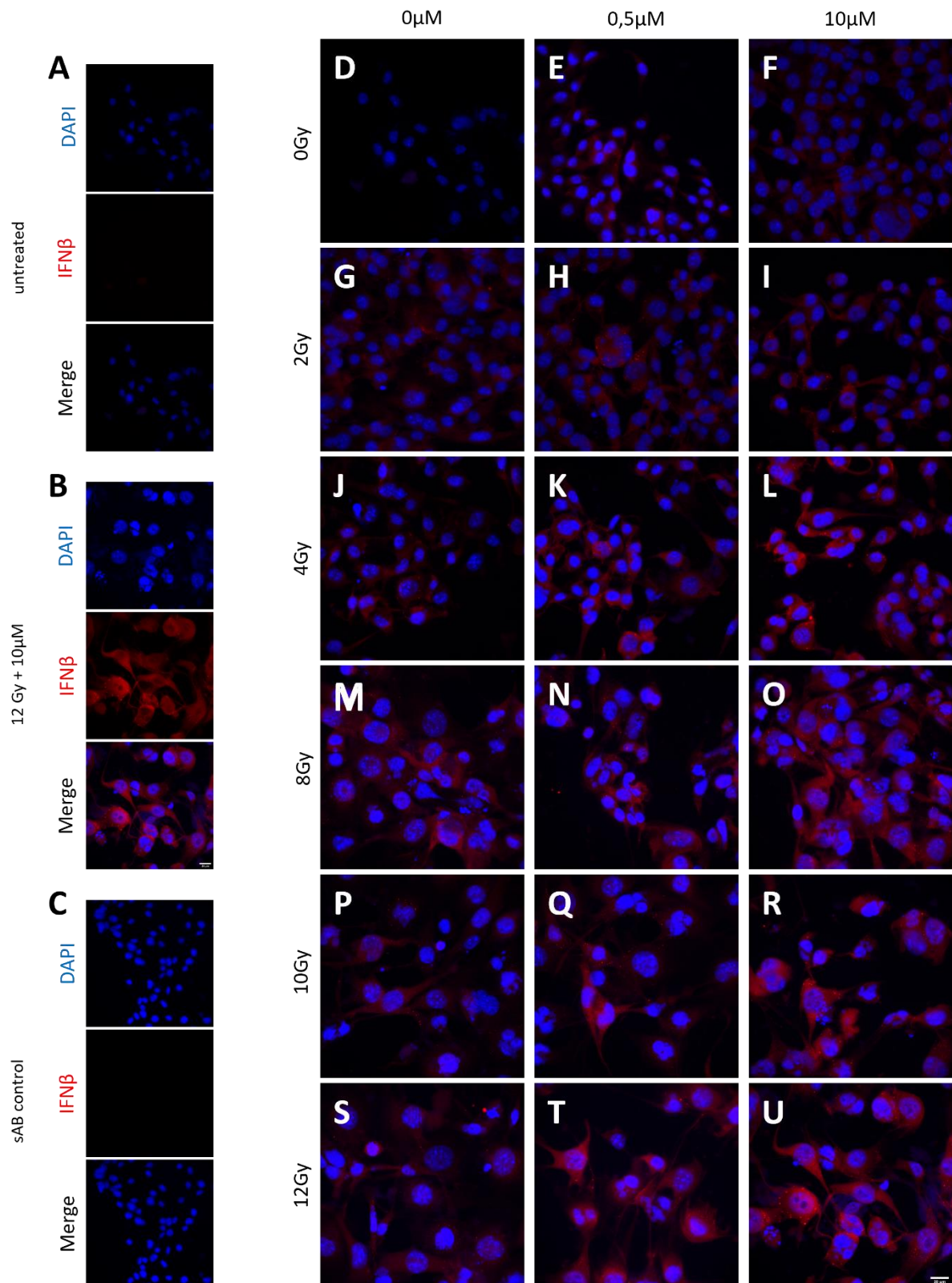


Figure 29: Immunofluorescence staining for IFN β on MC38 cells

MC38 cells were treated with 0.5 and 10 μ M TAS-116, irradiated one hour later, and stained with DAPI (blue) and anti-IFN β with Alexa Fluor 555 (red) 48 hours after irradiation. Single color images for untreated cells (A), cells treated with 12 Gy and 10 μ M TAS-116 (B), and for untreated cells stained without the secondary antibody (C) are shown. One exemplary multicolor picture is shown for every condition (D-U). Scale bar in B accounts for all images in A-C; Scale bar in U accounts for D-U. Scale bars correspond to 20 μ m.

5.4.4. Summary of cGAS/STING pathway analysis

Contrary to the previously described hypothesis on which this thesis is based, it can be stated that combinatory treatment of RT and HSP90 inhibition did not significantly increase activation of the cGAS/STING pathway *in vitro*. Nevertheless, trends with distinct differences between tumor cell lines could be observed.

Both HSP90 inhibition and RT up to 12 Gy individually displayed a tendency to induce cGAS/STING pathway activation in ACF135.10 NSCLC cells in a concentration- and dose-dependent manner, as was shown by immunofluorescence staining for cytosolic dsDNA, pSTING, and IFN β , respectively. A trend toward synergism of the combined treatment was observed for dsDNA and IFN β yet not for pSTING staining.

The results obtained from HSP90 inhibition alone were less distinct in RP157.8 SCLC cells for every staining. RT seemed to mildly enhance staining signal for dsDNA and IFN β but not for pSTING. Regarding the outcome of the combined study treatment, application of 0.5 μ M TAS-116 exhibited a trend to increase RT-induced upregulation of cytosolic dsDNA and pSTING for doses up to 10 Gy but barely enhanced the effects on IFN β secretion mediated by RT alone. TAS-116 at a concentration of 10 μ M, however, exhibited a tendency to increase IFN β secretion when administered prior to RT with 4, 8, or 10 Gy, respectively. In terms of dsDNA and pSTING induction, treatment with 10 μ M of the active ingredient resulted in greater effects than 0.5 μ M with the differences between the concentrations becoming more distinct, yet not statistically significant, with rising radiation doses. Interestingly, the mentioned trends were only observed in RP157.8 cells for radiation doses up to 10 Gy. Neither immunofluorescence signal for dsDNA, pSTING nor IFN β displayed a tendency to intensify further following 12 Gy irradiation but even decreased.

In line with the TAS-116 cytotoxicity assay, MC38 colon carcinoma cells hardly displayed a tendency to respond to the study treatment. Whereas HSP90 inhibition alone demonstrated a trend toward amplified dsDNA and pSTING staining signal, this was not the case for IFN β . The observed tendency of RT to induce enhancement of immunofluorescence signal eventually reached a plateau for every staining and addition of TAS-116 seemed to overcome this state only at high radiation doses. Although administration of 10 μ M TAS-116 seemed to result in enhanced occurrence of cytosolic dsDNA at a minimum radiation dose of 8 Gy, the lower concentration of the compound could not intensify staining signal up to 12 Gy. When analyzing induction of STING phosphorylation and IFN β secretion, respectively, a trend toward additive effects of the combined treatment could be observed only in the 12 Gy group.

5.5 CD8⁺ T cell-mediated killing

Upregulation of the cGAS/STING pathway by combined treatment with TAS-116 and RT was investigated under the assumption that it would ultimately improve tumor immunogenicity and therefore CD8⁺ T cell-mediated killing of tumor cells. To confirm this hypothesis, ACF133.3 NSCLC cells transduced to present the ovalbumin peptide SIINFEKL via MHC-I molecules on their surface were irradiated with 8 Gy either on ice or at room temperature. Cells were then given into co-culture together with OT-I derived CD8⁺ T cells at various time points following RT in effector to target ratios ranging from 2.5:1 to 30:1. The percentage of dead tumor cells was assessed five hours later via flow cytometry.

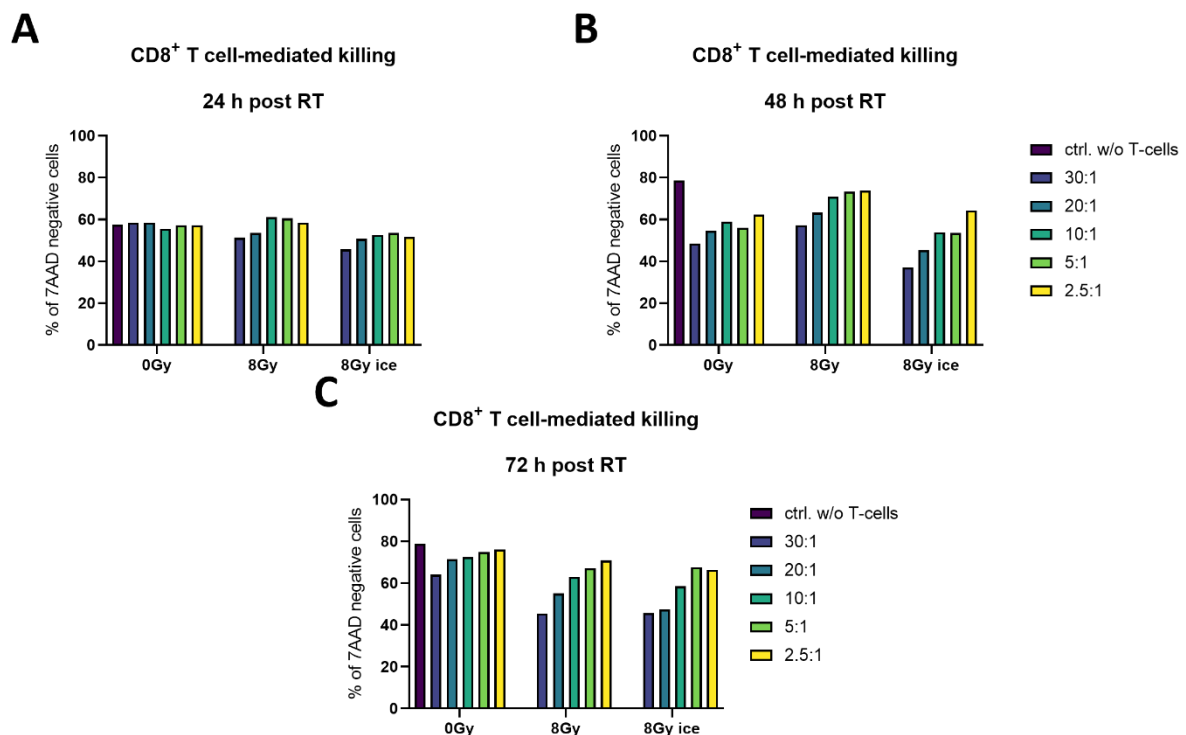


Figure 30: CD8⁺ T cell-mediated killing at different timepoints after RT

ACF133.3 cells were irradiated with 8 Gy at room temperature and on ice, respectively, and co-cultured with varying numbers of CD8⁺ T cells for five hours. Co-culture was set 24 (A), 48 (B), or 72 hours (C) after irradiation. The percentage of surviving tumor cells is illustrated. $n=1$

OT-I CD8⁺ T cells were not able to induce cell death of ACF133.3 cells when the co-culture was set up 24 hours after the tumor cells had received RT (Fig. 30A). T cell-mediated killing was, however, improved when cells were co-cultured either 48 or 72 hours after RT with effector to target cell ratios between 30:1 to 10:1 (Fig. 30B, C). Because this effect was slightly more distinct after 72 hours with cells irradiated on ice, this setup was maintained for the following experiments.

Killing assays were therefore conducted again as described above with ACF133.3 and OVA-transduced RP157.8 SCLC cells at an effector to target cell ratio of 30:1. CD8⁺ T cell-mediated

killing of ACF133.3 cells seemed to be slightly improved by RT alone, resulting in an approximately 10% reduction of surviving tumor cells (*Fig. 31A*). TAS-116 showed a tendency to improve CD8⁺ T cell-mediated killing at both concentrations tested in non-irradiated cells. However, only the higher concentration of 10 μM led to a mild enhancement of cell death induction in tumor cells that received 8 Gy irradiation. The proportion of 7-AAD positive tumor cells preincubated with 10 μM TAS-116 was approximately 12% higher in comparison to cells that received irradiation with 8 Gy alone, yet this was not statistically significant.

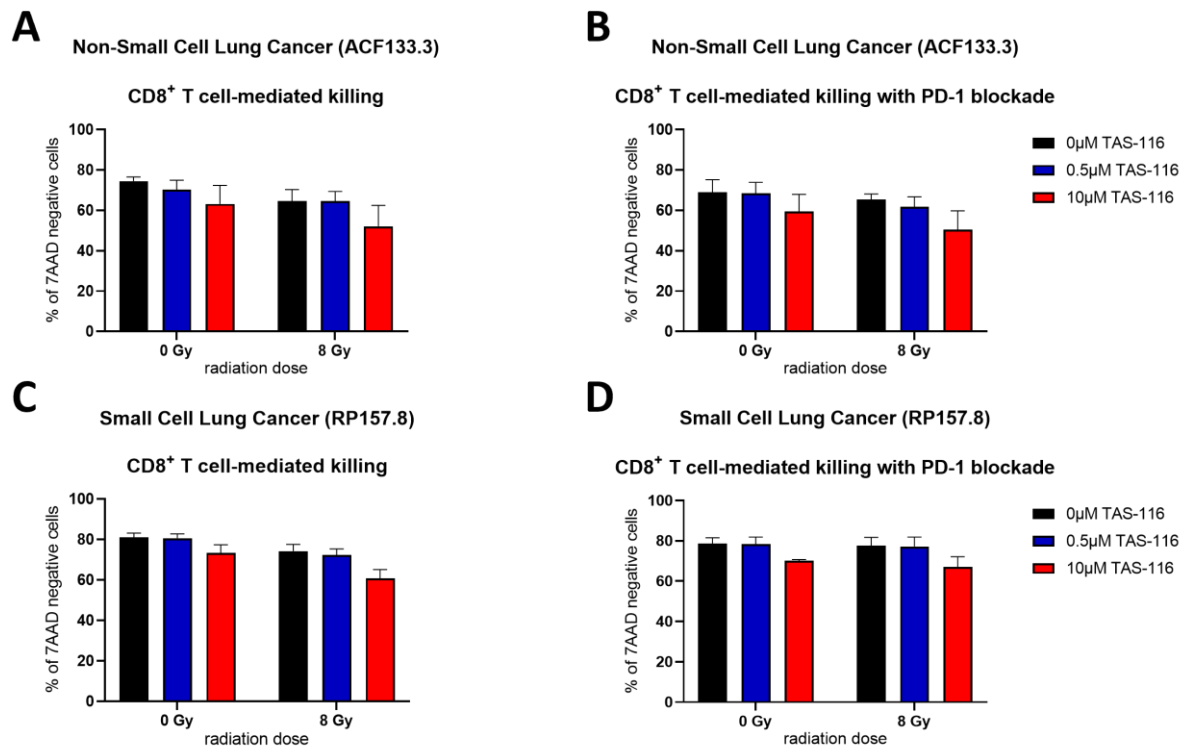


Figure 31: CD8⁺ T cell-mediated killing of tumor cells

Tumor cells were treated with 0.5 and 10 μM TAS-116, irradiated one hour later, and co-cultured with CD8⁺ T cells for five hours. Co-culture was set both with and without PD-1 blockade. CD8⁺ T cell-mediated tumor cell killing for ACF133.3 (A, B) and RP157.8 (C, D) is shown. Mean with SEM; n=4

In RP157.8 cells, on the other hand, administration of 0.5 μM TAS-116 resulted in improved CD8⁺ T cell-mediated killing neither for the irradiated nor the non-irradiated group (*Fig. 31C*). Preincubation with 10 μM TAS-116, however, obtained a similar trend as was observed in ACF133.3 cells.

Under the assumption that HSP90 inhibition would lead to upregulation of PD-L1 expression on tumor cells and blockade of PD-1/PD-L1 interaction would therefore further amplify CD8⁺ T cell-mediated killing, an antibody targeting PD-1 was added to the co-culture at a concentration of 10 μg/ml. This treatment, however, did not further enhance the observed effects in either cell line (*Fig. 31B, D*).

Because blockade of PD-1/PD-L1 interaction did not, as expected, result in improved CD8⁺ T cell-mediated killing in the previous experiment, I scrutinized whether PD-L1 and PD-L2 were, in fact, upregulated following the study treatment. To this end, ACF133.3 and RP157.8 cells were treated and irradiated as described before, and flow cytometric analysis for PD-L1 and PD-L2 expression on the tumor cell surface was performed approximately 77 hours after irradiation.

Irradiation with 8 Gy alone displayed a tendency to augment the expression of PD-L1 and PD-L2 in ACF133.3 cells by 1.2- and 1.3-fold, respectively. Whereas 0.5 μ M TAS-116 preincubation did not alter this effect, there was a trend toward further upregulation of ligand expression upon treatment with 10 μ M (Fig. 32A, B).

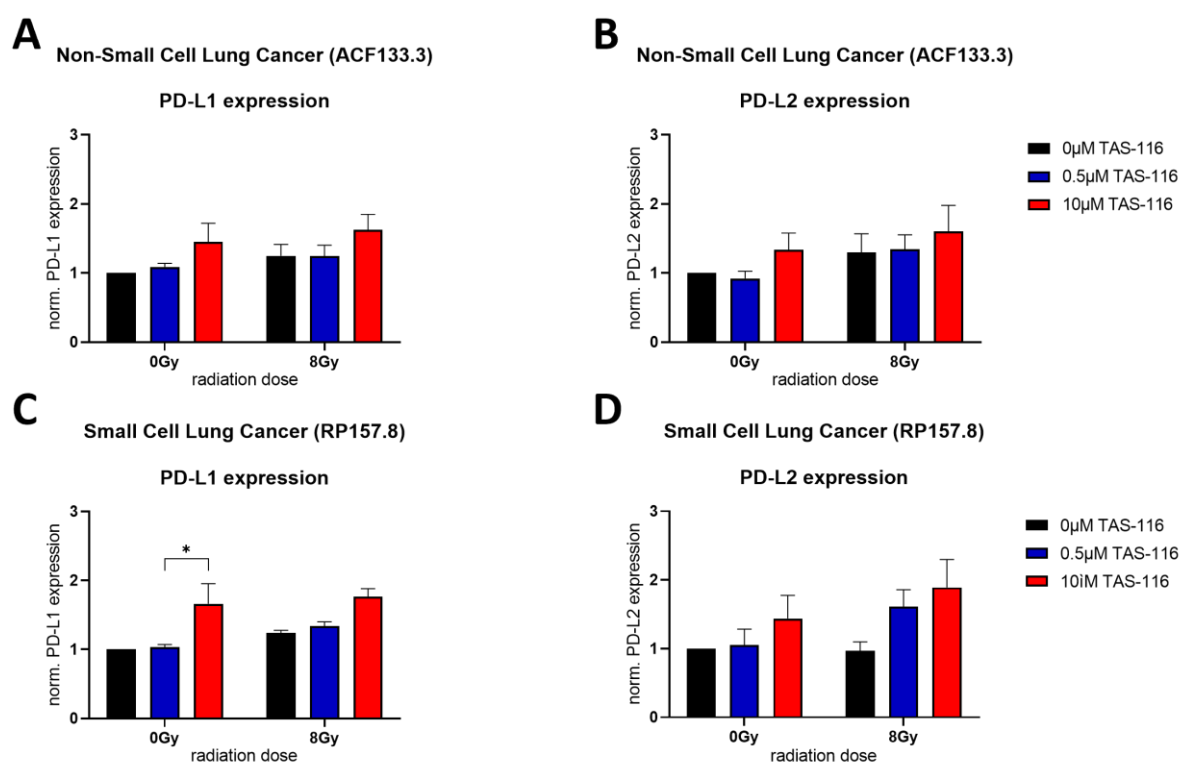


Figure 32: PD-L1 and PD-L2 expression following RT and TAS-116 treatment

Tumor cells were treated with 0.5 and 10 μ M TAS-116, irradiated one hour later, and stained for PD-L1 and PD-L2 approximately 77 hours later. Normalized PD-L1 and PD-L2 expression is shown for ACF133.3 (A, B) and RP157.8 (C, D) cells. Mean with SEM; n=5; *p<0.05

Alterations of PD-L1 expression on RP157.8 cells following RT were comparable to NSCLC cells. However, 8 Gy RT did not result in upregulation of PD-L2 expression on the tumor cell surface (Fig. 32C, D). Whereas preincubation with 0.5 μ M, again, did not surpass the RT-mediated effects regarding PD-L1 expression, the latter was significantly increased following treatment with 10 μ M TAS-116 by 1.6-fold compared to cells treated with the drug at a concentration of 0.5 μ M. There was a trend toward enhanced expression of the ligand following treatment with 10 μ M TAS-116 one hour prior to irradiation with 8 Gy as well, yet this was not

statistically significant. The only time the lower concentration of TAS-116 displayed a mild effect in this experiment was upon analysis of PD-L2 expression on RP157.8 cells that also received RT. Increase of the TAS-116 concentration seemingly further magnified this upregulation.

It was therefore shown that there was a trend toward upregulation of both PD-L1 and PD-L2 expression following HSP90 inhibition and RT on ACF133.3 NSCLC and RP157.8 SCLC cells in vitro. This effect was statistically significant in non-irradiated RP157.8 cells that had received TAS-116 at the higher concentration. It would be worthwhile testing different concentrations of the antibody for future experiments as well as assessing the best time point for administration.

5.6 Analysis of TCR clonality

Finally, since the cytotoxic activity of CD8⁺ T lymphocytes depends on target cell recognition via TCRs, it was investigated whether RT with and without prior TAS-116 treatment would affect the TCR clonality of infiltrating T lymphocytes in vivo. To this end, WT mice bearing ACF135.10 flank tumors received 8 Gy irradiation per tumor either alone or following treatment with TAS-116 one hour prior. Mice were sacrificed seven days after RT, and TCR expression on CD4⁺ and CD8⁺ T lymphocytes obtained from the spleen, blood, and tumor tissue was assessed by flow cytometry.

In CD4⁺ T cells derived from the spleen, neither RT alone nor in combination with HSP90 inhibition obtained any effect regarding TCR clonality (*Fig. 33B*). CD4⁺ T lymphocytes infiltrating the tumor tissue, however, displayed upregulation of six TCRs (*Vα3.2, Vα8.3, Vα11.1/11.2, Vβ8.3, Vβ11[RR3-15], Vβ13*) following TAS-116 treatment and RT (*Fig. 33A*). Of those, only *Vα8.3* and *Vβ11[RR3-15]* were likewise upregulated on T helper cells obtained from the blood, whereas *Vβ13* was found to be downregulated in blood CD4⁺ lymphocytes (*Fig. 33C*).

Regarding CD8⁺ T cells, on the other hand, the study treatment resulted in upregulation of four TCRs (*Vα11.1/11.2, Vβ5.1/5.2, Vβ7, Vβ12*) on cells obtained from the spleen (*Fig. 33D*), of which *Vα11.1/11.2* and *Vβ5.1/5.2* were likewise upregulated on blood CD8⁺ lymphocytes (*Fig. 33F*). While these two TCRs, however, were not distinctly altered on tumor infiltrating cytotoxic T cells, *Vβ7* and *Vβ12* TCRs were here found to be inversely downregulated (*Fig. 33E*).

Interestingly, several TCR clones, especially on tumor infiltrating CD8⁺ T cells, seemed to be upregulated by RT alone but not so much following combined treatment with the HSP90 inhibitor TAS-116 (*Vα3.2, Vα8.3, Vα11.1/11.2, Vβ2, Vβ8.3, Vβ9, Vβ11[RR3-15]*). Moreover, the only TCR clones identified to be upregulated in both tumor infiltrating CD4⁺ and CD8⁺ T cells were *Vβ8.3* and *Vβ13*. However, these results need further validation.

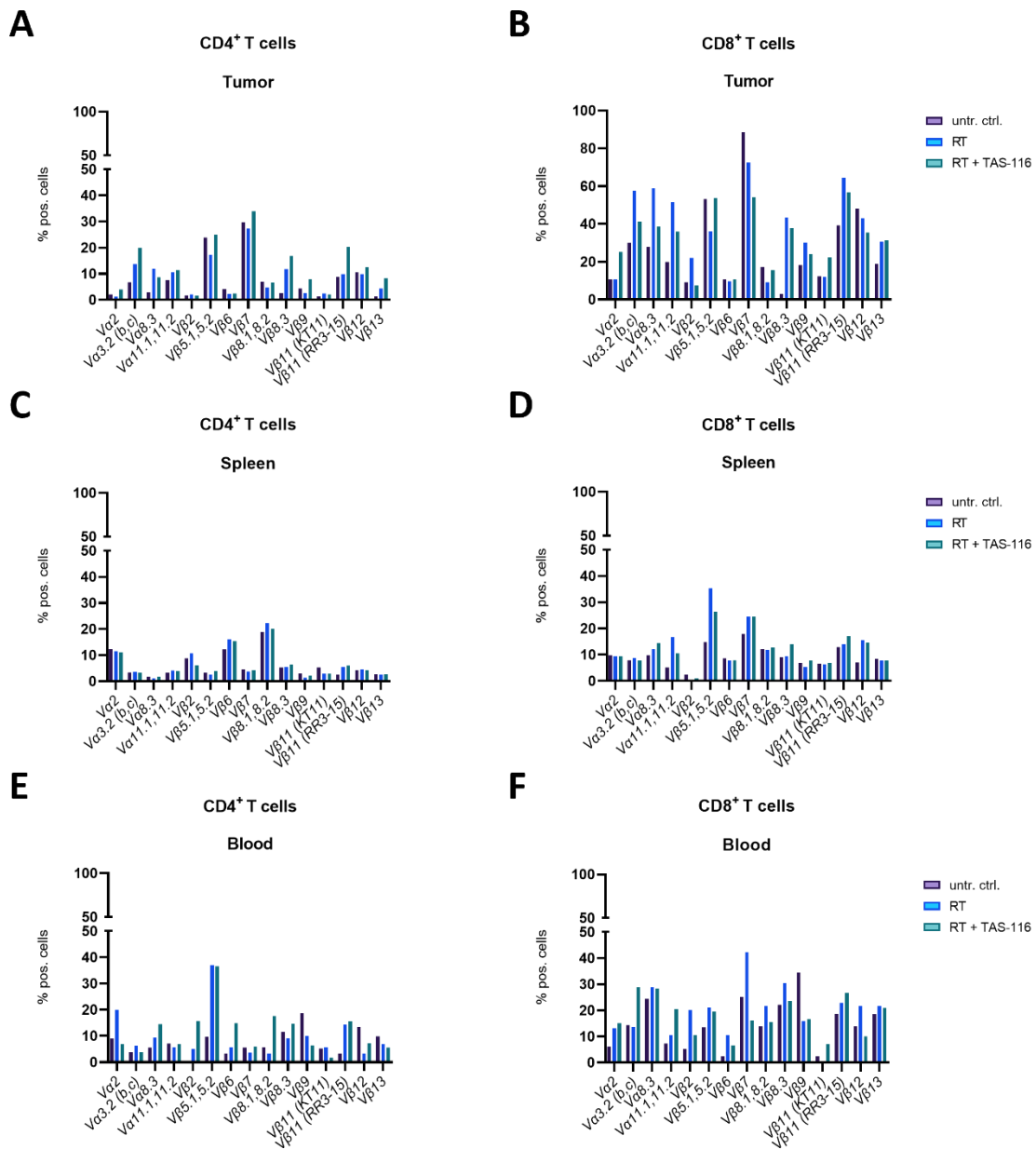


Figure 33: T cell receptor expression

WT mice bearing ACF135.10 flank tumors were treated with TAS-116 and irradiated with 8 Gy per tumor one hour later. Mice were sacrificed seven days after irradiation. Cells obtained from tumors, spleen, and blood were stained for CD4, CD8, and T cell receptor clones. TCR expression on CD4⁺ (A, B, C) and CD8⁺ (D, E, F) T cells is illustrated. n=1

6. Discussion

The aim of this thesis was to investigate the possible synergistic effects of HSP90 inhibition and RT on tumor immunogenicity. Therefore, activation of the cGAS/STING pathway by the HSP90 inhibitor TAS-116 in combination with RT in various dosing regimens was analyzed. To elaborate tumor type-specific differences, this thesis mainly focused on MC38 colon carcinoma, RP157.8 SCLC, and ACF135.10 NSCLC cells.

6.1 Effects of HSP90 inhibition and RT on MC38 cells

The murine MC38 colon adenocarcinoma cell line is widely used in preclinical immunology models. RT was previously found to yield substantial benefits on MC38 tumor growth *in vivo* only in rather high doses. However, mice bearing subcutaneous MC38 tumors responded well to moderate radiation doses in combination with checkpoint blockade¹⁶⁸. Regardless of RT seldom being of importance in the treatment of colon carcinoma patients clinically, the MC38 cell line was thus included in this work due to its favorable responsiveness toward combinatory treatment regimens including RT and immunomodulatory approaches.

Regarding cytotoxicity of TAS-116, MC38 cells displayed a substantially greater resistance to the drug with an IC₅₀ value more than ten-fold higher than the other cell lines tested (*Fig. 7*). Said resistance was confirmed via staining with PI 72 hours after treatment where administration of 0.5 μ M TAS-116 was found to not induce cell death in MC38 cells, whereas application of 10 μ M TAS-116 showed a tendency to do so (*Fig. 8C*). Moreover, MC38 cells displayed only a very mild sensitivity toward RT in this experiment. RT with 12 Gy resulted in detection of 17.7% more PI positive cells compared to non-irradiated cells. While this effect was dose-dependent it only represented a rather flat ascent with no increase from 4 to 8 Gy and 10 to 12 Gy, respectively. Preincubation with 10 μ M TAS-116 one hour prior to RT further enhanced the percentage of PI positive cells for every radiation dose in line with its toxicity on colon carcinoma cells by itself, yet this was not statistically significant. Application of the lower concentration, however, did not yield synergistic effects regarding induction of cell death when combined with RT in doses up to 8 Gy. For irradiation with 10 and 12 Gy, respectively, the proportion of PI positive cells observed following pretreatment with 0.5 μ M TAS-116 exceeded that of non-treated cells yet still did not reach the effect of the 10 μ M group.

The results observed upon analysis of DNA double-strand breaks in MC38 cells induced by RT alone mimicked the results previously mentioned in that there was an overall trend toward dose-dependent induction of DNA double-strand breaks but no visible effect between cells irradiated with 4 and 8 Gy or 10 and 12 Gy, respectively (*Fig. 13C*). In terms of γ H2AX staining, MC38 cells seemingly neither reacted to TAS-116 monotreatment nor was there any trend toward a synergistic induction of DNA double-strand breaks upon combination with RT.

However, induction of apoptosis or necrosis by the HSP90 inhibitor TAS-116 should be due to its impairment of DDR mechanisms. Therefore, DNA damage is bound to precede the cells' uptake of PI and the results obtained from γ H2AX staining are most likely owing to a sub-optimal experimental setup. It has previously been shown that phosphorylation of histone H2AX indicating DNA double-strand breaks sets in within seconds of tumor irradiation in vivo and already decreases within two hours¹⁶⁹. It is thus not surprising that while there was a trend toward ascension of γ H2AX signal with rising radiation doses three hours after RT in each cell line, this was not very prominent. Unexpectedly, there were no statistically significant alterations in γ H2AX staining signal by concomitant HSP90 inhibition, either. By fixing the cells three hours after RT, I aimed at differentiating the extent of DNA double-strand breaks in cells with impaired DDR from cells with such mechanisms intact. In that regard, the HSP90 inhibitor TAS-116 has already been shown to increase phosphorylation of histone H2AX in human cervical carcinoma cells (HeLa cells) irradiated with 2 Gy and this effect prevailed up to 24 hours after RT¹⁷⁰. The experimental setup differed from this thesis in so far as HeLa cells were preincubated with 1 μ M TAS-116 for 24 hours prior to RT and the active ingredient was washed out directly afterward. This way, the authors achieved a cell cycle arrest in the G2/M phase which has been shown to render cells most susceptible to RT¹⁷¹. Considering this, preincubation with TAS-116 for only one hour is likely to result in upregulation of γ H2AX foci to a lesser extent. Another influencing factor might be the method of analysis. Because one γ H2AX focus in the nucleus is equivalent to one DNA double-strand break¹⁷² the latter are usually quantified via counting of foci. This method, however, reaches practical limits when high radiation doses are applied due to the vast number of foci that would need to be counted per nucleus. Instead, global γ H2AX phosphorylation levels were quantified in this study by measuring the integrated density, i.e., the sum of all fluorescence pixel values, within the nucleus. Whereas measurement of total γ H2AX phosphorylation levels per cell has been described before as an alternative to foci counting, there are known shortcomings to this method. It was found, for example, that the number of γ H2AX foci in hamster ovarian cells irradiated with 2 Gy decreased faster than the global γ H2AX signal¹⁷³. The authors suggest an increase in the size of the remaining foci, higher phosphatase activity within the foci, or a redistribution of γ H2AX in chromatin as possible explanations for this finding. It can thus not be ruled out that the assay performed for this thesis yielded questionable results as the number of foci in cells that did not undergo HSP90 inhibition might have decreased further than in treated cells, yet this was not detectable by the method of analysis.

Next, activation of the cGAS/STING pathway was analyzed via quantification of dsDNA in the cytosol, STING phosphorylation, and IFN β secretion. Administration of TAS-116 showed a concentration-dependent tendency to increase the occurrence of cytosolic dsDNA and pSTING alike in MC38 cells (*Fig. 18C, Fig. 22C*). Likewise, irradiation with 2 Gy resulted in

enhanced dsDNA and pSTING signal, yet this was not statistically significant. Rising radiation doses further enhanced this effect only mildly. A trend toward synergistic potential for enhancement of cytosolic dsDNA in colon carcinoma cells was seen for TAS-116 at a concentration of 10 μM and radiation doses of at least 8 Gy while administration of 0.5 μM did not exceed the level of cells that received RT alone up to 12 Gy. This observed trend, however, was even less pronounced regarding STING phosphorylation.

In accordance with TAS-116 only displaying a tendency to slightly induce phosphorylation of STING protein individually in MC38 cells, it did not result in complete cGAS/STING pathway activation as measured by IFN β secretion, either. Additionally, the cells' reaction to RT in this regard was likewise delayed and overall weaker with an ascent from 8 Gy on (*Fig. 26C*). This phenomenon is most likely due to impaired stabilization of TBK1 which is a client protein of HSP90 and therefore affected by the latter's inhibition¹⁶⁶. As previously described, TBK1 is essential for STING phosphorylation which in turn is indispensable for completion of the pathway and ultimately for secretion of type I IFNs. Thus, impairment of TBK1 activity could explain the attenuated and delayed signal increase in the immunofluorescence staining performed here. The further downstream of the cGAS/STING pathway an effect occurs, the more intensive treatment regimens are necessary to enhance it.

6.2 Effects of HSP90 inhibition and RT on RP157.8 cells

Even though treatment options have advanced in recent years, prognosis for patients bearing SCLC tumors is still poor with a 2-year survival of 14-15%¹³. New treatment approaches, such as combination regimens utilizing RT and immunotherapeutic agents, are thus of utmost clinical importance. The SCLC cell line RP157.8, which is driven by both *RB1* and *Trp53* knockout, the most commonly found mutations in SCLC tumors overall¹¹, was therefore included in this thesis.

RP157.8 cells proved to be a lot more susceptible toward treatment with TAS-116 than MC38 colon carcinoma cells, as was shown in the cytotoxicity assay (*Fig. 7B*). I therefore assumed that the lower concentration of 0.5 μM TAS-116 would yield greater effects in this cell line.

While treatment with 0.5 μM had resulted in an increase in 7-AAD positive cells in the cytotoxicity assay by 17%, no such effect was observed upon staining with PI 72 hours after treatment (*Fig. 8B*). One explanation for this observation could lie within the different incubation times, i.e., 24 hours for the cytotoxicity assay and seven hours for PI staining. There was a visible trend upon treatment with 10 μM of the active ingredient, however. Irradiation alone displayed a tendency to induce cell death from 4 Gy on in a dose-dependent manner. Comparable to MC38 cells, no significant synergistic effects were observed for any treatment condition and the trend following preincubation with TAS-116 at the lower concentration was

only observed for the 10 and 12 Gy groups, whereas 10 μ M TAS-116 exceeded the non-treated cells for every radiation dose. While this response grew more pronounced with rising radiation doses in MC38 cells, the difference between cells that had received RT alone and RP157.8 cells pretreated with 10 μ M TAS-116 remained relatively constant throughout all groups.

Similar to the colon carcinoma cell line, monotreatment with TAS-116 did not significantly enhance the γ H2AX staining signal in RP157.8 cells, although the radiosensitivity results were consistent with the counted PI positive cells from the previous experiment (*Fig. 13B*). Furthermore, there was a mild trend toward synergistic induction of DNA double-strand breaks for radiation doses ranging from 2 to 10 Gy after preincubation with either concentration of the compound. In cells irradiated with 8 and 10 Gy, results achieved by administration of 10 μ M TAS-116 overtook the lower concentration. Unexpectedly, γ H2AX signal seemed to decline in cells irradiated with 12 Gy and preincubated with either concentration of TAS-116. Because this trend was also observed in all subsequent immunofluorescence stainings of RP157.8 cells, but administration of TAS-116 had shown a trend toward an increased percentage of dead cells in the 12 Gy group, I first hypothesized that DNA damage from this combined treatment may have exceeded the DDR capability of the cells and therefore the cells had already undergone cell death at the time of staining.

Moreover, phosphorylation of histone H2AX is known to be mediated by different kinases depending on the triggering factor. While ataxia telangiectasia mutated kinase (ATM) is primarily responsible for H2AX phosphorylation in response to DNA double-strand breaks following RT, phosphorylation of H2AX during apoptosis is solely mediated by DNA-dependent protein kinase (DNA-PK)¹⁷⁴. ATM is a client protein of HSP90 α , and inhibition of the latter has been shown to promote its proteasomal degradation¹⁷⁵. Additionally, ATM is responsible for phosphorylation of nuclear HSP90 α directly after RT and this process correlates with histone H2AX phosphorylation¹⁷⁶. In accordance, γ H2AX formation following RT was reduced in HSP90 α deficient cells regardless of HSP90 β levels in the same study. Another study had demonstrated before that silencing of HSP90 α impaired maintenance of γ H2AX foci, yet not total γ H2AX levels, after RT but treatment of the same cells with the HSP90 α inhibitor 17-allylamino-17-demethoxy-geldanamycin (17-AAG) did not yield the same effect¹⁷⁷. The authors thus suggest that while DNA repair mechanisms mediated by HSP90 α are inhibited by 17-AAG, phosphorylation of the chaperone is not. Likewise, DNA-PK is a known client of HSP90 α as well, and downregulation of the latter therefore reduces DNA-PK-mediated γ H2AX formation in apoptotic cells¹⁷⁸. Significantly in this context, the γ H2AX distribution pattern in cells undergoing apoptosis, e.g., due to severe DNA damage, is distinctly different from γ H2AX foci representing DNA double-strand breaks. Nuclei of early apoptotic cells display an annular γ H2AX staining, referred to as the apoptotic ring, which later propagates to a pan-nuclear staining pattern¹⁷⁹. As was already discussed earlier on, the method of γ H2AX staining analysis

in this thesis does not allow to distinguish with certainty between foci, pan-nuclear staining or cells possibly marked by both patterns. With respect to the results indicating a decline of γ H2AX staining intensity in RP157.8 cells treated with TAS-116 and irradiated with 12 Gy, it is thus possible that phosphorylation of histone H2AX in this setting is downregulated due to impaired stabilization of ATM and DNA-PK by HSP90 α . The non-functional form of the chaperone might still be phosphorylated upon inhibition at first. However, it seems likely that extensive inhibition of HSP90 α and henceforth ATM and DNA-PK will forestall phosphorylation of HSP90 α and therefore γ H2AX foci formation above a certain threshold.

Regarding activation of the cGAS/STING pathway, administration of TAS-116 resulted in a concentration-dependent trend toward upregulation of both dsDNA and pSTING in RP157.8 cells (*Fig. 18B, 22B*). However, the lower concentration of 0.5 μ M did not seem to influence the induction of IFN β secretion at all (*Fig. 26B*). In contrast, irradiation alone showed a tendency to gradually increase the intensity of dsDNA and IFN β but not pSTING staining. In line with these results, a synergistic tendency for pathway activation up to the STING phosphorylation step was observed using radiation doses up to 10 Gy with both concentrations of the active ingredient, yet only preincubation with 10 μ M TAS-116 resulted in possible completion of the pathway as quantified by IFN β secretion. None of the observations mentioned reached statistical significance.

6.3 Effects of HSP90 inhibition and RT on ACF135.10 cells

The final cell line included in this study was the *Trp53/KRAS* driven ACF135.10 NSCLC cell line. Even though the IC50 value determined for this cell line in the cytotoxicity assay was comparable to that of RP157.8 cells (115.1 and 168.4 μ M, respectively; *Fig. 7A, B*), results obtained from PI staining seemed to display some differences (*Fig. 8A*).

While for most cell lines tested the percentage of PI positive cells ascended to values between approximately 49 and 59% following the most intense treatment regimen, the maximum observed proportion of PI positive ACF135.10 cells was only approximately 15%. Possible explanations for this phenomenon lay within the design of the assay. The nuclear and chromosome counterstain PI intercalates into the DNA upon entering the nucleus and is commonly used to identify necrotic and late apoptotic cells. It is prevented from entering the cell as long as the cellular membrane is intact and therefore does not stain viable or early apoptotic cells¹⁶¹. A study using human HCT116 colon carcinoma cells demonstrated that HSP90 inhibition enforced RT-induced apoptosis and accelerated transit into necrosis in a concentration-dependent manner in vitro¹⁸⁰. The same study deployed radiation doses up to 5 Gy and found that, while nearly 100% of treated cells entered apoptosis within 48 hours of irradiation, the percentage of necrotic or late apoptotic, i.e., PI positive cells, was still ascending

after 72 hours, rendering them clearly distinguishable to untreated cells. For this thesis, irradiation was applied in doses as high as 12 Gy. I therefore assumed that treatment-mediated differences regarding the induction of cell death could be best quantified via PI staining 72 hours following RT. However, it cannot be ruled out that the ideal setup or time point of measurement, respectively, could be different depending on the cell line. Apart from *KRAS/Trp53* mutated lung cancer cells displaying high resistance to RT in general¹⁸¹ another possible explanation for the apparent relative unresponsiveness of ACF135.10 cells in this experiment could thus be that transition to necrosis, including permeabilization of the cellular membrane, might take longer in these cells. In this regard, it is worth considering whether staining at another time point might have yielded significant results in the other cell lines as well.

Nevertheless, there was still an apparent trend toward induction of cell death by TAS-116 treatment at a concentration of 10 μ M visible for this cell line. While RT alone yielded no effect in this regard for doses up to 10 Gy, the number of PI positive cells counted increased following RT with 12 Gy, although not significantly. Interestingly, even though TAS-116 had displayed slightly higher cytotoxicity on ACF135.10 than RP157.8 cells in the first experiment, the trend observed in NSCLC cells regarding their responsiveness toward combined treatment with RT in the PI staining assay was less marked than in SCLC cells. The proportion of dead cells showed a tendency to rise dose-dependently only for RT doses of at least 8 Gy with the 0.5 μ M approaching the 10 μ M group when combined with irradiation of 10 and 12 Gy, respectively. However, as previously mentioned, these results are to be interpreted with caution due to the overall low percentage of PI positive cells for this cell line.

Regarding immunofluorescence staining for γ H2AX, no effect following TAS-116 treatment alone was observed for either concentration, whereas γ H2AX staining signal was incrementally upregulated by all radiation doses individually, although this was not statistically significant (*Fig. 13A*). A trend toward synergism of RT and HSP90 inhibition seemingly set in at 4 Gy irradiation for the higher and at 10 Gy for the lower TAS-116 concentration, respectively.

Both TAS-116 and RT individually exhibited a tendency toward a concentration- and dose-dependent augmentation of the staining signal for dsDNA, pSTING, and IFN β (*Fig. 18A, 22A, 26A*). Whereas both 0.5 and 10 μ M TAS-116 preincubation displayed a tendency to enhance RT-mediated upregulation of cytosolic dsDNA in all groups, this trend was hardly visible for STING phosphorylation. However, a synergistic tendency of HSP90 inhibition and RT was again perceived for radiation doses of at least 4 Gy in cells stained for IFN β .

6.4 Effects of HSP90 inhibition and RT on CTL-mediated killing of tumor cells

Next, I was interested whether combination of HSP90 inhibition and RT would result in enhanced tumor cell killing by CD8⁺ T cells. As I observed trends toward enhanced secretion of IFN β in both lung cancer cell lines yet not in MC38 cells, the killing assay was conducted solely with OVA-transduced RP157.8 and ACF133.3 cells, another subset of the ACF135.10 cell line.

There was a weak trend toward enhanced CD8⁺ T cell-mediated killing of NSCLC cells following administration of both 0.5 and 10 μ M TAS-116 but the lower concentration did not yield such an effect on RP157.8 cells (*Fig. 31*). Rather unexpectedly, the tendency to enhance tumor cell killing by irradiation with 8 Gy was slightly more pronounced in ACF133.3 than RP157.8 cells, even though NSCLC cells had displayed a trend toward upregulation of IFN β secretion to a somewhat lesser extent. Combined treatment of HSP90 inhibition and RT with 8 Gy conveyed a trend toward synergism of CD8⁺ T cell-mediated killing only with TAS-116 at a concentration of 10 μ M in both cell lines.

Hence, the effects displayed in this study were only mild and not statistically significant. Yet it has been published before that HSP90 inhibition does improve tumor cells' response to CTL-mediated lysis. Whereas CD8⁺ T cell-mediated killing of human melanoma cells was enhanced following treatment with ganetespib for 24 hours¹⁸², another study stated that induction of differentiating antigens, ultimately leading to increased T cell recognition of melanoma cells in vitro even required continuous inhibition of HSP90 for 48 hours¹⁸³. While the enhancement of effector functions of CTLs was traced back to an upregulation of IFN response genes in the first study by Mbofung et al.¹⁸², another study on sarcoma cells found proteasomal degradation of antigens to be improved upon administration of the HSP90 inhibitor 17-Dimethylaminoethylamino-17-demethoxy-geldanamycin (17-DMAG), ultimately leading to prolonged recognition of tumor cells by CD8⁺ T cells in vitro and in vivo¹⁸⁴. Contrary to these results, however, it has been reported that HSP90 inhibition, even though not affecting synthesis, does inhibit peptide loading onto MHC-I molecules, therefore impeding antigen presentation as well as cross-priming¹⁸⁵.

Furthermore, RT evidentially sensitizes tumor cells toward CD8⁺ T cell-mediated killing in vitro. Two studies found that murine MC38 and human CRC cells were more susceptible toward CTL-mediated killing when co-cultured with antigen specific CD8⁺ T cells for 18 hours 24 or 72 hours after RT, respectively^{186,187}. The effector to target cell ratios in these studies ranged from 12.5:1 up to 100:1 with MC38 cells displaying statistically significant differences compared to non-irradiated cells only when co-cultured with T cells at the highest ratio. Interestingly, Chakraborty et al.¹⁸⁷ found the death receptor Fas to be upregulated in MC38 cells upon RT with 20 Gy and blocking its interaction with the respective ligand on T cells

reversed RT-mediated sensitization toward cytolysis. However, whereas the study by Garnett et al.¹⁸⁶ likewise observed Fas upregulation, CTL-mediated killing was apparently not dependent on this effect. Another study conducted similarly to the aforementioned, yet coculturing tumor and T cells for four to five hours only, uncovered that human CRC cells were sensitized toward CD8⁺ T cell-mediated killing only when at least one of the co-stimulatory molecules OX-40 ligand (CD134L) or 4-1BBL (CD137L) were upregulated following RT¹⁸⁸. Both ligands belong to the TNF family of T cell co-stimulators and, upon interaction with their respective receptors on T cells, promote T cell proliferation and cytokine production¹⁸⁹. Whereas 4-1BBL was found to be expressed on human lung cancer cells yet not healthy lung tissues¹⁹⁰, OX-40L seems to be expressed on both SCLC and NSCLC cells only rarely^{191,192}. Apart from said sensitizing effects, however, RT can impede antitumor immunity, as well. Secretion of Type I IFNs following RT-mediated activation of the cGAS/STING pathway has been shown to induce expression of SERPINB9, an inhibitor of granzyme B. With the latter being an important mediator of T cell cytotoxicity, RT can thus contribute to tumor cell resistance toward T cell-mediated killing¹⁹³.

Next, it was analyzed whether PD-1/PD-L1 checkpoint blockade would enhance CD8⁺ T cell-mediated killing of ACF133.3 and RP157.8 cells in this experimental setup. Surprisingly, this was not the case for either cell line even though PD-L1 expression was significantly upregulated upon treatment with 10 μ M TAS-116 in RP157.8 cells. Moreover, there was a trend toward PD-L1 and PD-L2 upregulation both by RT and TAS-116 treatment alone as well as by combined treatment (*Fig. 32*). This is in accordance with a study that found enhanced CTL-mediated lysis of murine breast and pancreatic cancer cells following RT even with an effector to target cell ration as low as 1:10 yet no enhancement by administration of an anti-PD-L1 antibody regardless of PD-L1 upregulation on the tumor cells¹⁹⁴. The authors hypothesize that CD8⁺ T cells in their setting had already been activated maximally and blocking of PD-1/PD-L1 interaction therefore yielded no further effect. In contrast, PD-L1 blockade has been shown to improve tumor cell killing by itself as well as in combination with inhibitors of poly ADP ribose polymerase (PARP) *in vitro*^{195,196}. Noteworthy, however, both studies used antibodies targeting PD-L1 which have been shown to be more effective than PD-1 antibodies, as used in this work¹⁹⁷.

6.5 Effects of HSP90 inhibition and RT on TCR clonality

By enhancing and preserving DNA damage in irradiated tumor cells, TAS-116 bears the potential of improving the presentation of neoantigens. However, not all neoantigens ultimately promote a tumor-specific T cell response. Rather than addressing this hypothesis directly, tumor immunogenicity is therefore better analyzed by quantification of the immune response

itself. As T cell-mediated effects are dependent on recognition of antigens via TCR on lymphocytes, TCR clonality can yield valuable information on the anti-tumor immune response following RT and TAS-116 treatment.

Sequencing of tumor-infiltrating lymphocytes in early-stage SCLC tumors unraveled a 'cold' TCR repertoire, meaning high TCR heterogeneity which was correlated with low overall survival¹⁹⁸. Interestingly, while this intratumoral heterogeneity was not correlated with clonal neoantigen burden in SCLC, another study found that early-stage LUAD with high neoantigen burden displayed greater homogeneity than samples with a low burden and that this resulted in better overall survival as well as an improved response to pembrolizumab treatment¹⁹⁹. In accordance, genomic intratumoral heterogeneity of LUAD was shown to result in higher TCR heterogeneity and increased relapse risk²⁰⁰. On the other hand, TCR clonality depends on the number of genomic mutations that are unique to the tumor as well, and this seems to correlate with PD-1 expression status. Moreover, T cell clonality was shown to be primarily driven by clonal expansion of CD8⁺ T cells²⁰¹. This is in line with the finding that most lymphocytes infiltrating NSCLC tumors that received neoadjuvant treatment with nivolumab are CD8⁺ T cells specific for neoantigens²⁰². In contrast, few neoantigen-specific infiltrating T cells were found in human lung and CRC tumors, and these exhibited a resident memory phenotype²⁰³.

When assessing the influence of TAS-116 on T cell-mediated effects, it must be considered that HSP90 inhibition has also been found to impede secretion of IL-2, expression of the IL-2 receptor as well as proliferation of stimulated T cells²⁰⁴. Additionally, processes involved in T cell priming, such as antigen processing, MHC-I peptide loading, and antigen presentation by APCs are likewise known to be dependent on functional HSP90²⁰⁵. These effects, however, are presumably less severe following administration of TAS-116, as it selectively inhibits the cytosolic isoforms HSP90 α and HSP90 β but not GRP94 in the endoplasmic reticulum which has been implicated in antigen loading onto MHC-I molecules²⁰⁶. Moreover, inhibition of HSP90 has been linked to downregulation of CD4 protein, co-stimulatory molecules, and $\alpha\beta$ receptors on T lymphocytes²⁰⁷.

Therefore, examining the TCR receptor status does not allow assessment of the induction of neoantigens alone. It could, however, be an elegant way to evaluate the overall treatment effects. The results of the TCR clonality analysis in this thesis suggest alterations in TCR clonality following RT and TAS-116 treatment but require further validation. In this regard, it would be of added value to repeat the in vivo experiments using Nur77^{GFP} reporter mice. In these transgenic mice, green fluorescent protein (GFP) is linked to expression of Nur77, a gene upregulated early following TCR activation. This way, it is possible to assess not only T cell clonality but also TCR signaling strength²⁰⁸.

6.6 Conclusion

Taken together, the hypothesis on which this work is based, i.e., RT and HSP90 inhibition enhance tumor immunogenicity via induction of IFN β and therefore render tumor cells more susceptible toward combined treatment with immune checkpoint blockade, could not be confirmed by the experiments conducted for this thesis. Previously published data as well as trends observed in the results herein suggest a synergistic potential of HSP90 inhibition and RT, nevertheless.

The fact that most of the results did not reach statistical significance may be explained by various shortcomings in the experimental designs. Moreover, HSP90 inhibition, by means of DDR inhibition, might not enhance cGAS/STING pathway activation as much as prolong it. It may therefore be of interest to monitor some of the pathway-dependent effects for a period of time using the dosing regimens that displayed a tendency to elicit a response herein. The experimental setups established for this work should therefore be further expanded to explore possible cell line-specific differences regarding preservation of DNA damage with subsequent prolonged cGAS/STING pathway signaling.

Additionally, ultimate effects in terms of tumor immunogenicity and enhanced susceptibility to immune checkpoint blockade should be examined further in in vivo treatment studies on various tumor entities.

7. Bibliography

1. Bray F, Laversanne M, Sung H, et al. Global cancer statistics 2022: GLOBOCAN estimates of incidence and mortality worldwide for 36 cancers in 185 countries. *CA Cancer J Clin* 2024; **74**(3): 229-63.
2. Hanahan D, Weinberg Robert A. Hallmarks of Cancer: The Next Generation. *Cell* 2011; **144**(5): 646-74.
3. Hanahan D. Hallmarks of Cancer: New Dimensions. *Cancer Discov* 2022; **12**(1): 31-46.
4. Luzzatto L, Pandolfi PP. Causality and Chance in the Development of Cancer. *N Engl J Med* 2015; **373**(1): 84-8.
5. Kontomanolis EN, Koutras A, Syllaios A, et al. Role of Oncogenes and Tumor-suppressor Genes in Carcinogenesis: A Review. *Anticancer Res* 2020; **40**(11): 6009-15.
6. Davis A, Gao R, Navin N. Tumor evolution: Linear, branching, neutral or punctuated? *Biochim Biophys Acta Rev Cancer* 2017; **1867**(2): 151-61.
7. Dagogo-Jack I, Shaw AT. Tumour heterogeneity and resistance to cancer therapies. *Nat Rev Clin Oncol* 2018; **15**(2): 81-94.
8. Bade BC, Dela Cruz CS. Lung Cancer 2020: Epidemiology, Etiology, and Prevention. *Clin Chest Med* 2020; **41**(1): 1-24.
9. Salehi-Rad R, Li R, Paul MK, Dubinett SM, Liu B. The Biology of Lung Cancer: Development of More Effective Methods for Prevention, Diagnosis, and Treatment. *Clin Chest Med* 2020; **41**(1): 25-38.
10. Park KS, Liang MC, Raiser DM, et al. Characterization of the cell of origin for small cell lung cancer. *Cell Cycle* 2011; **10**(16): 2806-15.
11. George J, Lim JS, Jang SJ, et al. Comprehensive genomic profiles of small cell lung cancer. *Nature* 2015; **524**(7563): 47-53.
12. Thai AA, Solomon BJ, Sequist LV, Gainor JF, Heist RS. Lung cancer. *Lancet* 2021; **398**(10299): 535-54.
13. Siegel RL, Miller KD, Fuchs HE, Jemal A. Cancer Statistics, 2021. *CA Cancer J Clin* 2021; **71**(1): 7-33.
14. Rudin CM, Brambilla E, Faivre-Finn C, Sage J. Small-cell lung cancer. *Nat Rev Dis Primers* 2021; **7**(1): 3.
15. Liu SV, Reck M, Mansfield AS, et al. Updated Overall Survival and PD-L1 Subgroup Analysis of Patients With Extensive-Stage Small-Cell Lung Cancer Treated With Atezolizumab, Carboplatin, and Etoposide (IMpower133). *J Clin Oncol* 2021; **39**(6): 619-30.
16. Paz-Ares L, Dvorkin M, Chen Y, et al. Durvalumab plus platinum-etoposide versus platinum-etoposide in first-line treatment of extensive-stage small-cell lung cancer (CASPIAN): a randomised, controlled, open-label, phase 3 trial. *Lancet* 2019; **394**(10212): 1929-39.

17. Herbst RS, Morgensztern D, Boshoff C. The biology and management of non-small cell lung cancer. *Nature* 2018; **553**(7689): 446-54.
18. Pignon JP, Tribodet H, Scagliotti GV, et al. Lung adjuvant cisplatin evaluation: a pooled analysis by the LACE Collaborative Group. *J Clin Oncol* 2008; **26**(21): 3552-9.
19. Forde PM, Spicer J, Lu S, et al. Neoadjuvant Nivolumab plus Chemotherapy in Resectable Lung Cancer. *N Engl J Med* 2022; **386**(21): 1973-85.
20. Myall NJ, Das M. Advances in the Treatment of Stage III Non-Small Cell Lung Cancer. *Clin Chest Med* 2020; **41**(2): 211-22.
21. Curran WJ, Jr., Paulus R, Langer CJ, et al. Sequential vs. concurrent chemoradiation for stage III non-small cell lung cancer: randomized phase III trial RTOG 9410. *J Natl Cancer Inst* 2011; **103**(19): 1452-60.
22. Spigel DR, Faivre-Finn C, Gray JE, et al. Five-Year Survival Outcomes From the PACIFIC Trial: Durvalumab After Chemoradiotherapy in Stage III Non-Small-Cell Lung Cancer. *J Clin Oncol* 2022; **40**(12): 1301-11.
23. Duma N, Santana-Davila R, Molina JR. Non-Small Cell Lung Cancer: Epidemiology, Screening, Diagnosis, and Treatment. *Mayo Clin Proc* 2019; **94**(8): 1623-40.
24. Lee CK, Wu YL, Ding PN, et al. Impact of Specific Epidermal Growth Factor Receptor (EGFR) Mutations and Clinical Characteristics on Outcomes After Treatment With EGFR Tyrosine Kinase Inhibitors Versus Chemotherapy in EGFR-Mutant Lung Cancer: A Meta-Analysis. *J Clin Oncol* 2015; **33**(17): 1958-65.
25. Jänne PA, Yang JC, Kim DW, et al. AZD9291 in EGFR inhibitor-resistant non-small-cell lung cancer. *N Engl J Med* 2015; **372**(18): 1689-99.
26. Reck M, Rodríguez-Abreu D, Robinson AG, et al. Pembrolizumab versus Chemotherapy for PD-L1-Positive Non-Small-Cell Lung Cancer. *N Engl J Med* 2016; **375**(19): 1823-33.
27. Gandhi L, Rodríguez-Abreu D, Gadgeel S, et al. Pembrolizumab plus Chemotherapy in Metastatic Non-Small-Cell Lung Cancer. *N Engl J Med* 2018; **378**(22): 2078-92.
28. Theelen W, Peulen HMU, Lalezari F, et al. Effect of Pembrolizumab After Stereotactic Body Radiotherapy vs Pembrolizumab Alone on Tumor Response in Patients With Advanced Non-Small Cell Lung Cancer: Results of the PEMBRO-RT Phase 2 Randomized Clinical Trial. *JAMA Oncol* 2019; **5**(9): 1276-82.
29. Siegel RL, Wagle NS, Cercek A, Smith RA, Jemal A. Colorectal cancer statistics, 2023. *CA Cancer J Clin* 2023; **73**(3): 233-54.
30. Siegel RL, Miller KD, Goding Sauer A, et al. Colorectal cancer statistics, 2020. *CA Cancer J Clin* 2020; **70**(3): 145-64.
31. Islami F, Goding Sauer A, Miller KD, et al. Proportion and number of cancer cases and deaths attributable to potentially modifiable risk factors in the United States. *CA Cancer J Clin* 2018; **68**(1): 31-54.
32. Leslie A, Carey FA, Pratt NR, Steele RJ. The colorectal adenoma-carcinoma sequence. *Br J Surg* 2002; **89**(7): 845-60.

33. Kloor M, Staffa L, Ahadova A, von Knebel Doeberitz M. Clinical significance of microsatellite instability in colorectal cancer. *Langenbecks Arch Surg* 2014; **399**(1): 23-31.
34. Dolcetti R, Viel A, Doglioni C, et al. High prevalence of activated intraepithelial cytotoxic T lymphocytes and increased neoplastic cell apoptosis in colorectal carcinomas with microsatellite instability. *Am J Pathol* 1999; **154**(6): 1805-13.
35. Popat S, Hubner R, Houlston RS. Systematic review of microsatellite instability and colorectal cancer prognosis. *J Clin Oncol* 2005; **23**(3): 609-18.
36. Guinney J, Dienstmann R, Wang X, et al. The consensus molecular subtypes of colorectal cancer. *Nat Med* 2015; **21**(11): 1350-6.
37. Rebersek M. Consensus molecular subtypes (CMS) in metastatic colorectal cancer - personalized medicine decision. *Radiol Oncol* 2020; **54**(3): 272-7.
38. Ribic CM, Sargent DJ, Moore MJ, et al. Tumor microsatellite-instability status as a predictor of benefit from fluorouracil-based adjuvant chemotherapy for colon cancer. *N Engl J Med* 2003; **349**(3): 247-57.
39. Amado RG, Wolf M, Peeters M, et al. Wild-type KRAS is required for panitumumab efficacy in patients with metastatic colorectal cancer. *J Clin Oncol* 2008; **26**(10): 1626-34.
40. Le DT, Uram JN, Wang H, et al. PD-1 Blockade in Tumors with Mismatch-Repair Deficiency. *N Engl J Med* 2015; **372**(26): 2509-20.
41. Overman MJ, McDermott R, Leach JL, et al. Nivolumab in patients with metastatic DNA mismatch repair-deficient or microsatellite instability-high colorectal cancer (CheckMate 142): an open-label, multicentre, phase 2 study. *Lancet Oncol* 2017; **18**(9): 1182-91.
42. Lenz HJ, Van Cutsem E, Luisa Limon M, et al. First-Line Nivolumab Plus Low-Dose Ipilimumab for Microsatellite Instability-High/Mismatch Repair-Deficient Metastatic Colorectal Cancer: The Phase II CheckMate 142 Study. *J Clin Oncol* 2022; **40**(2): 161-70.
43. McComb S, Thiriot A, Akache B, Krishnan L, Stark F. Introduction to the Immune System. *Methods Mol Biol* 2019; **2024**: 1-24.
44. Parkin J, Cohen B. An overview of the immune system. *Lancet* 2001; **357**(9270): 1777-89.
45. Togashi Y, Shitara K, Nishikawa H. Regulatory T cells in cancer immunosuppression - implications for anticancer therapy. *Nat Rev Clin Oncol* 2019; **16**(6): 356-71.
46. Blankenstein T, Coulie PG, Gilboa E, Jaffee EM. The determinants of tumour immunogenicity. *Nat Rev Cancer* 2012; **12**(4): 307-13.
47. Ehrlich P. Über den jetzigen Stand der Karzinomforschung. *Beiträge zur experimentellen Pathologie und Chemotherapie* 1909: 117-64.
48. Dunn GP, Bruce AT, Ikeda H, Old LJ, Schreiber RD. Cancer immunoediting: from immunosurveillance to tumor escape. *Nat Immunol* 2002; **3**(11): 991-8.

49. Girardi M, Oppenheim DE, Steele CR, et al. Regulation of cutaneous malignancy by gammadelta T cells. *Science* 2001; **294**(5542): 605-9.
50. Smyth MJ, Thia KY, Street SE, et al. Differential tumor surveillance by natural killer (NK) and NKT cells. *J Exp Med* 2000; **191**(4): 661-8.
51. Chen DS, Mellman I. Oncology meets immunology: the cancer-immunity cycle. *Immunity* 2013; **39**(1): 1-10.
52. Yarchoan M, Johnson BA, 3rd, Lutz ER, Laheru DA, Jaffee EM. Targeting neoantigens to augment antitumour immunity. *Nat Rev Cancer* 2017; **17**(4): 209-22.
53. Aguirre-Ghiso JA. Models, mechanisms and clinical evidence for cancer dormancy. *Nat Rev Cancer* 2007; **7**(11): 834-46.
54. Khong HT, Restifo NP. Natural selection of tumor variants in the generation of "tumor escape" phenotypes. *Nat Immunol* 2002; **3**(11): 999-1005.
55. Schreiber H, Wu TH, Nachman J, Kast WM. Immunodominance and tumor escape. *Semin Cancer Biol* 2002; **12**(1): 25-31.
56. Nihans GA, Brunner T, Frizelle SP, et al. Human lung carcinomas express Fas ligand. *Cancer Res* 1997; **57**(6): 1007-12.
57. Hahne M, Rimoldi D, Schröter M, et al. Melanoma cell expression of Fas(Apo-1/CD95) ligand: implications for tumor immune escape. *Science* 1996; **274**(5291): 1363-6.
58. O'Connell J, O'Sullivan GC, Collins JK, Shanahan F. The Fas counterattack: Fas-mediated T cell killing by colon cancer cells expressing Fas ligand. *J Exp Med* 1996; **184**(3): 1075-82.
59. Topalian SL, Drake CG, Pardoll DM. Immune checkpoint blockade: a common denominator approach to cancer therapy. *Cancer Cell* 2015; **27**(4): 450-61.
60. Hodi FS, O'Day SJ, McDermott DF, et al. Improved survival with ipilimumab in patients with metastatic melanoma. *N Engl J Med* 2010; **363**(8): 711-23.
61. Lenschow DJ, Walunas TL, Bluestone JA. CD28/B7 system of T cell costimulation. *Annu Rev Immunol* 1996; **14**: 233-58.
62. Linsley PS, Greene JL, Brady W, Bajorath J, Ledbetter JA, Peach R. Human B7-1 (CD80) and B7-2 (CD86) bind with similar avidities but distinct kinetics to CD28 and CTLA-4 receptors. *Immunity* 1994; **1**(9): 793-801.
63. Rudd CE, Taylor A, Schneider H. CD28 and CTLA-4 coreceptor expression and signal transduction. *Immunol Rev* 2009; **229**(1): 12-26.
64. Qureshi OS, Zheng Y, Nakamura K, et al. Trans-endocytosis of CD80 and CD86: a molecular basis for the cell-extrinsic function of CTLA-4. *Science* 2011; **332**(6029): 600-3.
65. Keir ME, Butte MJ, Freeman GJ, Sharpe AH. PD-1 and its ligands in tolerance and immunity. *Annu Rev Immunol* 2008; **26**: 677-704.
66. Freeman GJ, Long AJ, Iwai Y, et al. Engagement of the PD-1 immunoinhibitory receptor by a novel B7 family member leads to negative regulation of lymphocyte activation. *J Exp Med* 2000; **192**(7): 1027-34.

67. Chaudhri A, Xiao Y, Klee AN, Wang X, Zhu B, Freeman GJ. PD-L1 Binds to B7-1 Only In Cis on the Same Cell Surface. *Cancer Immunol Res* 2018; **6**(8): 921-9.
68. Mayoux M, Roller A, Pulko V, et al. Dendritic cells dictate responses to PD-L1 blockade cancer immunotherapy. *Sci Transl Med* 2020; **12**(534).
69. Sun C, Mezzadra R, Schumacher TN. Regulation and Function of the PD-L1 Checkpoint. *Immunity* 2018; **48**(3): 434-52.
70. Borghaei H, Paz-Ares L, Horn L, et al. Nivolumab versus Docetaxel in Advanced Nonsquamous Non-Small-Cell Lung Cancer. *N Engl J Med* 2015; **373**(17): 1627-39.
71. Brahmer J, Reckamp KL, Baas P, et al. Nivolumab versus Docetaxel in Advanced Squamous-Cell Non-Small-Cell Lung Cancer. *N Engl J Med* 2015; **373**(2): 123-35.
72. Ritterhouse LL. Tumor mutational burden. *Cancer Cytopathol* 2019; **127**(12): 735-6.
73. Snyder A, Makarov V, Merghoub T, et al. Genetic basis for clinical response to CTLA-4 blockade in melanoma. *N Engl J Med* 2014; **371**(23): 2189-99.
74. Rizvi NA, Hellmann MD, Snyder A, et al. Cancer immunology. Mutational landscape determines sensitivity to PD-1 blockade in non-small cell lung cancer. *Science* 2015; **348**(6230): 124-8.
75. Baskar R, Lee KA, Yeo R, Yeoh KW. Cancer and radiation therapy: current advances and future directions. *Int J Med Sci* 2012; **9**(3): 193-9.
76. Bionda C, Hadchity E, Alphonse G, et al. Radioresistance of human carcinoma cells is correlated to a defect in raft membrane clustering. *Free Radic Biol Med* 2007; **43**(5): 681-94.
77. Tang L, Wei F, Wu Y, et al. Role of metabolism in cancer cell radioresistance and radiosensitization methods. *J Exp Clin Cancer Res* 2018; **37**(1): 87.
78. Frey B, Rückert M, Deloch L, et al. Immunomodulation by ionizing radiation-impact for design of radio-immunotherapies and for treatment of inflammatory diseases. *Immunol Rev* 2017; **280**(1): 231-48.
79. Douki T, Ravanat JL, Pouget JP, Testard I, Cadet J. Minor contribution of direct ionization to DNA base damage induced by heavy ions. *Int J Radiat Biol* 2006; **82**(2): 119-27.
80. Corre I, Niaudet C, Paris F. Plasma membrane signaling induced by ionizing radiation. *Mutat Res* 2010; **704**(1-3): 61-7.
81. Hall EJ, Hei TK. Genomic instability and bystander effects induced by high-LET radiation. *Oncogene* 2003; **22**(45): 7034-42.
82. Koyama S, Kodama S, Suzuki K, Matsumoto T, Miyazaki T, Watanabe M. Radiation-induced long-lived radicals which cause mutation and transformation. *Mutat Res* 1998; **421**(1): 45-54.
83. Baskar R, Balajee AS, Geard CR. Effects of low and high LET radiations on bystander human lung fibroblast cell survival. *Int J Radiat Biol* 2007; **83**(8): 551-9.

84. Azzam EI, de Toledo SM, Little JB. Direct evidence for the participation of gap junction-mediated intercellular communication in the transmission of damage signals from alpha-particle irradiated to nonirradiated cells. *Proc Natl Acad Sci U S A* 2001; **98**(2): 473-8.
85. Najafi M, Fardid R, Hadadi G, Fardid M. The mechanisms of radiation-induced bystander effect. *J Biomed Phys Eng* 2014; **4**(4): 163-72.
86. Verheij M. Clinical biomarkers and imaging for radiotherapy-induced cell death. *Cancer Metastasis Rev* 2008; **27**(3): 471-80.
87. Eriksson D, Stigbrand T. Radiation-induced cell death mechanisms. *Tumour Biol* 2010; **31**(4): 363-72.
88. Jiang X, Wang X. Cytochrome c promotes caspase-9 activation by inducing nucleotide binding to Apaf-1. *J Biol Chem* 2000; **275**(40): 31199-203.
89. Roninson IB, Broude EV, Chang BD. If not apoptosis, then what? Treatment-induced senescence and mitotic catastrophe in tumor cells. *Drug Resist Updat* 2001; **4**(5): 303-13.
90. Ianzini F, Mackey MA. Spontaneous premature chromosome condensation and mitotic catastrophe following irradiation of HeLa S3 cells. *Int J Radiat Biol* 1997; **72**(4): 409-21.
91. Schosserer M, Grillari J, Breitenbach M. The Dual Role of Cellular Senescence in Developing Tumors and Their Response to Cancer Therapy. *Front Oncol* 2017; **7**: 278.
92. Demaria M, O'Leary MN, Chang J, et al. Cellular Senescence Promotes Adverse Effects of Chemotherapy and Cancer Relapse. *Cancer Discov* 2017; **7**(2): 165-76.
93. Reits EA, Hodge JW, Herberts CA, et al. Radiation modulates the peptide repertoire, enhances MHC class I expression, and induces successful antitumor immunotherapy. *J Exp Med* 2006; **203**(5): 1259-71.
94. Golden EB, Frances D, Pellicciotta I, Demaria S, Helen Barcellos-Hoff M, Formenti SC. Radiation fosters dose-dependent and chemotherapy-induced immunogenic cell death. *Oncoimmunology* 2014; **3**: e28518.
95. Lam AR, Bert NL, Ho SS, et al. RAE1 ligands for the NKG2D receptor are regulated by STING-dependent DNA sensor pathways in lymphoma. *Cancer Res* 2014; **74**(8): 2193-203.
96. Klug F, Prakash H, Huber PE, et al. Low-dose irradiation programs macrophage differentiation to an iNOS⁺/M1 phenotype that orchestrates effective T cell immunotherapy. *Cancer Cell* 2013; **24**(5): 589-602.
97. Filatenkov A, Baker J, Mueller AM, et al. Ablative Tumor Radiation Can Change the Tumor Immune Cell Microenvironment to Induce Durable Complete Remissions. *Clin Cancer Res* 2015; **21**(16): 3727-39.
98. Rabinovich GA, Gabrilovich D, Sotomayor EM. Immunosuppressive strategies that are mediated by tumor cells. *Annu Rev Immunol* 2007; **25**: 267-96.
99. Lee Y, Auh SL, Wang Y, et al. Therapeutic effects of ablative radiation on local tumor require CD8⁺ T cells: changing strategies for cancer treatment. *Blood* 2009; **114**(3): 589-95.

100. Chen Q, Sun L, Chen ZJ. Regulation and function of the cGAS-STING pathway of cytosolic DNA sensing. *Nat Immunol* 2016; **17**(10): 1142-9.
101. Vanpouille-Box C, Alard A, Aryankalayil MJ, et al. DNA exonuclease Trex1 regulates radiotherapy-induced tumour immunogenicity. *Nat Commun* 2017; **8**: 15618.
102. Burnette BC, Liang H, Lee Y, et al. The efficacy of radiotherapy relies upon induction of type I interferon-dependent innate and adaptive immunity. *Cancer Res* 2011; **71**(7): 2488-96.
103. Ishikawa H, Barber GN. STING is an endoplasmic reticulum adaptor that facilitates innate immune signalling. *Nature* 2008; **455**(7213): 674-8.
104. Ishikawa H, Ma Z, Barber GN. STING regulates intracellular DNA-mediated, type I interferon-dependent innate immunity. *Nature* 2009; **461**(7265): 788-92.
105. Sun L, Wu J, Du F, Chen X, Chen ZJ. Cyclic GMP-AMP synthase is a cytosolic DNA sensor that activates the type I interferon pathway. *Science* 2013; **339**(6121): 786-91.
106. Wu J, Sun L, Chen X, et al. Cyclic GMP-AMP is an endogenous second messenger in innate immune signaling by cytosolic DNA. *Science* 2013; **339**(6121): 826-30.
107. Ablasser A, Schmid-Burgk JL, Hemmerling I, et al. Cell intrinsic immunity spreads to bystander cells via the intercellular transfer of cGAMP. *Nature* 2013; **503**(7477): 530-4.
108. Ergun SL, Fernandez D, Weiss TM, Li L. STING Polymer Structure Reveals Mechanisms for Activation, Hyperactivation, and Inhibition. *Cell* 2019; **178**(2): 290-301.e10.
109. Zhang C, Shang G, Gui X, Zhang X, Bai XC, Chen ZJ. Structural basis of STING binding with and phosphorylation by TBK1. *Nature* 2019; **567**(7748): 394-8.
110. Tanaka Y, Chen ZJ. STING specifies IRF3 phosphorylation by TBK1 in the cytosolic DNA signaling pathway. *Sci Signal* 2012; **5**(214): ra20.
111. Honda K, Takaoka A, Taniguchi T. Type I interferon [corrected] gene induction by the interferon regulatory factor family of transcription factors. *Immunity* 2006; **25**(3): 349-60.
112. Konno H, Konno K, Barber GN. Cyclic dinucleotides trigger ULK1 (ATG1) phosphorylation of STING to prevent sustained innate immune signaling. *Cell* 2013; **155**(3): 688-98.
113. Deng Y, Wang Y, Li L, Miao EA, Liu P. Post-Translational Modifications of Proteins in Cytosolic Nucleic Acid Sensing Signaling Pathways. *Front Immunol* 2022; **13**: 898724.
114. Harding SM, Benci JL, Irianto J, Discher DE, Minn AJ, Greenberg RA. Mitotic progression following DNA damage enables pattern recognition within micronuclei. *Nature* 2017; **548**(7668): 466-70.
115. Ghosh M, Saha S, Bettke J, et al. Mutant p53 suppresses innate immune signaling to promote tumorigenesis. *Cancer Cell* 2021; **39**(4): 494-508.e5.

116. Ghosh M, Saha S, Li J, Montrose DC, Martinez LA. p53 engages the cGAS/STING cytosolic DNA sensing pathway for tumor suppression. *Mol Cell* 2023; **83**(2): 266-80.e6.
117. Sen T, Rodriguez BL, Chen L, et al. Targeting DNA Damage Response Promotes Antitumor Immunity through STING-Mediated T-cell Activation in Small Cell Lung Cancer. *Cancer Discov* 2019; **9**(5): 646-61.
118. Miyata Y, Nakamoto H, Neckers L. The therapeutic target Hsp90 and cancer hallmarks. *Curr Pharm Des* 2013; **19**(3): 347-65.
119. Buchberger A, Bukau B, Sommer T. Protein quality control in the cytosol and the endoplasmic reticulum: brothers in arms. *Mol Cell* 2010; **40**(2): 238-52.
120. Dayalan Naidu S, Dinkova-Kostova AT. Regulation of the mammalian heat shock factor 1. *Febs j* 2017; **284**(11): 1606-27.
121. Richter K, Haslbeck M, Buchner J. The heat shock response: life on the verge of death. *Mol Cell* 2010; **40**(2): 253-66.
122. Mendillo ML, Santagata S, Koeva M, et al. HSF1 drives a transcriptional program distinct from heat shock to support highly malignant human cancers. *Cell* 2012; **150**(3): 549-62.
123. Scherz-Shouval R, Santagata S, Mendillo ML, et al. The reprogramming of tumor stroma by HSF1 is a potent enabler of malignancy. *Cell* 2014; **158**(3): 564-78.
124. Schopf FH, Biebl MM, Buchner J. The HSP90 chaperone machinery. *Nat Rev Mol Cell Biol* 2017; **18**(6): 345-60.
125. Nathan DF, Vos MH, Lindquist S. In vivo functions of the *Saccharomyces cerevisiae* Hsp90 chaperone. *Proc Natl Acad Sci U S A* 1997; **94**(24): 12949-56.
126. Panaretou B, Prodromou C, Roe SM, et al. ATP binding and hydrolysis are essential to the function of the Hsp90 molecular chaperone in vivo. *Embo j* 1998; **17**(16): 4829-36.
127. Mayer MP. Gymnastics of molecular chaperones. *Mol Cell* 2010; **39**(3): 321-31.
128. Birbo B, Madu EE, Madu CO, Jain A, Lu Y. Role of HSP90 in Cancer. *Int J Mol Sci* 2021; **22**(19).
129. Tokuriki N, Stricher F, Serrano L, Tawfik DS. How protein stability and new functions trade off. *PLoS Comput Biol* 2008; **4**(2): e1000002.
130. McCready J, Sims JD, Chan D, Jay DG. Secretion of extracellular hsp90alpha via exosomes increases cancer cell motility: a role for plasminogen activation. *BMC Cancer* 2010; **10**: 294.
131. Song X, Wang X, Zhuo W, et al. The regulatory mechanism of extracellular Hsp90{alpha} on matrix metalloproteinase-2 processing and tumor angiogenesis. *J Biol Chem* 2010; **285**(51): 40039-49.
132. Ullrich SJ, Robinson EA, Law LW, Willingham M, Appella E. A mouse tumor-specific transplantation antigen is a heat shock-related protein. *Proc Natl Acad Sci U S A* 1986; **83**(10): 3121-5.

133. Zhao R, Davey M, Hsu YC, et al. Navigating the chaperone network: an integrative map of physical and genetic interactions mediated by the hsp90 chaperone. *Cell* 2005; **120**(5): 715-27.
134. Taipale M, Jarosz DF, Lindquist S. HSP90 at the hub of protein homeostasis: emerging mechanistic insights. *Nat Rev Mol Cell Biol* 2010; **11**(7): 515-28.
135. Dubrez L, Causse S, Borges Bonan N, Dumétier B, Garrido C. Heat-shock proteins: chaperoning DNA repair. *Oncogene* 2020; **39**(3): 516-29.
136. Gallegos Ruiz MI, Floor K, Roepman P, et al. Integration of gene dosage and gene expression in non-small cell lung cancer, identification of HSP90 as potential target. *PLoS One* 2008; **3**(3): e0001722.
137. Johnson ML, Yu HA, Hart EM, et al. Phase I/II Study of HSP90 Inhibitor AUY922 and Erlotinib for EGFR-Mutant Lung Cancer With Acquired Resistance to Epidermal Growth Factor Receptor Tyrosine Kinase Inhibitors. *J Clin Oncol* 2015; **33**(15): 1666-73.
138. Seggewiss-Bernhardt R, Bargou RC, Goh YT, et al. Phase 1/1B trial of the heat shock protein 90 inhibitor NVP-AUY922 as monotherapy or in combination with bortezomib in patients with relapsed or refractory multiple myeloma. *Cancer* 2015; **121**(13): 2185-92.
139. Kryeziu K, Bruun J, Guren TK, Sveen A, Lothe RA. Combination therapies with HSP90 inhibitors against colorectal cancer. *Biochim Biophys Acta Rev Cancer* 2019; **1871**(2): 240-7.
140. Garcia-Carbonero R, Carnero A, Paz-Ares L. Inhibition of HSP90 molecular chaperones: moving into the clinic. *Lancet Oncol* 2013; **14**(9): e358-69.
141. Ohkubo S, Kodama Y, Muraoka H, et al. TAS-116, a highly selective inhibitor of heat shock protein 90 α and β , demonstrates potent antitumor activity and minimal ocular toxicity in preclinical models. *Mol Cancer Ther* 2015; **14**(1): 14-22.
142. Shimomura A, Yamamoto N, Kondo S, et al. First-in-Human Phase I Study of an Oral HSP90 Inhibitor, TAS-116, in Patients with Advanced Solid Tumors. *Mol Cancer Ther* 2019; **18**(3): 531-40.
143. Doi T, Kurokawa Y, Sawaki A, et al. Efficacy and safety of TAS-116, an oral inhibitor of heat shock protein 90, in patients with metastatic or unresectable gastrointestinal stromal tumour refractory to imatinib, sunitinib and regorafenib: a phase II, single-arm trial. *Eur J Cancer* 2019; **121**: 29-39.
144. Demetri GD, Heinrich MC, Chmielowski B, et al. An open-label phase II study of the Hsp90 inhibitor ganetespib (STA-9090) in patients (pts) with metastatic and/or unresectable GIST. *Journal of Clinical Oncology* 2011; **29**(15_suppl): 10011-.
145. Bendell JC, Bauer TM, Lamar R, et al. A Phase 2 Study of the Hsp90 Inhibitor AUY922 as Treatment for Patients with Refractory Gastrointestinal Stromal Tumors. *Cancer Invest* 2016; **34**(6): 265-70.
146. Kurokawa Y, Honma Y, Sawaki A, et al. Pimipespib in patients with advanced gastrointestinal stromal tumor (CHAPTER-GIST-301): a randomized, double-blind, placebo-controlled phase III trial. *Ann Oncol* 2022; **33**(9): 959-67.
147. Hoy SM. Pimipespib: First Approval. *Drugs* 2022.

148. Teranishi R, Takahashi T, Obata Y, et al. Combination of pimitespib (TAS-116) with sunitinib is an effective therapy for imatinib-resistant gastrointestinal stromal tumors. *Int J Cancer* 2023; **152**(12): 2580-93.
149. Kawazoe A, Itahashi K, Yamamoto N, et al. TAS-116 (Pimitespib), an Oral HSP90 Inhibitor, in Combination with Nivolumab in Patients with Colorectal Cancer and Other Solid Tumors: An Open-Label, Dose-Finding, and Expansion Phase Ib Trial (EPOC1704). *Clin Cancer Res* 2021; **27**(24): 6709-15.
150. Takei S, Tanaka Y, Lin YT, et al. Multiomic molecular characterization of the response to combination immunotherapy in MSS/pMMR metastatic colorectal cancer. *J Immunother Cancer* 2024; **12**(2).
151. Gong J, Wang C, Lee PP, Chu P, Fakhri M. Response to PD-1 Blockade in Microsatellite Stable Metastatic Colorectal Cancer Harboring a POLE Mutation. *J Natl Compr Canc Netw* 2017; **15**(2): 142-7.
152. Taiho Pharmaceutical Co. L. A Study of Pimitespib in Combination With Imatinib in Patients With GIST (CHAPTER-GIST-101). ClinicalTrials.gov identifier: NCT05245968. Updated 2024.08.07. <https://ClinicalTrials.gov/show/NCT05245968> (accessed 2024.10.08).
153. Bai R, Chen N, Li L, et al. Mechanisms of Cancer Resistance to Immunotherapy. *Front Oncol* 2020; **10**: 1290.
154. Vanpouille-Box C, Demaria S, Formenti SC, Galluzzi L. Cytosolic DNA Sensing in Organismal Tumor Control. *Cancer Cell* 2018; **34**(3): 361-78.
155. Kabakov AE, Kudryavtsev VA, Gabai VL. Hsp90 inhibitors as promising agents for radiotherapy. *J Mol Med (Berl)* 2010; **88**(3): 241-7.
156. Melnikova VO, Bolshakov SV, Walker C, Ananthaswamy HN. Genomic alterations in spontaneous and carcinogen-induced murine melanoma cell lines. *Oncogene* 2004; **23**(13): 2347-56.
157. Moore MW, Carbone FR, Bevan MJ. Introduction of soluble protein into the class I pathway of antigen processing and presentation. *Cell* 1988; **54**(6): 777-85.
158. Hogquist KA, Jameson SC, Heath WR, Howard JL, Bevan MJ, Carbone FR. T cell receptor antagonist peptides induce positive selection. *Cell* 1994; **76**(1): 17-27.
159. Clarke SR, Barnden M, Kurts C, Carbone FR, Miller JF, Heath WR. Characterization of the ovalbumin-specific TCR transgenic line OT-I: MHC elements for positive and negative selection. *Immunol Cell Biol* 2000; **78**(2): 110-7.
160. Philpott NJ, Turner AJ, Scopes J, et al. The use of 7-amino actinomycin D in identifying apoptosis: simplicity of use and broad spectrum of application compared with other techniques. *Blood* 1996; **87**(6): 2244-51.
161. Rieger AM, Nelson KL, Konowalchuk JD, Barreda DR. Modified annexin V/propidium iodide apoptosis assay for accurate assessment of cell death. *J Vis Exp* 2011; (50).
162. Chazotte B. Labeling nuclear DNA with hoechst 33342. *Cold Spring Harb Protoc* 2011; **2011**(1): pdb.prot5557.

163. Sharma A, Singh K, Almasan A. Histone H2AX phosphorylation: a marker for DNA damage. *Methods Mol Biol* 2012; **2012**;920:613-26.
164. Jesenko T, Bosnjak M, Markelc B, et al. Radiation Induced Upregulation of DNA Sensing Pathways is Cell-Type Dependent and Can Mediate the Off-Target Effects. *Cancers (Basel)* 2020; **12**(11).
165. Krutzik PO, Nolan GP. Intracellular phospho-protein staining techniques for flow cytometry: monitoring single cell signaling events. *Cytometry A* 2003; **55**(2): 61-70.
166. Yang K, Shi H, Qi R, et al. Hsp90 regulates activation of interferon regulatory factor 3 and TBK-1 stabilization in Sendai virus-infected cells. *Mol Biol Cell* 2006; **17**(3): 1461-71.
167. Bai J, Liu F. The cGAS-cGAMP-STING Pathway: A Molecular Link Between Immunity and Metabolism. *Diabetes* 2019; **68**(6): 1099-108.
168. Barnes S, Franklin M. MC38: An immunoresponsive murine tumor model. 2019. <https://oncology.labcorp.com/mc38-immunoresponsive-murine-tumor-model> (accessed 2024.10.08).
169. Herter-Sprie GS, Korideck H, Christensen CL, et al. Image-guided radiotherapy platform using single nodule conditional lung cancer mouse models. *Nat Commun* 2014; **5**: 5870.
170. Lee Y, Sunada S, Hirakawa H, Fujimori A, Nickoloff JA, Okayasu R. TAS-116, a Novel Hsp90 Inhibitor, Selectively Enhances Radiosensitivity of Human Cancer Cells to X-rays and Carbon Ion Radiation. *Mol Cancer Ther* 2017; **16**(1): 16-24.
171. Pawlik TM, Keyomarsi K. Role of cell cycle in mediating sensitivity to radiotherapy. *Int J Radiat Oncol Biol Phys* 2004; **59**(4): 928-42.
172. Sedelnikova OA, Rogakou EP, Panyutin IG, Bonner WM. Quantitative detection of (125)IdU-induced DNA double-strand breaks with gamma-H2AX antibody. *Radiat Res* 2002; **158**(4): 486-92.
173. Bouquet F, Muller C, Salles B. The loss of gammaH2AX signal is a marker of DNA double strand breaks repair only at low levels of DNA damage. *Cell Cycle* 2006; **5**(10): 1116-22.
174. Mukherjee B, Kessinger C, Kobayashi J, et al. DNA-PK phosphorylates histone H2AX during apoptotic DNA fragmentation in mammalian cells. *DNA Repair (Amst)* 2006; **5**(5): 575-90.
175. Pennisi R, Antocchia A, Leone S, Ascenzi P, di Masi A. Hsp90 α regulates ATM and NBN functions in sensing and repair of DNA double-strand breaks. *Febs j* 2017; **284**(15): 2378-95.
176. Elaimy AL, Ahsan A, Marsh K, et al. ATM is the primary kinase responsible for phosphorylation of Hsp90 α after ionizing radiation. *Oncotarget* 2016; **7**(50): 82450-7.
177. Quanz M, Herbette A, Sayarath M, et al. Heat shock protein 90 α (Hsp90 α) is phosphorylated in response to DNA damage and accumulates in repair foci. *J Biol Chem* 2012; **287**(12): 8803-15.

178. Solier S, Kohn KW, Scroggins B, et al. Heat shock protein 90 α (HSP90 α), a substrate and chaperone of DNA-PK necessary for the apoptotic response. *Proc Natl Acad Sci U S A* 2012; **109**(32): 12866-72.
179. Solier S, Pommier Y. The nuclear γ -H2AX apoptotic ring: implications for cancers and autoimmune diseases. *Cell Mol Life Sci* 2014; **71**(12): 2289-97.
180. Ernst A, Hennel R, Krombach J, et al. Priming of Anti-tumor Immune Mechanisms by Radiotherapy Is Augmented by Inhibition of Heat Shock Protein 90. *Front Oncol* 2020; **10**(1668).
181. Gurtner K, Kryzmien Z, Koi L, et al. Radioresistance of KRAS/TP53-mutated lung cancer can be overcome by radiation dose escalation or EGFR tyrosine kinase inhibition in vivo. *Int J Cancer* 2020; **147**(2): 472-7.
182. Mbofung RM, McKenzie JA, Malu S, et al. HSP90 inhibition enhances cancer immunotherapy by upregulating interferon response genes. *Nat Commun* 2017; **8**(1): 451.
183. Haggerty TJ, Dunn IS, Rose LB, Newton EE, Pandolfi F, Kurnick JT. Heat shock protein-90 inhibitors enhance antigen expression on melanomas and increase T cell recognition of tumor cells. *PLoS One* 2014; **9**(12): e114506.
184. Rao A, Taylor JL, Chi-Sabins N, Kawabe M, Gooding WE, Storkus WJ. Combination therapy with HSP90 inhibitor 17-DMAG reconditions the tumor microenvironment to improve recruitment of therapeutic T cells. *Cancer Res* 2012; **72**(13): 3196-206.
185. Callahan MK, Garg M, Srivastava PK. Heat-shock protein 90 associates with N-terminal extended peptides and is required for direct and indirect antigen presentation. *Proc Natl Acad Sci U S A* 2008; **105**(5): 1662-7.
186. Garnett CT, Palena C, Chakraborty M, Tsang K-Y, Schlom J, Hodge JW. Sublethal Irradiation of Human Tumor Cells Modulates Phenotype Resulting in Enhanced Killing by Cytotoxic T Lymphocytes. *Cancer Research* 2004; **64**(21): 7985-94.
187. Chakraborty M, Abrams SI, Camphausen K, et al. Irradiation of Tumor Cells Up-Regulates Fas and Enhances CTL Lytic Activity and CTL Adoptive Immunotherapy. *The Journal of Immunology* 2003; **170**(12): 6338-47.
188. Kumari A, Garnett-Benson C. Effector function of CTLs is increased by irradiated colorectal tumor cells that modulate OX-40L and 4-1BBL and is reversed following dual blockade. *BMC Res Notes* 2016; **9**: 92.
189. Kober J, Leitner J, Klausner C, et al. The capacity of the TNF family members 4-1BBL, OX40L, CD70, GITRL, CD30L and LIGHT to costimulate human T cells. *Eur J Immunol* 2008; **38**(10): 2678-88.
190. Zhang GB, Dong QM, Hou JQ, et al. Characterization and application of three novel monoclonal antibodies against human 4-1BB: distinct epitopes of human 4-1BB on lung tumor cells and immune cells. *Tissue Antigens* 2007; **70**(6): 470-9.
191. Niknam S, Barsoumian HB, Schoenhals JE, et al. Radiation Followed by OX40 Stimulation Drives Local and Abscopal Antitumor Effects in an Anti-PD1-Resistant Lung Tumor Model. *Clin Cancer Res* 2018; **24**(22): 5735-43.

192. Chen P, Wang H, Zhao L, et al. Immune Checkpoints OX40 and OX40L in Small-Cell Lung Cancer: Predict Prognosis and Modulate Immune Microenvironment. *Front Oncol* 2021; **11**: 713853.
193. Chen J, Cao Y, Markelc B, Kaeppler J, Vermeer JA, Muschel RJ. Type I IFN protects cancer cells from CD8+ T cell-mediated cytotoxicity after radiation. *J Clin Invest* 2019; **129**(10): 4224-38.
194. Hartmann L, Schröter P, Osen W, et al. Photon versus carbon ion irradiation: immunomodulatory effects exerted on murine tumor cell lines. *Scientific Reports* 2020; **10**(1): 21517.
195. Jiao S, Xia W, Yamaguchi H, et al. PARP Inhibitor Upregulates PD-L1 Expression and Enhances Cancer-Associated Immunosuppression. *Clin Cancer Res* 2017; **23**(14): 3711-20.
196. Iwai Y, Ishida M, Tanaka Y, Okazaki T, Honjo T, Minato N. Involvement of PD-L1 on tumor cells in the escape from host immune system and tumor immunotherapy by PD-L1 blockade. *Proc Natl Acad Sci U S A* 2002; **99**(19): 12293-7.
197. De Sousa Linares A, Battin C, Jutz S, et al. Therapeutic PD-L1 antibodies are more effective than PD-1 antibodies in blocking PD-1/PD-L1 signaling. *Sci Rep* 2019; **9**(1): 11472.
198. Chen M, Chen R, Jin Y, et al. Cold and heterogeneous T cell repertoire is associated with copy number aberrations and loss of immune genes in small-cell lung cancer. *Nat Commun* 2021; **12**(1): 6655.
199. McGranahan N, Furness AJ, Rosenthal R, et al. Clonal neoantigens elicit T cell immunoreactivity and sensitivity to immune checkpoint blockade. *Science* 2016; **351**(6280): 1463-9.
200. Reuben A, Gittelman R, Gao J, et al. TCR Repertoire Intratumor Heterogeneity in Localized Lung Adenocarcinomas: An Association with Predicted Neoantigen Heterogeneity and Postsurgical Recurrence. *Cancer Discov* 2017; **7**(10): 1088-97.
201. Reuben A, Zhang J, Chiou SH, et al. Comprehensive T cell repertoire characterization of non-small cell lung cancer. *Nat Commun* 2020; **11**(1): 603.
202. Caushi JX, Zhang J, Ji Z, et al. Transcriptional programs of neoantigen-specific TIL in anti-PD-1-treated lung cancers. *Nature* 2021; **596**(7870): 126-32.
203. Simoni Y, Becht E, Fehlings M, et al. Bystander CD8(+) T cells are abundant and phenotypically distinct in human tumour infiltrates. *Nature* 2018; **557**(7706): 575-9.
204. Schnaider T, Somogyi J, Csermely P, Szamel M. The Hsp90-specific inhibitor geldanamycin selectively disrupts kinase-mediated signaling events of T-lymphocyte activation. *Cell Stress Chaperones* 2000; **5**(1): 52-61.
205. Graner MW. HSP90 and Immune Modulation in Cancer. *Adv Cancer Res* 2016; **129**: 191-224.
206. Kropp LE, Garg M, Binder RJ. Ovalbumin-derived precursor peptides are transferred sequentially from gp96 and calreticulin to MHC class I in the endoplasmic reticulum. *J Immunol* 2010; **184**(10): 5619-27.

207. Bae J, Munshi A, Li C, et al. Heat shock protein 90 is critical for regulation of phenotype and functional activity of human T lymphocytes and NK cells. *J Immunol* 2013; **190**(3): 1360-71.
208. Moran AE, Holzapfel KL, Xing Y, et al. T cell receptor signal strength in Treg and iNKT cell development demonstrated by a novel fluorescent reporter mouse. *J Exp Med* 2011; **208**(6): 1279-89.

8. Appendix

8.1 List of figures

| | |
|--------------------------------------------------------------------------------------------|----|
| Figure 1: The hallmarks of cancer (D. Hanahan, 2022) ² | 12 |
| Figure 2: Common cells of the immune system (McComb et al., 2019) ⁴³ | 18 |
| Figure 3: The cancer-immunity cycle (D.S. Chen and Mellman, 2013) ⁵¹ | 19 |
| Figure 4. cGAS/STING pathway (Q. Chen et al., 2016) ¹⁰⁰ | 25 |
| Figure 5: DNA damage repair signaling pathways (Dubrez et al., 2020) | 28 |
| Figure 6: Flow cytometry panel for TCR staining | 44 |
| Figure 7: Cytotoxicity of TAS-116 | 47 |
| Figure 8: Cell viability following RT and TAS-116 treatment | 48 |
| Figure 9: Propidium Iodide staining of ACF135.10 cells..... | 50 |
| Figure 10: Propidium Iodide staining of RP157.8 cells..... | 51 |
| Figure 11: Propidium Iodide staining of MC38 cells | 52 |
| Figure 12: Propidium Iodide staining of B16F ₁₀ cells..... | 53 |
| Figure 13: DNA double-strand breaks following RT and TAS-116 treatment | 54 |
| Figure 14: Immunofluorescence staining for γ H2AX on ACF135.10 cells | 56 |
| Figure 15: Immunofluorescence staining for γ H2AX on RP157.8 cells | 57 |
| Figure 16: Immunofluorescence staining for γ H2AX on MC38 cells..... | 58 |
| Figure 17: cGAS/STING pathway activation by RT and TAS-116..... | 59 |
| Figure 18: dsDNA in the cytosol following RT and TAS-116 treatment | 61 |
| Figure 19: Immunofluorescence staining for dsDNA on ACF135.10 cells | 62 |
| Figure 20: Immunofluorescence staining for dsDNA on RP157.8 cells | 63 |
| Figure 21: Immunofluorescence staining for dsDNA on MC38 cells..... | 64 |
| Figure 22: STING phosphorylation following RT and TAS-116 treatment | 65 |
| Figure 23: Immunofluorescence staining for pSTING on ACF135.10 cells..... | 67 |
| Figure 24: Immunofluorescence staining for pSTING on RP157.8 cells..... | 68 |
| Figure 25: Immunofluorescence staining for pSTING on MC38 cells | 69 |
| Figure 26: IFN β induction following RT and TAS-116 treatment | 70 |
| Figure 27: Immunofluorescence staining for IFN β on ACF135.10 cells..... | 72 |
| Figure 28: Immunofluorescence staining for IFN β on RP157.8 cells..... | 73 |
| Figure 29: Immunofluorescence staining for IFN β on MC38 cells | 74 |
| Figure 30: CD8 ⁺ T cell-mediated killing at different timepoints after RT | 76 |
| Figure 31: CD8 ⁺ T cell-mediated killing of tumor cells..... | 77 |
| Figure 32: PD-L1 and PD-L2 expression following RT and TAS-116 treatment | 78 |
| Figure 33: T cell receptor expression..... | 80 |

9. Preliminary publications of results

Heßelmann, I., Reinscheid, M., Kiljan, M., Niu, L.-n., Cai, J., Wagner, E., Ibruli, O., Sahbaz, Y., Mayer, M., Kamp, F., Baues, C., Marnitz, S., Herter-Sprie, G. and Herter, J. Synergy of HSP90 Inhibition and Radiation Therapy for cGAS/STING Pathway Activation. *The FASEB Journal* 2021; **35**(S1).